Design of a Series Articulated Bipedal Robot Capable of Agile and Transient Maneuvers

Nathan Eduard Weiss

Thesis presented in partial fulfilment of the requirements for the degree of Master of Engineering (Electronic) in the Faculty of Engineering at Stellenbosch University.

Supervisor: Dr C. Fisher
Department of Electrical and Electronic Engineering

March 2023

Acknowledgements

To my academic supervisor, Dr. Callen Fisher, the success of this project could not have been achieved without your invaluable support and guidance over the past two years. It has been an honor and privilege to work with you and share your enthusiastic passion for robotics. Thank you for always motivating me during those tough times and always being available to chat when I needed advice. May the "Dream Team" live on and may our paths cross again in the future!

I would like to thank my parents and family for everything they have done for me over the past six years. Thank you for always supporting me through my educational journey and inspiring me to maintain a positive outlook on life. When times have been tough you have always motivated me to be resilient and work towards achieving my goals.

To all the friends in the ESL, thank you for providing me with an amazing work life balance through all the social events and interesting lunch time conversations; there is never a dull moment when you guys are around! To my office friends: Annika, Sam and Andries ... a.k.a "The Night Shift", thank you for all the venting sessions, coffee breaks, inspirational moments and the occasional beer! I will forever cherish the memories we have made and the friendships I have built during my time at the ESL. Together we have finally made it through this degree; despite Covid, pandemic lockdowns and the continuous challenges presented by load shedding. I'm really going to miss you guys next year.

Lastly, I would like to thank the NRF (National Research Foundation) for funding this research under grant number 129830.

UNIVERSITEIT•STELLENBOSCH•UNIVERSITY
jou kennisvennoot • your knowledge partner

Plagiaatverklaring / *Plagiarism Declaration*

By submitting this thesis electronically, I declare that the entirety of the work contained therein is my own, original work, that I am the sole author thereof (save to the extent explicitly otherwise stated), that reproduction and publication thereof by Stellenbosch University will not infringe any third party rights and that I have not previously in its entirety or in part submitted it for obtaining any qualification.

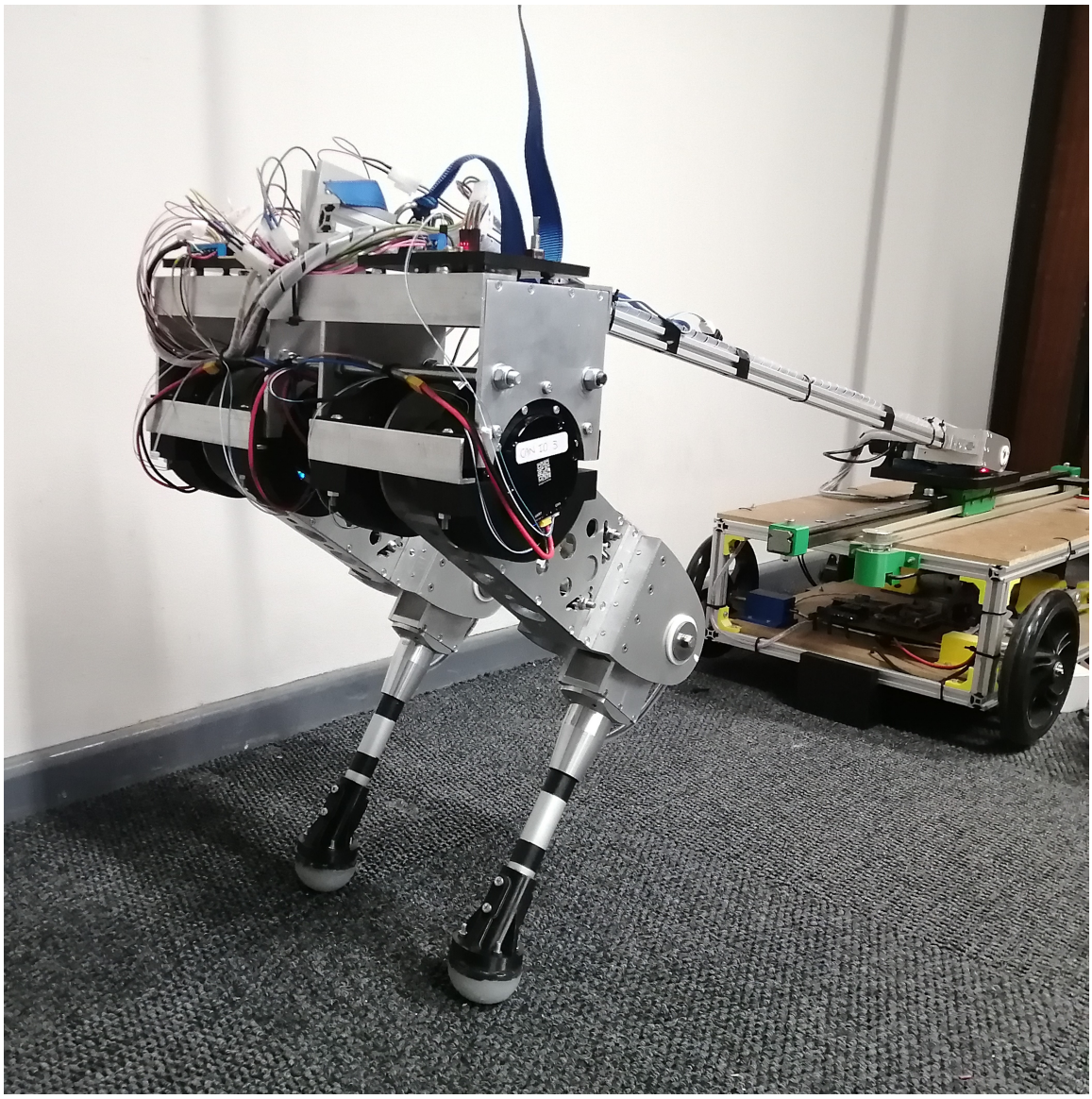

"Science can amuse and fascinate us all, but it is engineering that changes the world." - **Isaac Asimov**

Abstract

English

For legged robots to effectively emulate the dynamic maneuverability, mobility and agility presented by animals in nature, highly dynamic and robust legged locomotive systems are required. In achieving transient legged mobility, legged robots are capable of employing static and dynamically stable motions, including walking, running and jumping, to navigate various topographic terrains and overcome obstacles in unknown environments. However, due to the numerous complexities and non-linearities involved in legged locomotion; researchers in the past have struggled to produce robotic systems that embody the same level of dexterity and maneuverability seen by their biological inspiration.

The aim of this thesis was to design and develop a series articulated bipedal robot capable of performing agile and transient maneuvers. In accomplishing this objective, the designed robots would serve as a platform for future research candidates at Stellenbosch University to explore legged locomotive compliance on various terrains. However, the main focus of this research involved the investigation and implementation of key design principles, identified through literature to have contributed to the advancements seen in existing legged robots.

To aid the design process of the bipdeal robot, named Q-Bert, an analytical analysis was employed to investigate the jumping performance of a two link articulated leg model for various link lengths and actuators. This resulted in the selection of an appropriate link length, along with a Quasi-Direct Drive electric actuation transmission. Thereafter, an iterative mechanical design process was conducted to produce an initial monopedal prototype; while ensuring adequate structural integrity and minimized system mass and inertia. Furthermore, the planar motion of both, the monopod and biped platforms were constrained within the sagittal plane and supported by a developed vertical planarizing cart system.

Q-Bert's dynamic motions were embodied through the implementation of a virtual model controller inspired by Raibert's control framework. The performance of these dynamic motions were evaluated and verified through a performance metric known as vertical specific agility. This showed the agility of Q-Bert to surpass some existing dynamic robots; however, was unable to compete with the most agile legged systems. The

transient capabilities of Q-Bert were compared to long-time-horizon trajectories generated through a trajectory optimisation simulation and verified Q-Bert's suitability for transient maneuvers. Q-Bert's verified suitability was achieved through periodic hopping maneuvers that showed the steady-state hopping frequency and height of the robot to align with the simulated trajectories. Lastly, the maximum recorded jumping height attained by Q-Bert successfully surpassed the analytical jumping height determined during the design analysis and validated the robots design process.

Afrikaans

Vir beenrobotte om die dinamiese beweeglikheid, mobiliteit en ratsheid wat diere in die natuur bied effektief na te boots, word hoogs dinamiese en robuuste beenlokomotiefstelsels vereis. As verbygaande beenmobiliteit bereik kan word, is beenrobotte in staat om staties en dinamies stabiele bewegings te gebruik, insluitend loop, hardloop en spring, om verskeie topografiese terreine te navigeer en hindernisse in onbekende omgewings te oorkom. As gevolg van die talle kompleksiteite en nie-lineariteite wat egter by beenbeweging betrokke is, het navorsers in die verlede gesukkel om robotstelsels te produseer wat dieselfde vlak van behendigheid en beweeglikheid vorstel as wat deur hul biologiese inspirasie bereik word.

Die doel van hierdie tesis was om 'n reeks geartikuleerde tweevoetige robot te ontwerp en te ontwikkel wat in staat is om ratse en verbygaande bewegings uit te voer. Nadat hierdie doelwit bereik is, sal die ontwerpte robotte dien as 'n platform vir toekomstige navorsingskandidate aan die Universiteit van Stellenbosch om beenlokomotiefnakoming op verskeie terreine te ondersoek. Die hooffokus van hierdie navorsing het egter die ondersoek en implementering van sleutelontwerpbeginsels behels, wat in die literatuur geïdentifiseer is as bydraend tot die vooruitgang van bestaande beenrobotte.

Om die ontwerpproses van die tweevoetige robot, genaamd Q-Bert, aan te help, is 'n analitiese analise gebruik om die springprestasie van 'n tweeskakel-geartikuleerde beenmodel vir verskeie skakellengtes en aktuators te ondersoek. Dit het gelei tot die keuse van 'n gepaste skakellengte, saam met 'n Quasi-Direct Drive elektriese aandrywingstransmissie. Daarna is 'n iteratiewe meganiese ontwerpproses uitgevoer om 'n aanvanklike eenpotige prototipe te vervaardig; terwyl voldoende strukturele integriteit behou word sowel as stelselmassa en traagheid tot die minimum beperk word. Verder is die planêre beweging van beide, die eenpotige en tweevoetige platforms binne die sagittale vlak beperk en ondersteun deur 'n ontwikkelde vertikale planariserende karstelsel.

Q-Bert se dinamiese bewegings is voorgestel deur die implementering van 'n virtuele modelbeheerder wat deur Raibert se beheerraamwerk geïnspireer is. Die prestasie van hierdie dinamiese bewegings is geëvalueer en geverifieer deur middel van 'n prestasiemaatstaf

bekend as vertikale spesifieke behendigheid. Dit het getoon dat die behendigheid van Q-Bert sommige bestaande dinamiese robotte oortref, maar is egter nie in staat om met die mees ratse beenstelsels te kompeteer nie. Die verbygaande vermoëns van Q-Bert is vergelyk met langtermyn-horisontrajekte wat deur 'n trajek-optimeringssimulasie gegenereer is en Q-Bert se geskiktheid vir verbygaande bewegings is geverifieer. Q-Bert se geverifieerde geskiktheid is bereik deur periodieke hop-bewegings wat getoon het dat die bestendige-toestand hop-frekwensie en hoogte van die robot in lyn is met die gesimuleerde trajekte. Laastens het die maksimum aangetekende springhoogte wat deur Q-Bert bereik is, die analitiese springhoogte wat tydens die ontwerpontleding bepaal is, suksesvol oortref en die robotontwerpproses bekragtig.

Contents

List of Figures

List of Tables

Nomenclature

ESL	Electronic Systems Laboratory
CoM	Centre of Mass
MoI	Moment of Inertia
DoF	Degree(s) of Freedom
GRF	Ground Reaction Force
BLDC	Brushless Direct Current
GM	Geared Motor
DD	Direct Drive
QDD	Quasi-Direct Drive
SEA	Series Elastic Actuator
FOC	Field Orientated Control
CAN	Controller Area Network
FEA	Finite Element Analysis
FoS	Factor of Safety
FSM	Finite State Machine
SLIP	Spring-Loaded Inverted Pendulum
MCU	Micro Controller Unit
IO	Input/Output
OVP	Over Voltage Protection
PPR	Pulse Per Revolution

Chapter 1

Introduction

Over the course of the past few decades, legged locomotion has emerged as a growing field of research with idealised advantages over conventional wheeled locomotion in navigating rugged and discontinuous topographic terrain. The ideology of legged locomotion in robotics has predominantly been inspired through animals in nature, which effortlessly perform highly dynamic and transient motions to ensure their survival [1, 2]. While large portions of Earth have remained unscathed by humans due to the inaccessibility of wheeled platforms; animals have roamed freely by embodying rapid maneuverability, mobility and agility characteristics [3].

Research advancements in the design and control of highly dynamic legged robots has been paramount in generating robust steady-state locomotion to emulate the dynamic maneuverability and dexterity presented by animals as shown in Figure 1.1 [4, 5]. In recent times, the primary objective in legged robotics has been shifted towards transient motion to employ legged robots in real world applications including remote location exploration; and search and rescue operations. However, achieving rapid-transient maneuverability, such as accelerating, decelerating and turning maneuvers, has often been presented as a challenging task due to the complex and non-linear system dynamics embodied by legged locomotion.

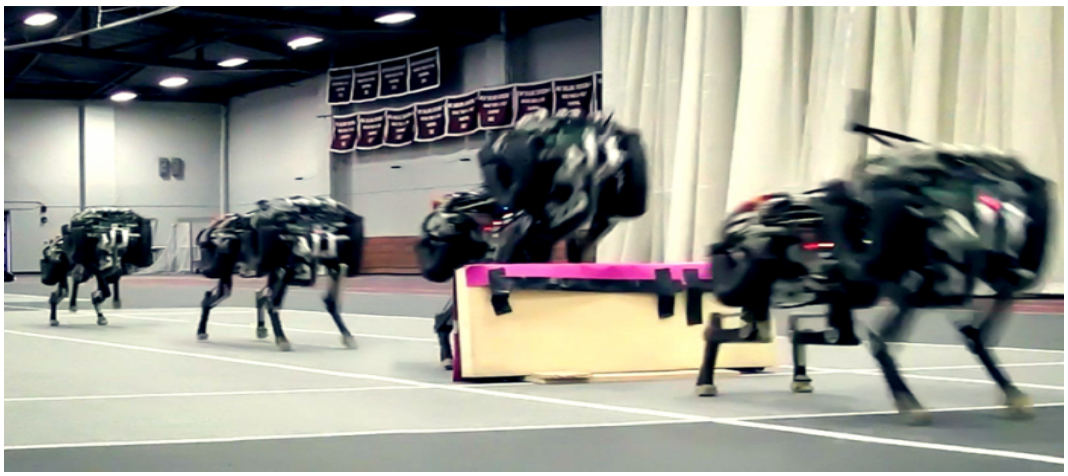

Figure 1.1: An overlaid image of the bio-inspired MIT Cheetah 2 quadruped robot demonstrating steady-state locomotion on an experimental circuit before autonomously jumping over a 40 cm high obstacle [6].

1.1. Motivation and Background

Despite the advancements seen in the legged robotics community over the past few decades; the first potentially feasible robots for commercialization only started to emerge in 2019, through the production of the world renowned quadruped robot developed by Boston Dynamics, named Spot [7]. Although numerous legged robots exist and present promising dynamic capabilities; these platforms are limited by significant locomotive trade-offs in terms of mobility and dexterity, while navigating unfamiliar terrain compared to biological mechanisms [3]. Notably, bio-inspiration in legged robotics has enhanced the locomotive characteristics of mobile robots by allowing them to travel over challenging terrain in environments which pose danger to humans. However, the existing robots struggle to comprehend uncertainties in challenging terrain; whereas animals are able to completely adapt to their environment through transient motions such as rapid acceleration and deceleration.

This discrepancy between robotic and animal locomotion on rugged terrain has led researchers and biologists to believe that transient motions have not been fully understood within the robotics community [8]. Although biological and robotics mechanisms are fundamentally different, muscle tendons and connective tissue are seen to be pivotal aspects in generating compliant animal locomotion [9]. Therefore, for legged systems to achieve compliant, transient locomotion across multiple topographic terrains, robots are required to employ static and dynamic, highly stable and agile maneuvers. In recent times, trajectory optimisation techniques have been used to explore and gain a better understanding of these compliant, transient maneuvers with remarkable solutions obtained in improving the robustness of legged locomotion [4, 10–12].

Therefore, the purpose of designing a series articulated bipedal robot tailored for transient and agile maneuvers is to provide a low cost platform for future students within the Electronic Systems Laboratory (ESL) [13] to explore robust locomotion on rough terrain. Additionally, the infrastructure developed in this research would enable students to execute trajectory optimisation inspired control templates and explore feasibility of various controllers.

1.2. Aim and Objectives of the Project

The research conducted in this thesis is specifically aimed at developing a series articulated bipedal robot capable of performing transient and agile maneuvers and has been divided into several objectives in order to achieve this main research aim. The developed bipedal robot is named Q-Bert, however its name is only used towards the backend of this thesis. The identified objectives cover several aspects of the project which include the

mechanical design, actuation strategy, artificial support system, controller implementation and performance evaluation of the system. The outlined objectives to achieve the desired outcome of this thesis are as follows:

1. Develop an analytical simulation study to aid the design process of the bipedal robot by assessing the jumping performance produced by a range of different link lengths for the limbs. The analytical simulation should also serve as an environment to evaluate and compare various actuators. This is explored in Chapter 4.

2. Construct the mechanical design of the bipedal robot through the use of a finite element analysis (FEA) to ensure a system capable of withstanding detrimental ground impact forces. During this objective, multiple prototype designs are produced and evaluated in an iterative manner to optimize the design for dynamic maneuverability, followed by the manufacturing and assembly of the final design prototype. This is explored in Chapter 5.

3. Design and manufacture an artificial restraint system using inspiration from current existing systems to support and constrain the robot in the sagittal plane. This includes the incorporation of sensors to monitor the robots position and motion. This is explored in Chapter 5.

4. Develop and implement a simple control template to execute transient and agile motions on the bipedal robot. The stability of the controller should be analysed and evaluated during high ground reaction forces to ensure a robust system. This is explored in Chapter 6.

5. Conduct a trajectory optimisation simulation of a simplified model to verify the dynamic, transient maneuvers of the robot; which include acceleration, steady-state and deceleration locomotive states. This provides a means to compare and justify the performance of the physical robot. This is explored in Chapter 3 and 7.

1.3. Scope and Limitations

The scope of this project was limited and constrained by numerous factors that required consideration during the design process to ensure the completion of this thesis within the stipulated timeline. Firstly, the primary constraint on the research conducted in this thesis involved time, as a limited period of 24 months was outlined for this project. Secondly, large portions of the robot's design process were limited within the manufacturing capabilities of the Stellenbosch University electronic department workshop to reduce expected lead times and expenditure.

Lastly, to investigate and verify the dynamic, transient and agile capabilities of the robot, the system was restricted to a known flat surfaced environment; while the executed robotic motions were limited to periodic hopping maneuvers. Furthermore, the complexity of the robot's design scope was limited to an active 4 degree of freedom (DoF) mechanism and constrained the systems motion within the sagittal plane, due to the additional support required by bipedal robots. Expanding the robots complexity to enable enhancements in three dimensional maneuverability and system range of motion through additional DoF's was considered to be outside the scope of the thesis.

1.4. Plan of Development

This thesis begins with a thorough literature review section, provided in Chapter 2, which discusses the evolution of legged robotics and details several existing highly dynamic legged robots. This chapter describes the desired principles and trade-offs encountered during compliant leg design. Additional focus is placed on the numerous actuation and transmissions strategies, along with artificial restraint systems utilized throughout the legged robotics community. This is followed by a discussion on control templates and the use of trajectory optimisation in legged robotics.

The methodology of this thesis is outlined in Chapter 3 and provides the overall project requirements in terms of system and transmission objectives. Here, a brief description of the method of approach for each major aspect of this thesis is provided. However, special focus is placed on the implementation of the trajectory optimisation simulation required to validate the transient maneuverability of the robot.

This is followed by the robot design analysis detailed in Chapter 4, which focuses on generating an analytical analysis to aid actuation and link length selection based on the jumping performance of different actuator combinations. Evidently, this chapter provides the foundation of the design process and is proceed by the mechanical design of the robot, detailed in Chapter 5. Here, focus is placed on the structural design to ensure the system is robust and resistant to failure. This chapter also details the development of an artificial restraint system used to support and constrain the robot within the sagittal plane.

The controller design and implementation is described in Chapter 6, which details the framework of a virtual model controller inspired by Raibert's hopping control algorithm. Each of the individual aspects involved in the controller are described along with an initial torque mapping simulation.

The robot's physical experiments and validation are detailed and discussed in Chapter

7, which presents the results of the monopod and bipedal robots for an array of conducted tests and discusses the comparison to the trajectory optimisation simulation results. Lastly, a brief conclusion and future work section is presented in Chapter 8. The outlined structure of this thesis is summarized in Figure 1.2.

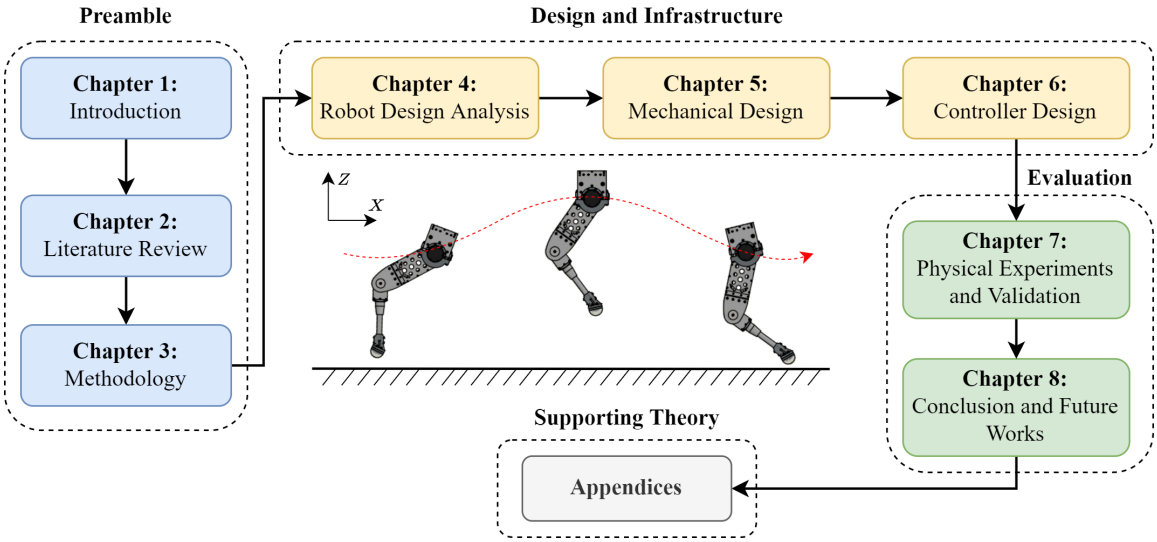

Figure 1.2: This image shows the outlined structure of this thesis. It begins with a preamble component compromising of a brief introduction, followed by a literature review and methodology chapter. This is proceeded by a design and infrastructure component, detailing the robots design analysis in Chapter 4, followed by the mechanical design in Chapter 5 and controller design in Chapter 6. Lastly, the physical experiments and validation was presented in Chapter 7, followed by the conclusion in Chapter 8.

Chapter 2

Literature Review

This chapter serves to provide an adequate foundation for the work produced in this thesis by investigating the intricacies involved in legged robotic motion, design and actuation. In the process, gaining insight into the transient and agile motions seen in legged robots by analysing current literature. For years, legged robots have attempted to replicate the dynamic characteristics and maneuverability observed in animal locomotion through their ability to effortlessly overcome obstacles and terrain discontinuities.

However, unlike biological mechanisms in nature, robotic mechanisms exhibit several complexities in their kinematics, dynamics and control due to modelling irregularities and limitations in mechanical compliance. Therefore, robotic actuators and mechanisms are required to overcome these complexities in replicating the dynamic movements produced by muscles and ligaments in animals. As this chapter progresses, legged robotic terminology will become comprehensible as the desirable properties surrounding the design and development of legged robots are addressed.

2.1. Evolution of Legged Robots

Legged locomotive systems can be described as a system that navigates through the use of discrete footholds and comprises of several mechanical links, connected by prismatic or rotational joints to form a leg structure [1, 14]. In comparison to their wheeled counterparts, legged mechanisms have been regarded as superior due to their ability to climb over obstacles and overcome terrain discontinuities [1]. Since the inception of legged robots, literature related to walking robots has been inspired by biological systems found in nature through resemblance in morphology and locomotion [15, 16]. Whilst animals in nature are seen to embody dynamic attributes, such as remarkable mobility and agility in navigating irregular terrain and rapid maneuverability in overcoming predatory encounters as shown below in Figure 2.1 [1]. Through the development of numerous bio-inspired design templates, legged robotic systems have attempted to replicate these dynamic features embodied by animals in order to emulate locomotive versatility and dexterity in robots.

(a) The rapid maneuverability and agility seen by animals in nature during predatory encounters. Image from [19].

(b) The MIT Mini Cheetah quadruped robot displaying its dynamic and agile capabilities during a perfect back-flip maneuver. Image from [20].

Figure 2.1: An illustration of the morphological and dynamic characteristics emulated in robotic locomotion through biological inspiration.

Throughout the evolution of legged robotics, monopedal robots have often been introduced as testbeds for implementing proof of concept control strategies and justifying mechanical designs [16]. Despite the lack of balance suffered by monopedal robots due to their single contact point used to aid support, balance and translation; these platforms are capable of revealing systematic complexities within the kinematics and dynamics of the robot [1, 16]. These complex phenomena observed within robots include underactuation, non-linear or hybrid dynamics and the possibility of sliding foot contact [4]; evidently contributing to the increased difficulty in analysing and controlling legged robots. Unlike robots, monopedal biological systems do not exist in nature. However, nature exhibits emulated monopedal characteristics through the locomotive techniques of bipedal animals, such as the kangaroo (*Macropus*) and South African springhare (*Padetes capensis*); which hop using both feet [17]. Additionally, biologists' have shown through studies that the kangaroo utilizes its tail for support and balance, while it behaves as an additional leg in propelling itself forward, creating a momentary pentapedal gait [18].

Similarly, nature offers legged robots a wide range of bipedal and quadrupedal inspiration through the anatomy of animals such as the ostrich (*Struthio camelus*) and cheetah (*Acinonyx jubatus*). Notably, the fastest land bound bird and mammal, possessing the ability to run at speeds of approximately 16.67 m/s and 29 m/s, respectively [21, 22]. Although animals are naturally capable of achieving such speeds, research has shown robots to struggle with speed; recording the average bipedal speed under optimal power consumption to be 1.551 m/s [23]. Whereas, the Guinness World Record for the fastest bipedal robot to complete a 100 m sprint was established by the robot Cassie, running at a speed of 4.043 m/s without the use of cameras or external sensors [24].

The differences in speed observed between animals and legged robots are influenced by numerous factors such as topology, actuator limitations and inefficiencies introduced by collision losses and joint friction [25]. Despite these struggles, the functional principles regarding the locomotion of these animals has enhanced the perception of bipedal and quadrupedal robotic motion. As the provision of an additional leg, converting a monopod to biped, enables inertial counter-balancing and dynamic stability while hopping, walking or running; alleviating the dependency on foot placement experienced by monopedal robots in solving the control problem [16]. Similarly to monopedal robots, bipedal robots typically encounter static instability at rest and require additional support, due to the implementation of point foot contact models used to reduce actuation complexity [4,16,17]. Subsequently, quadrupedal robots are capable of maintaining stability during static and dynamic maneuvers as a result of the support polygon generated by the contact points of the legs.

2.1.1. Existing Platforms

The first documentation on legged systems dates back to the mid 1950's with a number of researchers studying the development of systematic walking machines. The production of the first legged robot later occurred in the late 1960's in the form of a human operated quadruped robot capable of adopting different locomotive gaits [1, 26]. However, the developed platform was considerably large, heavy and power intensive; as the robot required an internal combustion engine to propel the hydraulic actuation system. In addition, the vehicles dependency on well equipped human operators evidently expedited the need for automated control systems.

In 1983, a 3-D monopedal hopping robot developed by Marc Raibert became the first truly dynamic legged platform [27]. Raibert's robot was capable of achieving active balance through a single contact point with the ground, despite applied external disturbances and without the aid of additional support. The hopping robot exhibited high speed steady-state locomotion by translating in a preferred direction through the implementation of a simple control algorithm. Furthermore, the robot embraced a simplistic design consisted of a pneumatic actuated prismatic leg in combination with a mechanical spring and a hydraulic actuated hip. Considering the problems identified in the first legged vehicles, the modern day legged platforms presented in Figure 2.2 can be considered as milestones throughout the evolution of legged robots.

Inspired by the anatomy of a flamingo, researchers at the MIT Leg Lab developed a series articulated bipedal planar walking robot, named Spring Flamingo, for the purpose of implementing various force based control techniques, specifically virtual model control [28].

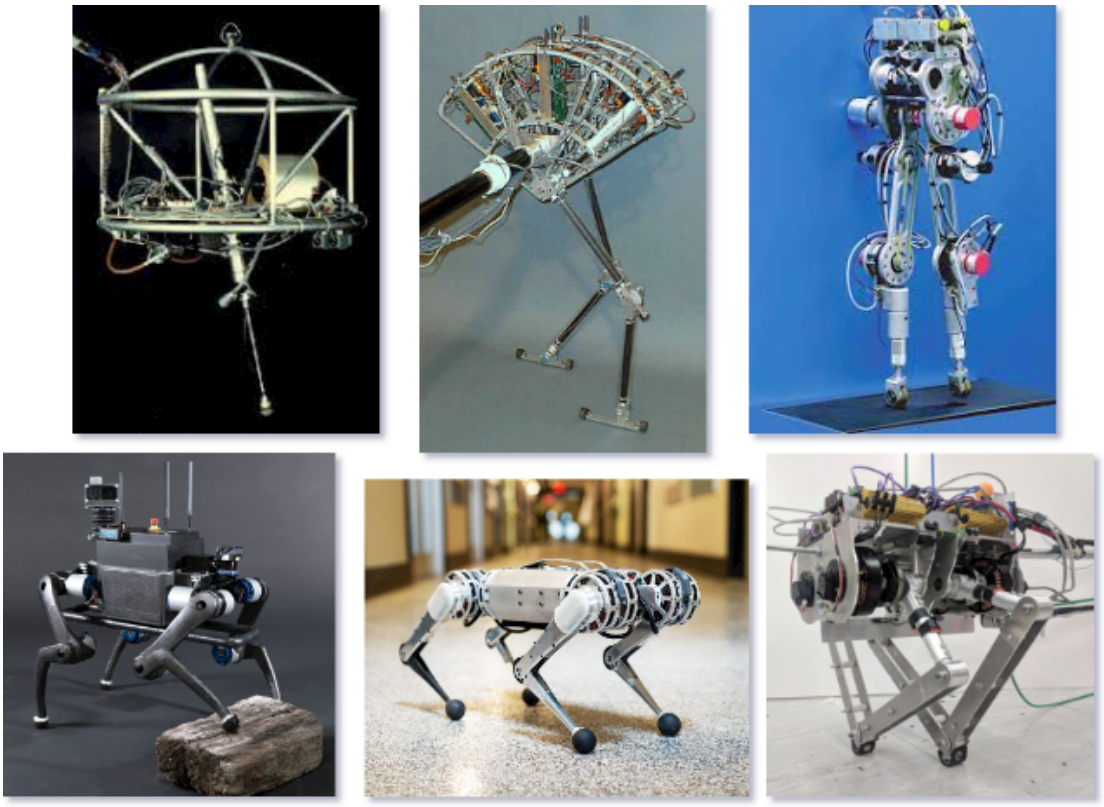

Figure 2.2: The progression of legged robotic platforms over the past 40 years illustrating various morphologies, topology and actuation types. The platforms from top left to bottom right: Raibert's 3D Hopper [29], Spring Flamingo [28], RABBIT [30], ANYmal [31], MIT Mini Cheetah [32] and Baleka [8].

Spring Flamingo displayed significant robustness through successfully performing over 200 experiments at a maximum walking speed of 1.2 m/s before experiencing a breakdown [28]. All actuators were situated at the upper body of the robot and made use of cable drive transmission to actuate the joints of the legs. The topology of the articulated robot included an ankle joint used to increase the stability of the platform. In addition, the robot employed series elastic actuation (SEA) through linear compression springs to increase energy efficiency and mitigate shock impulses at the cost of limiting control bandwidth.

In 2003, researchers developed a simplistic passive walking bipedal robot, named RABBIT, as a testbed for advanced control techniques to represent human walking [30]. The developed platform consisted of a simplistic mechanical structure, utilizing an articulated linkage mechanism for the legs and underactuated point feet. The joints of the legs were actuated using high power to weight ratio, DC motors fitted with gear reducers and transmitted power to the knee joint via a belt drive transmission. RABBIT yielded exceptional closed-loop control robustness as the robot was capable of continuously walking for 70 steps, at a speed of 0.7 m/s before manual terminating the controller [30].

In the past, research involving highly advanced and dynamic legged systems has been limited within well funded laboratories; which emulate perfect environmental conditions and fail to emphasize the use of legged robots in real world applications [12]. However, in recent years, companies such as the renowned Boston Dynamics and Agility Robotics have emerged; producing commercial legged robots for real world applications as well as specialized research and development. This includes the ETH Zurich ANYmal quadruped, specifically developed for real world applications such as long endurance autonomous missions in harsh environments [31]. Alternatively, the ANYmal robot could be used for remote location prospecting or equipment monitoring in hostile and dangerous environments [1]. Due to major focus placed on outdoor sustainability, bio-inspiration was embraced in the joint arrangement with the implementation of successive hip abduction/adduction; resulting in the platforms resemblance of a dog. Offset leg links allowed the robot joints to obtain a full range of motion enabling high mobility to climb over challenging obstacles. Additionally, the robots performance displayed impact robustness and high disturbance rejection capabilities.

Inspired by the dynamic maneuverability and locomotion embodied by cheetahs, researchers at MIT developed a highly dynamic, bio-inspired miniature quadruped robot to resemble the dynamic characteristics seen in cheetahs [32]. The scaled robot, named the MIT Mini Cheetah, implemented a custom designed low cost, low impedance proprioceptive actuators and enabled robustness against external impacts, while achieving high torque control bandwidth. Similarly to the MIT Cheatah series and the robots predecessor, the MIT Cheetah 3 [33]; the actuator technology allowed force transparency [34, 35] through torque feedback enabling the robot to detect surface contact. Evidently, these features contributed to the robot's highly dynamic and nimble capabilities seen in walking, running and performing maneuvers such as perfect 360° back-flips.

The investigation into legged robotic milestones was concluded with the bidepal robot Baleka [8]. In 2019, the platform was developed for rapid acceleration and braking maneuvers and made use of underactuated 5-link mechanism legs along with proprioceptive force feedback to identify ground contacts. The robot remained constrained in the sagittal plane and validated its agile and dynamic functionality through various vertical hopping maneuvers. Unlike the various series articulated robots reviewed in this section, Baleka is an example that rapid maneuverability and agility can be achieved through topologies unrepresented by biological mechanisms. As the platform successfully displayed robustness to ground impacts during remarkable vertical agility experiments, which resulted in the robot jumping approximately 3.6 times its initial resting height [8].

2.2. Compliant Leg Design Principles

As seen in existing legged platforms, dynamic mobility and agility can be achieved through numerous leg morphologies, topologies and actuation strategies. Compliant robot design comprises of several balanced trade-offs within these categories, while prioritisation of the most prominent dynamic features is required for transient motion. Legged robot design templates have identified these balanced trade-offs as follows [3, 8]:

- Torque density versus mechanical impedance.
- Compliance and energy efficiency versus controllability.
- Structural strength and robustness versus speed.

This section aims to extract compliant design principles through the investigation of these balanced features to achieve the agile and dynamic motion requirements of this thesis.

2.2.1. Principles for High Powered Legs

1. **Speed:** As a prerequisite in achieving highly dynamic legged locomotion, robots require actuators capable of producing a high speed output. This is required to satisfy the alternating back and forth motion created by the leg in transitioning between periods of high speed swing and stance to accelerate the robot forward. This occurs as the joints of the leg are rapidly re-orientated during flight to achieve a desired foot position for landing, returning the robot to the stance phase as ground contact is resumed.

   Typically, research has established a directly proportional relationship between the running speed and stride frequency of robots, resulting in a lower duty factor within platforms [8, 26, 35, 36]. However, this creates a trade-off amongst critical design features as increased speeds result in increased ground reaction forces. This is due to larger forces applied on the robot to accelerate it forward at higher speeds, which compromises the structural integrity of the robot through induced stress concentrations [26]. Therefore, a delicate balance is required between the speed and force output of robotic actuators. Subsequently, this ensures an equilibrium in the systems net energy input, as shorter contact periods are experienced during higher speeds and result in increased ground reaction forces.

2. **Torque Density:** Legged systems present a conflicting actuation challenge with the demanding force and speed requirements for dynamic maneuverability. Typically in

the case of legged robotic actuation, torque density is defined as mass specific torque and is considered to be a critical and limiting performance characteristic [3]. Legged systems should strive to maximize torque density, as insufficient torque will result in the failure of the robot to support its own weight. In addition, maximized torque density provides a high torque to inertia ratio, ensuring the actuators torque is used to accelerate the robot rather than dissipated through actuating the mechanism [32].

Furthermore, legged robots typically experience ground reaction forces ranging between two to three times the weight of the robot [3]. Similarly, dogs and humans experience normal ground reaction forces of 2.6 times and 3 times their body weight, respectively [35]. Therefore, legged robots require high torque density actuators to maximize the foot force during these periods of surface contact.

3. **Mechanical Impedance:** The acceleration of legged robots is dependant on the applied force and mass of the system. To maximize the accelerating capabilities of a legged system, the design principles used should aim to maximize torque density and minimize mechanical impedance. Minimizing the mechanical impedance requires decreasing the mass, inertia and friction of the system, including the reflected inertia, stiffness and damping experienced by the actuators. This can be achieved by implementing mechanical mechanisms which locate higher percentages of mass at the hip region of the robot; commonly through the use of a co-axial motor placement [3,8].

   In addition, mechanical impedance can be minimized by proportionately scaling the mechanical structure with respect to the size of the actuator, while reducing the mass of the mechanical limb without neglecting the structural integrity. Alternatively, passive mechanical elements used to aid mechanism compliance can be viewed as contributing factor to the overall impedance of the system and should be carefully assessed during legged robotic design.

2.2.2. Active or Passive Mechanism Compliance

Mechanism compliance inspired by the compliant motion seen in animals has been a profoundly debated topic in the legged robotics community. As both active and passive methods of compliance demonstrate advantages in controlling the force and position of robotic legs. Active mechanism compliance utilizes sensory information to aid actuation decisions through control software to virtually emulate mechanically compliant behaviors [37]. This form of compliance is executed purely in software without the aid of additional mechanical elements to generate compliant motion. As result of the joint flexibility provided by active force sensing, this form of compli-

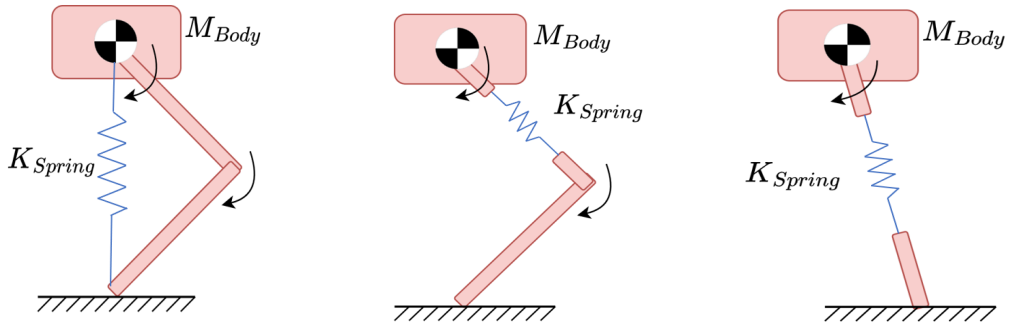

(a) Active Compliance **(b)** Passive Compliance **(c)** Simplified SLIP Model

Figure 2.3: A visual comparison between active and passive mechanism compliance in robots along with a standard SLIP model.

ant control enables robotic actuation to satisfy force and position control requirements [38].

Typically, active mechanism compliance is implemented in the form of a generalized spring and damper model, acquiring impedance control to interact with the robot's environment during execution. This is similar to a virtual representation of the Spring-Loaded Inverted Pendulum (SLIP) template used to describe walking and running in robots as shown in Figure 2.3 [39]. However, high control bandwidth is required near the kilohertz time scale for active compliance to operate effectively [3, 8].

Passive compliance is a physical mechanism which utilizes passive dynamics through underactuated motions to provide mechanical stiffness and adaptability, while contributing additional energy to the system. Passive mechanism compliance aims to replicate the flexibility and durability observed in the bone structure and muscle tendons of animals and humans to perform dynamically compliant motions; while protecting the robot against external forces [38]. This form of mechanism compliance is typically implemented through elastic actuation strategies such as SEA's; which involve coupling mechanical springs (torsional, compression or leaf) in combination with robotic actuators to aid motion, but at the cost of control bandwidth, backdrivability and stability [40].

Alternatively, mechanical compliance has been achieved through exploiting passive dynamics and actuation in the design of robotic feet as displayed in robots such as ATRIAS [41] and Spring Flamingo [28]. The additional energy contributed by these mechanical components to the joints and links of robots has proven useful in attenuating the transient effects of external disturbances [37, 42]. However, unlike biological structures, passively compliant robots lack the desired flexibility due to the inability to dynamically adjust the stiffness and material properties of mechanical components. In addition, the increased complexity in designing passively compliant mechanisms often results in mechanisms prone to mechanical failure, requiring joint overload protection [42].

2.2.3. Robotic Robustness

Structural robustness is a key design principle in producing legged mechanisms capable of withstanding the detrimental impact loads experienced due to ground reaction forces as mentioned in Section 2.2.1. Therefore, mitigating the effects of these cyclic forces should be prioritized without compromising the legged mechanism to fatigue failure. However, a trade-off exists between the structural integrity and agility of the robot, particularly in the distal part of leg due to increased rotational inertia imposed by the hip and the dissipated kinetic energy upon landing [26]. Balancing this trade-off can be achieved by minimizing the distal leg impedance of the system, specifically the mass, through the use of high strength-to-weight composite materials such as carbon fiber or metals such as aluminium alloys and titanium. Further efforts to increase robustness can be implemented through the use of backdrivable actuators containing low gear ratios to decrease the reflected inertia experienced by the actuator [8]. This allows the actuator to absorb the shock impacts generated by ground reaction forces during landing, reducing the detrimental effect of these forces on the system.

In addition to structural features, robotic robustness includes the systems behaviour and ability to respond to factors of uncertainty without making the system unstable. Robotic literature underlines the importance of robustness in a broader control context as the systematic response to variations in contact timing and joint orientation, irregularities in system dynamics, sensor noise and communication delays [10]. As a preliminary approach in exploring the robustness of robotic locomotion; researchers have developed trajectory optimisation frameworks derived from first principles to inspire compliant motion and validate system robustness [4, 10]. These optimisation techniques investigate and simulate the complex problem of legged locomotion and provide a method to define system robustness through torque and contact stability limitations.

2.2.4. Force Proprioception

Force proprioception is the perception of internal forces observed on a robot through the awareness of joint orientation, velocity and torque to enable force transparency. In recent times, proprioception has become a common approach in determining foot contact forces experienced by robots through the use of motor current sensing to provide controllers with torque feedback as seen in agile platforms such as the MIT Cheetah, MIT Mini Cheetah, GOAT and Baleka [3, 8, 32, 35]. However, this torque-based method is susceptible to minor deviations in accuracy due to mechanical impedance experienced within legged mechanisms as the foot force propagates through the structure to the motors [3]. Therefore, it is important to validate the accuracy of proprioception in robotic platforms before solely relying on this method of force sensing. Force proprioception enables robots to embody

the following behaviours [43]:

- **Feel:** Sense objects and interact with the surrounding environment.
- **Process:** Process signals based on force transparency to generate commands.
- **Respond:** React to generated commands at the desired actuation bandwidth.

To determine the external contact forces observed at the foot of the robot, the current induced in the motor windings (I_m) is multiplied with the motor's torque constant (K_t) to calculate the produced torque feedback (τ_m). Thereafter, the relationship established between the inverse Jacobian transpose matrix and the motor torque allows the force vector acting at the robot's end-effector to be determined as follows:

$$\begin{aligned} \tau_m &= K_t I_m, \\ \boldsymbol{F} &= (\boldsymbol{J}_{foot}^T)^{-1} \boldsymbol{\tau_m}. \end{aligned} \tag{2.1}$$

Where the Jacobian matrix ($\boldsymbol{J}_{foot}$) represents the partial derivative of the forward kinematics of the robot's foot with respect to the generalized coordinates of the system. Furthermore, the simplicity involved in proprioception along with the elimination of additional sensors (which tend to be fragile and expensive) has promoted its use in direct drive and quasi-direct drive systems, due to the reduced reflected inertia experienced in these actuation strategies [44].

2.3. Electric Actuation and Transmission

In legged locomotion, robotic actuators are seen as the most critical components, as they attempt to replicate and embody the dynamic characteristics produced by biological features such as muscles, tendons and connective tissue. Although, literature has shown that researchers have struggled to match the degree of performance exhibited by biological mechanisms in nature, while using mechanical actuation mechanisms [12, 45]. Robotic actuation and transmission strategies have been responsible for determining the system's dynamic capabilities based on the specifications and limitations of the actuator.

However, with advancements in legged robotic actuation over the years, numerous transmission types have emerged with various trade-offs amongst each other. The advantages and disadvantages of the electric actuator transmission types shown in Figure 2.4 are discussed in this section to provide the insight required to select the best actuation strategy for the bipedal robot. The motor selection and evaluation process of the robot is further outlined in Section 4.3.1.

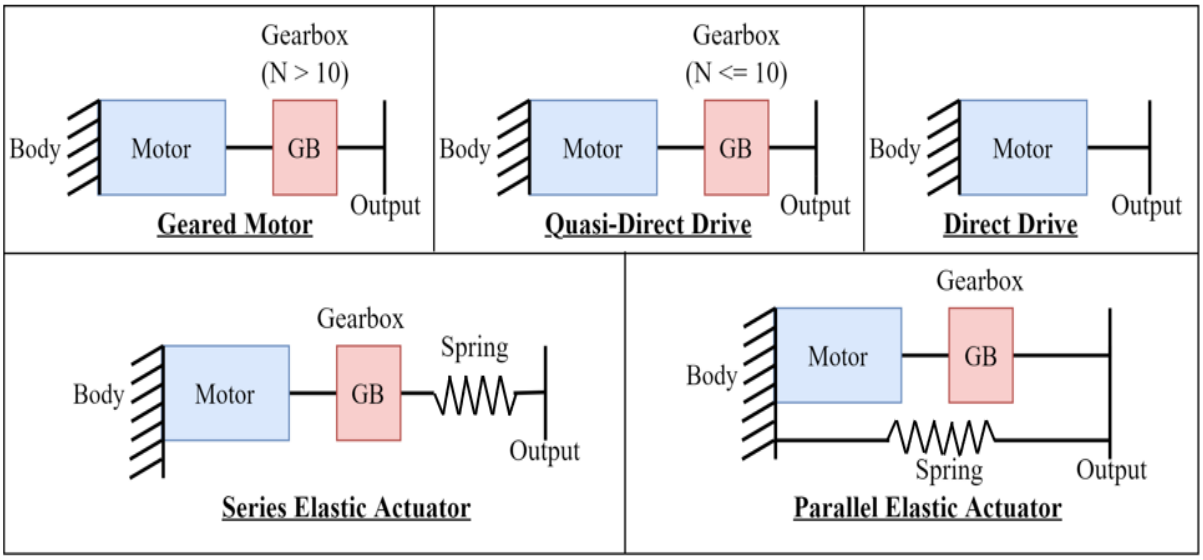

Figure 2.4: A comparison of the different electric actuator transmission types implemented throughout legged robotic platforms. Where N represents the reduction ratio of the gearbox (GB).

2.3.1. Direct Drive

The direct drive (DD) actuation strategy is the most simplistic from of transmission as the motor output is directly connected to the leg mechanism. This enables the actuator to achieve a high degree of proprioception and control bandwidth due to the absence of impeding characteristics associated with gear trains such as friction, stiction and backlash. DD actuation is typically implemented using brushless DC motors and offers high backdrivability due to the omission of gear reducers, which mitigate the effect of backlash. Therefore, the transparency exhibited by DD actuators in combination with high mechanical stiffness can be used to accurately observe external impact forces applied at the foot of the robot, increasing the robustness of the actuation transmission [12]. In addition, the absence of gear trains reduces to mass of the actuator and is seen as a key objective throughout legged robotic design principles.

However, the major downfall to DD actuation is that these actuators fail to fulfill the required torque output for high speed maneuvers. This is caused by the low torque density of the motors as speed is prioritized over force output for direct drive transmissions. Therefore, platforms which utilize this form of transmission are limited in size and need to be scaled according to the torque capabilities of the motors in order to reduce the mass of the system as seen in the quadruped robot named Minitaur [44, 46].

2.3.2. Geared Motors

Geared motors (GM) have been used in legged robotics to achieve the desired high force output and optimal torque density characteristics; typically through the use of servo-, brushed DC-, or brushless DC motors coupled with larger gear reductions as seen in platforms such as KURMET [47] and RABBIT [30]. As high transmission ratios allow the torque density output to be drastically increased in comparison to the motors standard output. However, the prioritization of force and torque density in this actuation strategy comes at the cost of low speeds, which are undesirable for rapid and transient locomotion.

The high impact forces propagated through the foot of the robot during landing maneuvers have a detrimental effect on the robustness of these actuators [48]. Geared motors are not backdrivable due to the high reflected inertia experienced in large gear transmissions [49]. Therefore, the external forces encountered during impact are directly transferred into the gearbox, creating high stress concentrations on the teeth of the gears. This results in worn out or damaged teeth and may contribute to increased backlash at the joints of the robot. Additionally, large gearing mechanisms present major sources of mechanical deflection due to non-linear factors such as friction, stiction and backlash [35]. While poor stiffness in gear transmissions can induce undesirable vibrations throughout the mechanism and decreases the control bandwidth of the motor [50].

2.3.3. Quasi-Direct Drive

Quasi-direct drive (QDD) actuators are an intermediate transmission strategy between GM and direct-drive actuators that implement a low reduction, single stage planetary gearbox with a gear ratio of less than 10 [51]. In the development of modern robotic platforms such as the MIT Mini Cheetah [32] and Baleka [8], QDD actuators have commonly been implemented using brushless DC motors and can be purchased as off-the-shelf modules containing pre-fitted gear reducers. The low reflected impedance experienced within the planetary reduction of these actuators enables proprioceptive characteristics such as high backdrivability and force transparency, through accurate current sensing at high control bandwidth [51].

In addition, QDD actuation achieves a good balance between the force, torque and speed requirements desired for rapid and transient maneuverability in legged robots. As QDD actuators are capable of delivering high output torques while operating at high speeds. Furthermore, the high backdrivability seen in QDD actuators increases their robustness as the detrimental effect of external impact forces on the transmission are reduced during dynamic motions.

2.3.4. Elastic Actuation

Elastic actuation is categorized into two types of actuators, namely series elastic actuators (SEA) and parallel elastic actuators (PEA), which consist of implementing a mechanical spring in combination with an electric motor and gearbox. The major difference between these transmission types is the location of the elastic mechanical element as shown by platforms in Figure 2.5. In addition, PEA's have the ability to decrease the force requirements of the motor through injecting stored energy into the system during motion, increasing the total torque output of the actuator [52]. In SEA's, the mechanical element is coupled between the gearbox output and mechanism load, allowing the elastic spring to isolate the motor by absorbing impulsive shock loads generated by ground contact during landing maneuvers [44]. Series elastic transmissions are commonly implemented using linear compression springs within the linkage mechanism of the leg or through cable driven torsional springs at the knee joint of the leg, as seen in platforms such as StarlETH, Spring Flamingo and KURMET [28, 47, 53].

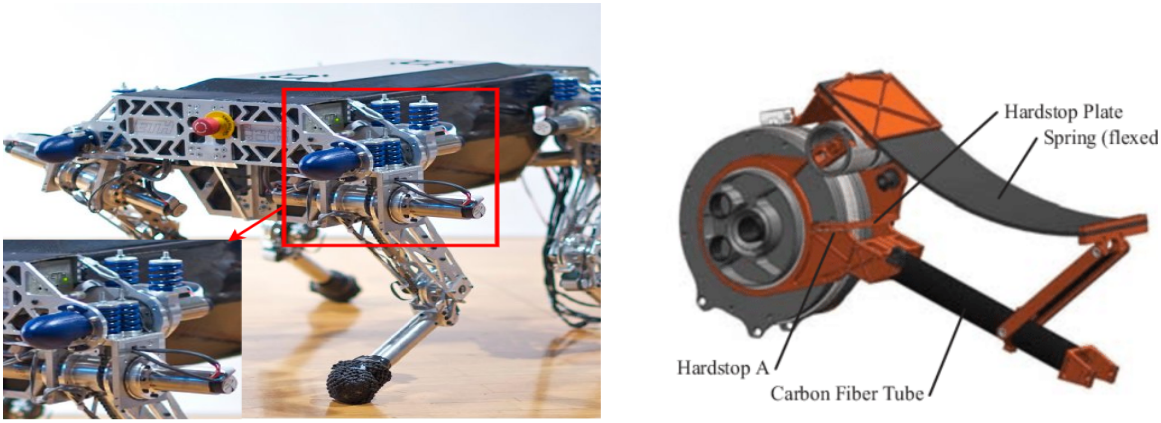

(a) SEA using linear compression springs. **(b)** PEA using a parallel leaf spring.

Figure 2.5: An illustration of elastic actuators implemented in existing platforms. (a) Linear compression springs connected to the motors and located above the hip of the StarlETH robot to assist with hip flexion. (b) A parallel leaf spring situated parallel to the motor and upper leg link of the ATRIAS robot. Images from [53, 54].

In PEA's, the mechanical spring is connected in parallel to the motor and mechanical limb output of the system. These actuators are typically implemented using leaf springs located in parallel to the upper limb of the leg or through the use of linear compression springs that encircle the knee joint and connect to the upper leg linkage as seen in platforms such as ATRIAS and SPEAR [54, 55]. Both types of elastic actuation minimize the reflected inertia of the motor by decoupling the load and motor inertia; mitigating inelastic collisions experienced within gear trains during impact and increasing the energy efficiency of the actuator and reducing the system's cost of transport [48]. To achieve backdrivability, elastic actuators are required to utilize DD or QDD transmissions to ensure the impeding factors experienced within gearboxes are reduced or eliminated.

However, the increased stiffness provided by these actuator contributes to their downfall, as the control bandwidth of the system is inversely proportional to the spring stiffness [8]. Therefore, the accuracy of force proprioception decreases with an increase in spring stiffness due to the low control bandwidth. Notably, the low control bandwidth experienced by elastic transmissions is undesirable for transient maneuvers as the robot is required to rapidly re-orientate its legs during motion.

2.4. Artificial Restraint Systems

Legged robotic platforms often require support or artificial restraint during initial development and testing within laboratories to assist in maintaining static and dynamic stable states. These artificial restraint systems serve as a protective measure by reducing the damage inflicted on robots through falling. This is achieved by constraining the motion of the robot to operate within a singular two dimensional plane, specifically the sagittal plane. Artificial support structures also enable simple position, velocity and acceleration sensing to capture the performance of the platform and provide the necessary data required by the control algorithms. Notably, legged robotic research fails to emphasize the importance of these support systems and often remains undocumented [56]. Artificial restraint systems can be categorized into three different types as shown Figure 2.6, namely pivot axis boom support, 2-D planarizer support and overhead tethered supports.

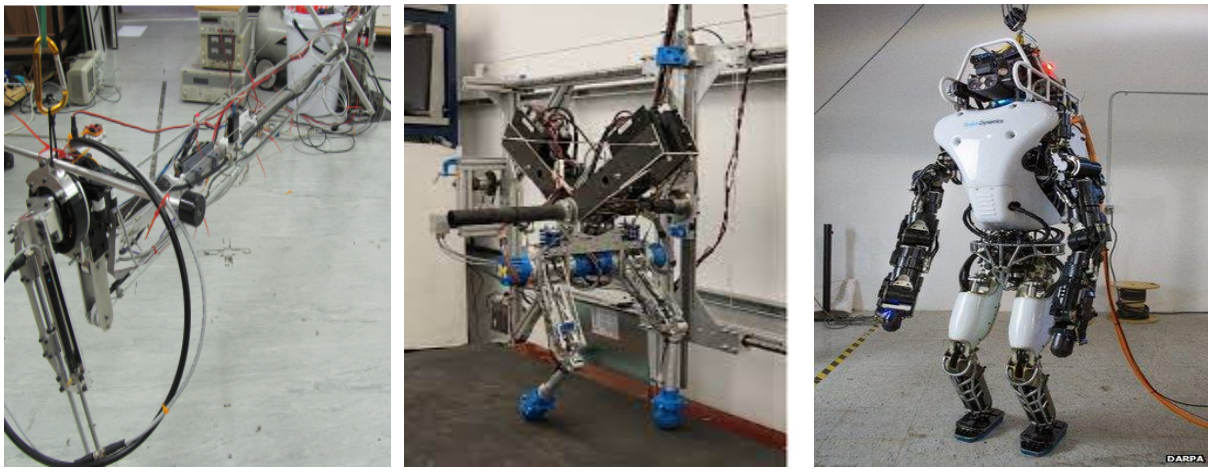

(a) **(b)** **(c)**

Figure 2.6: A comparison of the different artificial restraint system investigated in this section. (a) A pneumatic planar hopping robot supported by a boom arm system. (b) The bipedal robot, RAMone, supported by a vertical gantry 2-D planarizing system. (c) The Atlas robot developed by Boston Dynamics, supported by an overhead tethered system. Images from [4, 57, 58].

This section aims to investigate the existing artificial restraint systems used in the development of legged robots to identify relative distinctions between the various methods.

Furthermore, restraint systems should not impose on the planar dynamics of the robot and should aim to have a negligible effect on the system [44].

2.4.1. Pivot Axis Boom Systems

The pivot axis boom system is the most common approach for supporting planar motion in robots and has been used to support platforms such as Spring Flamingo, Baleka and ERNIE [28, 59, 60]. These systems present two types of booms namely, a single boom arm and a four bar linkage boom arm as shown in Figure 2.7. While numerous design variations exist for these systems, the basic system features include a boom arm that connects to a central gimbal, which can either be grounded or in an elevated configuration and allows the the robot to travel in a circular motion [56]. This allows the boom to maintain the vertical orientation of the robot tangential to the circumference of the circular path of motion during testing. Therefore, as the length of the boom arm increases, the straighter the motion of the robot becomes [4].

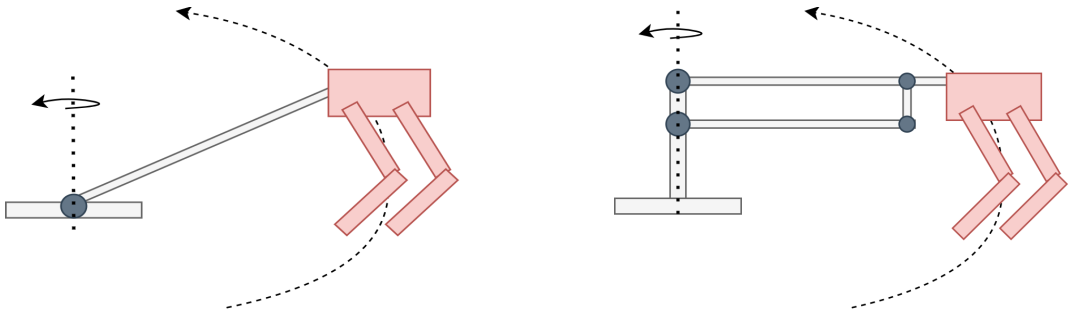

(a) Grounded single boom arm. **(b)** Elevated four bar linkage boom arm.

Figure 2.7: An illustration of the different boom types in the grounded and elevated configuration, along with the circular range of motion produced by this form of robotic support.

However, common problems arise in these systems with increased boom lengths as flexing occurs in the boom arm, corrupting sensor readings and contributing undesirable dynamics to the system [56]. In addition, the robot is required to accelerate and support the effective weight and inertia of the boom arm during maneuvers, which can significantly affect the behaviour of the robot [4]. Despite these downfalls, the problem of flexion and additional mass have been accounted for in the past by gravity compensation, involving the addition of counterweights to the gimbal end of the boom. Although, this often requires a larger, rigid boom with a reinforced base or the use of cable reinforcements as seen in Figure 2.6a.

2.4.2. 2-D Planarizer Systems

Vertical 2-D planarizing systems are an alternative solution to supporting planar robots. These systems have typically been used in combination with treadmills to provide robots the ability to walk and run on the spot, while constrained in the sagittal plane as seen by the MIT Cheetah and RAMone [57, 61]. This has been achieved through the implementation of a fixed boom arm or vertical gantry assembly located perpendicular to the treadmill, limiting the motion of the robot to the surface of a rectangular plane. In addition, vertical gantry assemblies can be used in scenarios involving normal ground contact. As the linear bearings of the gantry enable vertical and horizontal translation and require a simple pivoting connection to the robot as seen in Figure 2.6b. However, the sliding motion exhibited in gantry systems is limited to the length of the guiding rail and often comes at the cost of additional mass subjected to the robot. Despite efforts to lubricate the linear bearings, gantry systems still present minor friction which impedes on the dynamics of the robot [56].

On the contrary, treadmills mitigate bearing friction by eliminating the horizontal displacement of the robot as the foot travels over the the rotating treadmill belt. Furthermore, research has recommended operating treadmills at constant velocities to avoid influencing the dynamics of the robot and allowing the running motion to be mechanically equivalent to overground running [4, 56]. However, planarizing systems in combination with standard treadmills struggle to provide velocity consistency during the acceleration and deceleration phases of locomotion for large or heavy platforms due to stiction of the belt [56]. In addition, inertia treadmill have been used to explore acceleration and deceleration maneuvers, as standard treadmills only require the robot to leap into the air, while rapidly repositioning the legs and fails to accelerate the robots body mass. Notably, treadmills are considerably expensive and difficult to modify to account for testing on different terrains. Therefore, this type of restraint system is mainly suited for flat surface steady-state maneuvers.

2.4.3. Overhead Tethered Restraints

Unlike the pivot axis boom and 2-D planarizer systems, tethered systems are not constrained to the sagittal plane and are able to locomote in a higher dimensional space. Overhead tethered systems are generally implemented in humanoid and quadrupedal platforms designed to explore 3 dimensional maneuvers such as walking, jumping or turning within a confined environment to navigate around or over obstacles. This form of artificial restraint primarily serves as a safety mechanism to catch the robot when it falls to avoid inflicted damage on the platform.

Tethered restraint systems consist of an overhead gantry assembly, fitted with a centrally

located crane that attaches to the robot via a rope or cord. The suspended rope can be used to partially support the weight of the robot, while the crane is used to follow the robots motion; either through the use of an automated controller or a human operator. Notably, these gantry systems have typically been installed as fixed permanent structures within laboratories; however, mobile versions have been developed in the form of rolling gantry cranes as seen in the support system used by ATRIAS [42]. In addition, overhead tethered system have been used in combination with treadmills as seen in the MIT Cheetah 3 [33] and MIT Mini Cheetah [32]; however, these treadmills exhibit the same downfalls as mention in Section 2.4.2.

2.5. Legged Robotic Control Templates

Legged robotic control is presented as a challenging task due to the hybrid dynamic nature and underactuation of the system during phases of stance and flight [27, 62]. Therefore, control templates have been introduced as simplified models containing dynamic properties to resemble and reduce the complexity of the physical system. Over the past 30 years, robotic literature has shown the development and implementation of numerous control schemes based on templates used to embody walking and running gaits in legged robots with various degrees of success. In most cases, the developed control schemes draw inspiration from Raibert's simplistic control architecture, developed for the first truly dynamic legged robots and utilized three decoupled, parallel 1-DoF controllers [27, 62]. Raibert's algorithm, detailed in Chapter 6, is based on the SLIP model template and is used to regulate the forward velocity, hopping height and body attitude of the robot.

However, a vast amount of the developed control schemes utilize trajectory tracking methods, which are susceptible to two primary downfalls. The first drawback to this control scheme is that it's computationally expensive, as the dynamic equations of motion (EoM) for robots containing multiple degrees of freedom (DoF) become difficult to solve and may fail to converge at a local point of feasibility [63]. Additionally, robots controlled using trajectory tracking techniques lack robustness against disturbances and perturbations subjected to the system [63]. Therefore, this section serves to investigate the simplistic control templates used to embody highly dynamic locomotion in legged robotics.

2.5.1. Spring-Loaded Inverted Pendulum Model

The spring-loaded inverted pendulum model is a low-order, bio-inspired model used to capture the dynamics observed by the centre of mass (CoM) of animal locomotion [62]. In biomechanics and robotics, the SLIP model has effectively been implemented as a descriptive model and simplistic control gait template to investigate the dynamics of

compliant legged movements [64, 65]. The SLIP model, as shown in Figure 2.8, can be represented by a massless prismatic spring with a stiffness, k and dashpot with damping, c, connected to a point mass body. In addition, the foot of the SLIP model is assumed as a point at the end of the prismatic spring and mitigates the effect of sliding during ground contact, while the motion of the CoM generates a parabolic trajectory during flight.

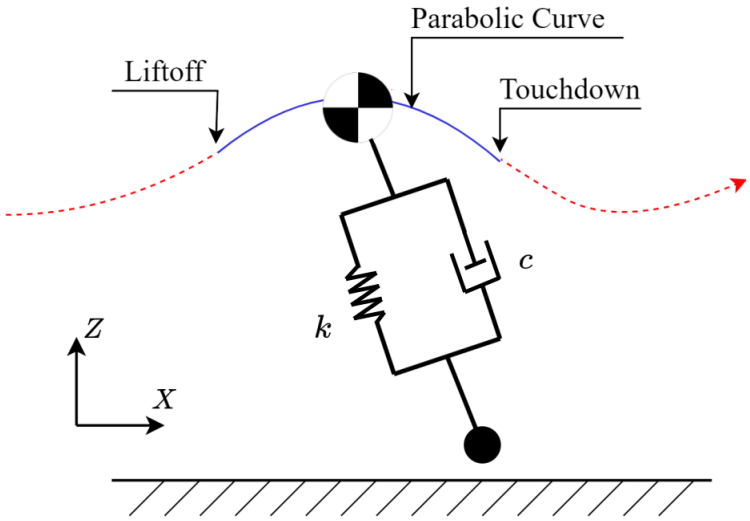

Figure 2.8: The spring-loaded inverted pendulum model at the apex of flight, consisting of a point mass, spring and damper.

Under transient circumstances involving rapid acceleration and deceleration maneuvers, the compliant nature exhibited by the SLIP model enables robots to accommodate disturbances using lower actuator efforts without infringing on the unilateral ground contact constraints [62]. This allows the SLIP model to achieve a continuous constant velocity and apex height irrespective of the terrain conditions; by dynamically adjusting the joint stiffness of the model to maintain the stable periodic motion [65]. This is evident in the stability and balance displayed within the agile walking gait of the ATRIAS robot which embodies the SLIP model template [54]. Additionally, the Baleka robot was capable of emulating highly dynamic acceleration and deceleration maneuvers in the form of alternating hopping through the implementation of the SLIP model [59].

2.5.2. Virtual Model Controllers

Unlike trajectory tracking techniques, virtual model control is a template based control architecture commanded by the external forces of the system; which is a softer control approach in comparison to typical positional controllers [63]. Virtual model control has become a common technique used to validate the dynamic capabilities of newly developed legged robotic platforms as seen in the initial control of robots such as Spring Flamingo, Baleka, GOAT and Solo [3, 8, 28, 66]. This control architecture avoids complex dynamic system modelling through the implementation of the SLIP model and relies on

the application of forces at the correct time intervals. Therefore, virtual model controllers are composed into two control components, namely a high-level controller and low-level controller as shown in Figure 2.9.

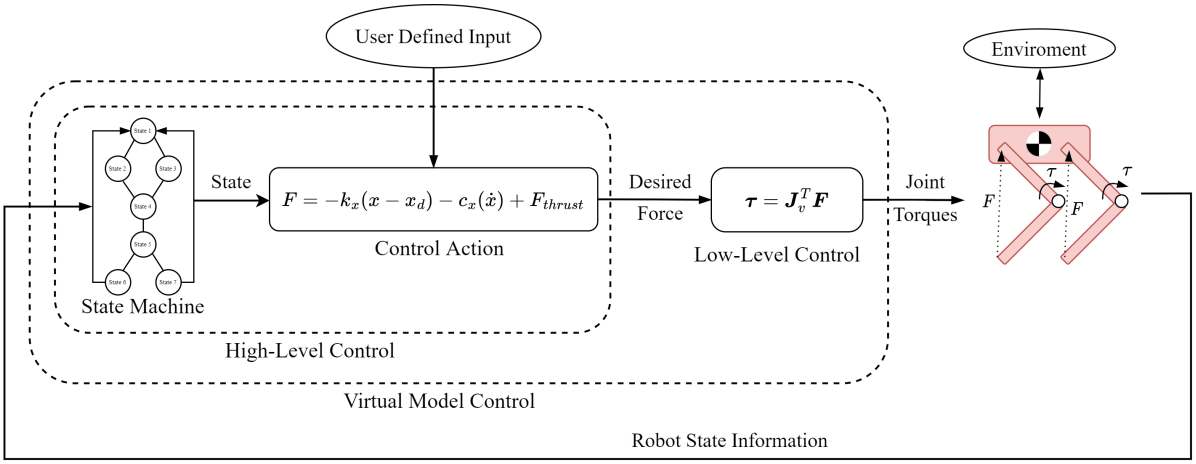

Figure 2.9: The virtual model control architecture indicting the flow of control between the high level and low level controllers. Note, the control action implemented in this architecture is based on the SLIP model template.

The high-level controller is responsible for determining the virtual force vector required to produce the desired robotic motion. This is implemented via a sequential state machine in combination with a control action; which ensures the desired forces are applied at the correct time based on the state information of the robot. Whereas, the low-level controller is responsible for applying the desired virtual forces determined by the high-level control action. The calculated virtual forces are essentially mapped to the joint torques of the robot through the relationship of the transposed Jacobian ($\boldsymbol{J}_v$) with respect to the virtual components of the leg as follows:

$$\boldsymbol{\tau} = \boldsymbol{J}_v^T \boldsymbol{F}. \tag{2.2}$$

Once the joint torques are mapped to the robot, the platform is able to interact with the environment and adjust the joint stiffness accordingly in the event of an external disturbance. This characteristic embodied through the use of the SLIP model effectively increases the robustness of virtual model control, allowing the robot to maintain compliant locomotion. Further details regarding the implementation of virtual model control are discussed in Chapter 6.

2.6. Trajectory Optimisation

Trajectory optimisation refers to a numerical technique used to satisfy a set of constraints, imposed by the environment and hardware elements of a robot, in computing an optimal

solution to an open loop control problem; which can be executed on a physical platform and in simulation [10]. Therefore, the motions and forces generated by the optimizer using the defined high level constraints have been embraced by the legged robotics community as a powerful tool in developing motion planners, inspiring robotic controllers and validating performance feasibility in robots [67, 68].

Trajectory optimisation techniques have employed two distinct methods to achieve optimal continuous control solutions, namely direct and indirect methods. The difference between these methods is that direct methods are used to discretize the problem into a non-linear program prior to optimizing; whereas, indirect methods are used to analytically construct optimized conditions prior to discretizing the problem [69]. The research conducted in this thesis follows the direct method approach to solving the optimisation problem. Furthermore, the optimizer is provided with bounds to limit the solution search range for each of the defined variables, along with an objective cost function used to maximize or minimize a measure of performance such as energy, force or time [12, 69]. Upon initialization, the solver is provided with a randomized seed of variables, varied within the defined bounds until each of the system constraints have been satisfied to produce a feasible solution [4]. Lastly, the feasibility of the obtained solution is only deemed optimal once the performance measure defined by the cost function is successfully minimized.

Research conducted in Winkler et al. [70], presented a trajectory optimisation formulation for phase-based end-effector parameterization used to practically validate the feasibility of generated motions on the ETH Zurich ANYmal robot. The trajectory optimisation problem isolated the influence of the feet location and force of the centroidal dynamics of the robot to optimize the motion of the feet over a discrete gait sequence. The motion tracking of the trajectory was implemented on the platform through the use of a simple proportional and derivative (PD) controller by utilizing the optimized footholds as reference positions. The optimisation results produced feasible contact solutions for walking and trotting motions on even and uneven terrains and were validated in both simulation and on a physical hardware system.

Further trajectory optimisation research involving the ANYmal robot was conducted in Carius et al. [67] and presented a trajectory optimisation method for sliding contact states observed in legged robots. The optimisation problem placed focus on the unilateral contact interactions presented in the generalized, articulated robot configuration and demonstrated motions that overcame the typically no-slip conditions seen in legged robotic motion [67]. Notably, the achieved solutions enabled the robots motion to allow for slippage based on the experienced contact surface. Furthermore, the feasibility of the exploited sliding

contact trajectories were practically verified and evaluated on a physical hardware system. Lastly, this research revealed how trajectory optimisation can be used as a dominant tool to explore movements, which are not specifically addressed in the generation of legged locomotion.

2.7. Summary

This chapter detailed the relevant robotic literature required to created a stable foundation for the author of this thesis to proceed with the design process of the bipedal robot. Firstly, this chapter began with a thorough review of the evolution of legged robotics, identifying legged robotic inspiration and observing the dynamic capabilities seen in platforms. An investigation into compliant leg design principles was performed and revealed speed, torque density and mechanical impedance as influential factors in the design of high power legs. While characteristics such as mechanism compliance, robustness and force proprioception were identified as desirable features in the design of legged robots. Thereafter, the numerous electric actuation and transmission strategies were investigated to identify various trade-off for the respective strategies. The different artificial restraint systems used to support robots were covered and the various control templates used to embody dynamic motion were addressed. Lastly, the chapter concluded with with use of trajectory optimisation in legged robots.

Chapter 3

Methodology

This project was divided into four distinct focal areas consisting of several specified subsets used to structure the development and verification of a dynamic and agile series articulated bipedal robot. These four focal areas included:

1. A detailed system design comprising of actuation, structural and support features.
2. An inspired controller design.
3. A trajectory optimisation verification simulation.
4. System testing and validation.

This chapter outlines the overall project requirements and individual approaches followed throughout each focal aspect of this thesis to govern the development and performance validation of Q-Bert.

3.1. Platform Requirement Identification

The extensive literature investigated at the start of this thesis, as detailed throughout Chapter 2, provided the necessary insight required to initiate the design process of the robot. Hence, the characteristics and attributes seen within existing highly dynamic legged robots were used to inspire and formulated the platform requirements of the design. However, as with every design process, certain factors require prioritization over others to achieve the desired outcome.

Evidently, the identified platform requirements shown in Table 3.1 were categorized into two subsets, namely transmission objectives and system objectives. Where the transmission objectives directly influence the actuation requirements of the leg and the system objectives related to the overall robot design. Additionally, each of the identified requirements were given a priority scale out of five to indicate the different levels of importance during the design process. Furthermore, the platform requirements are presented in an independent manner to guide the design process rather than eliminate possible solutions before the design process has even started.

Table 3.1: The platform requirements used to govern the design of the bipedal robot for agile and transient maneuvers. A rating of 1 on the priority scale indicates a minimal level of importance; whereas a rating of 5 indicates maximum importance.

No.	Project Requirement Description	Priority Scale /5
	Transmission Objectives	
1.	High force proprioceptive actuators.	4
2.	High closed loop control bandwidth to enable accurate proprioception.	3
3.	High torque and speed output.	5
4.	Low reflected inertia to minimize loss due to friction, impedance and cogging.	2
	System Objectives	
5.	Highly robust leg mechanism to withstand detrimental ground impacts.	4
6.	Low structural mass and inertia of the body and limbs to allow rapid leg transitions.	5
7.	Modular leg design to enable simplistic system expansion.	1
8.	Produce actively compliant agile and transient motions to validate the system performance.	3
9.	Constrain the planar motion of the robot within the sagittal plane and provide additional support.	4

3.2. System Design

The system design of the platform was categorized into three main subsets which included the actuation and transmission strategy of the robot, along with the mechanical design and artificial restraint system implementation. The approaches taken to address each of these factors within this thesis will be detailed in this section.

3.2.1. Actuation and Transmission Selection

To achieve highly dynamic and transient legged motion, numerous design principle trade-offs needed to be balanced, as detailed in Section 2.2.1, which explicitly involved the actuation and transmission strategy of the robot. For the developed series articulated platform to embody these desired characteristics and motions, a minimum of four electric actuators were required to successfully produce agile and transient maneuvers.

The actuation and transmission selection formed the first stage of the design process due to its crucial impact on the dynamic and agile performance of the platform. Therefore, with the help of an incremental analytical analysis of the robot configuration developed in Chapter 4; the analytical jumping height produced by various actuators was examined.

This ensured that a high powered actuation strategy was carefully selected and effectively balanced all the desired transmission objectives listed in Table 3.1.

3.2.2. Mechanical Design

A large window of opportunity was presented within this research to explore various design options to produce a low-cost platform for future generations to adapt and expand on within the Electronic Systems Laboratory (ESL). However, a decision regarding the leg topology was made at the start of this research to embody the series articulated mechanism due to the resemblance of animal and human anatomy [2].

A desired conventional linkage length was determined for the limbs of the leg through the analytical analysis used to aid the actuator selection of the robot. This was followed by an iterative concept development phase, involving numerous concept reviews with the assistance of the Stellenbosch University electronic department workshop foreman to ensure manufacturability and to avoid expensive machining processes. Additionally, certain features of the design were considered for 3D printing during the design process to accelerate the prototyping phase and assess the viability of components.

Furthermore, a finite element analysis was conducted on the final prototype design to ensure the structural integrity of the limbs, according to a defined mechanical safety factor before compiling a comprehensive drawing pack for manufacturing. Once the fabricated components were acquired from the workshop, the modular monopedal unit was assembled and further expanded to a biped following the initial conducted experiments.

3.2.3. Artificial Restraint System Design

To support and constrain the robot in a two-dimensional plane, specifically the sagittal plane; an artificial restraint system was required. Upon investigating and comparing the existing methods of restraint discussed in Section 2.4, a custom planarizing cart system was designed to combine the boom arm and planarizing strategies into a single concept. This enabled the boom arm to vertically support the robot in the sagittal plane, while the planarizing cart provided the system with the ability to track the robots trajectory without impeding on the dynamics of the robot. The developed restraint system was designed to be structurally simplistic, light weight and rigid; therefore, materials such as aluminium extrusion and 3D printed components were considered for the design. Furthermore, the design process of the artificial restraint system attempted to mitigate deflection and influence factors experienced by traditional boom arm systems to increase the systems overall performance.

3.3. Controller Design

A virtual model control template was inspired through Raibert's hopping control algorithm and selected to implement the robots dynamic maneuvers [27]. This allowed the designed controller to expose the robot to high impact forces experienced during transient motion to validate the system robustness and control stability. As detailed in Section 2.5.2, the virtual model controller consisted of a sequential state machine implementation together with an impedance control action and low-level torque-mapping controller; which were executed on a Teensy 4.0 micro-controller at a control frequency of 100 Hz. Additionally, the control template was modified to accommodate testing on both the monopod and biped robots, while the low-level torque mapping controller was simulated in MATLAB's Simulink environment prior to implementation. This was used to verify the applied torques due to the control action and assess the behaviour of the controller parameters.

3.4. Trajectory Optimisation Verification

This section describes the methods used to create and simulate the trajectory optimisation setup of the robot for dynamic maneuvers to validate the physical robots accelerating capabilities during transient motions. The generated trajectory optimisation simulation was inspired and based off existing frameworks, which enabled the implementation of the SLIP model [4, 10]. An illustration of the SLIP model utilized throughout the optimisation simulation can be seen in Figure 3.1 and consisted of a decoupled spring-damper system with a fixed point mass body (m_{body}) and leg mass (m_{leg}). In addition, the simulated periodic motion of the robot was stitched together to form a long-time-horizon task comprising of three individual trajectory tasks, namely an acceleration phase, steady-state phase and deceleration phase as proposed by Fisher et al. [4, 71]. This required post-processing in to stitch each of the generated trajectories together to form the long-time-horizon trajectory of the desired robotic motion. The following subsections will detail the integration of the robot's dynamics into the optimisation environment, along with the discretization process, constraints and conditions used to generate the desired trajectories.

3.4.1. Dynamics

The equations of motion (EoM) describing the simulated model were determined using Euler-Lagrange dynamics in the form of the manipulator equation shown below [4]:

$$\boldsymbol{M}(\boldsymbol{q})\ddot{\boldsymbol{q}} + \boldsymbol{C}(\boldsymbol{q}, \dot{\boldsymbol{q}})\dot{\boldsymbol{q}} + \boldsymbol{G}(\boldsymbol{q}) = \boldsymbol{B}\boldsymbol{\tau} + \boldsymbol{A}\boldsymbol{\lambda}. \tag{3.1}$$

Where $\boldsymbol{M}(\boldsymbol{q})$ represents the mass matrix of the system, $\boldsymbol{C}(\boldsymbol{q}, \dot{\boldsymbol{q}})$ describes the Coriolis matrix and $\boldsymbol{G}(\boldsymbol{q})$ represents the gravitational potential matrix of the system. The systems

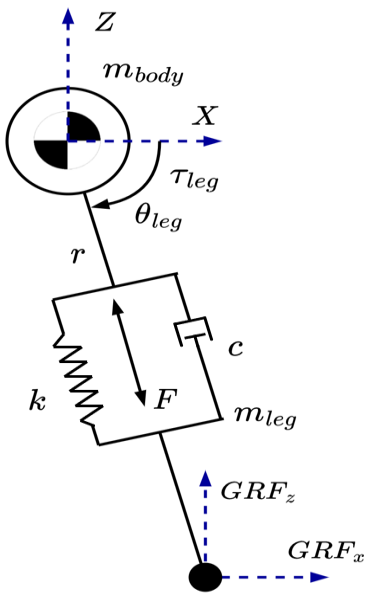

Figure 3.1: A representation of the SLIP model used in the trajectory optimisation simulation showing the models generalized coordinates, along with the applied forces and torques.

ground reaction force (GRF) was represented by $\boldsymbol{\lambda}$ and utilized the $\boldsymbol{A}$ matrix to map the respective external forces; whereas the applied system torques and forces represented by $\boldsymbol{\tau}$ were mapped to the generalized coordinates using the $\boldsymbol{B}$ matrix. Additionally, the robots generalized coordinates, denoted by $\boldsymbol{q}$, consisted of the following components:

$$\boldsymbol{q} = [X, Z, r, \theta_{leg}]^T. \tag{3.2}$$

Furthermore, as the robot was constrained within the sagittal plane the components for the applied torques and forces ($\boldsymbol{\tau}$) and GRF ($\boldsymbol{\lambda}$) were reduced to the following:

$$\begin{aligned} \boldsymbol{\tau} &= [\tau_{leg}, F]^T, \\ F &= F_{applied} + k(r_{neutral} - r) - c\dot{r}, \\ \boldsymbol{\lambda} &= [\lambda_x, \lambda_z]^T. \end{aligned} \tag{3.3}$$

Due to the SLIP model implementation, the force, F, became a function of applied force in combination with the contributing spring force represented by the spring constant k, which was multiplied by the change in length (r) from the initial neutral length of the leg ($r_{neutral}$). Lastly, the force of the leg was limited by the damping component of the model, which was a product of the damping coefficient (c) and speed of the leg ($\dot{r}$). Further details regarding the computation of the EoM can be found in Appendix A.

3.4.2. Generating The Optimisation Model

As discussed in Section 2.6 of the literature study, trajectory optimisation is a numerical technique used to compute an optimal trajectory solution, while satisfying numerous bounds, constraints and a predefined cost function. The optimisation problem was generated and solved using Pyomo [72], which is an open source Python package that makes use of the IPOPT solver to compute optimal solutions.

The direct method of optimization was utilized in this thesis and discretized each of the trajectories into N node points, which represented the number of discrete time-steps used to compute an optimal solution. The implemented number of N points for the computed trajectories ranged between 30 and 70 nodes depending on the optimized task to ensure sufficient solving time for comprehensive solutions. Hence, a variable time-step was implemented to allow a flexible time-step duration amongst the discrete nodes as shown in Equation 3.4.

$$\begin{aligned} 0.5h_M \leq h(i) \leq 1.5h_M, \\ tt(i,j) = tt_0(i) + h(i)\sum_{k=1}^{3} \boldsymbol{a}(k,j), \\ tt_0(i) = tt(i-1,3). \end{aligned} \tag{3.4}$$

Where $h(i)$ represents the duration of the i-th node ($i \in [1, N]$) and h_M is equivalent to $\frac{T}{N}$, which utilizes T as an estimated scaling time factor for each discretized time-step based on the optimization task. Furthermore, a 3-point collocation technique ($j \in [1, 3]$) was utilized to join the node points along a trajectory and can be seen in $tt(i, j)$; which represents the time duration of the trajectory from start to the relevant i-th node and j-th collocation point. Lastly, $tt_0(i)$ is used to align the time value of previous node's third collocation point to the current node's time value. A graphical explanation of the variable time-step and discretization process can be seen in Figure 3.2 and shows how the trajectory is divided into node points(i) and collocation points (j).

Discretization and Collocation

During the discretization process, each of the trajectory tasks were divided into N number of node points and integrated using a third order polynomial through the implementation of a 3-point collocation technique [73]. This allowed the optimizer to increase the accuracy of trajectory solution without significantly effecting the complexity of the problem [12, 69]. The 3-point collocation was achieved using a Runge-Kutta basis with three-point Radau techniques to solve the differential dynamics of the model represented by Equation 3.1 [73, 74]. The three-point collocation matrix of the Radau technique, represented by $\boldsymbol{a}$

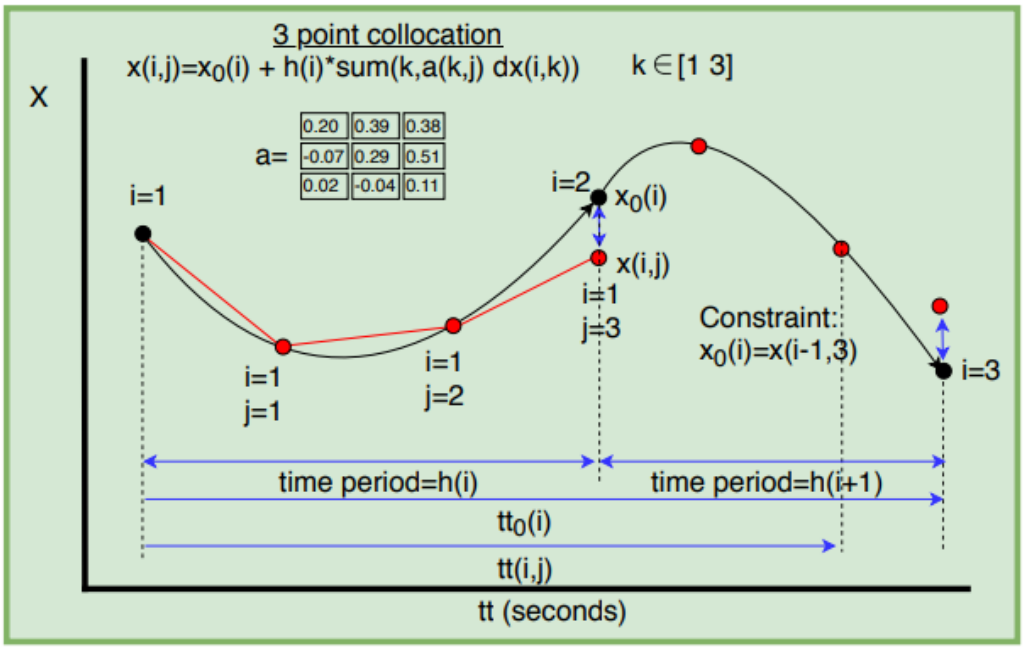

Figure 3.2: An illustration of the discretization process showing how the trajectory is divided into numerous node points (i) and collocation points (j). Image from [4].

is denoted as follows:

$$\boldsymbol{a} = \begin{bmatrix} 0.19681547722366 & 0.39442431473909 & 0.37640306270047 \\ -0.06553542585020 & 0.29207341166523 & 0.51248582618842 \\ 0.02377097434822 & -0.04154875212600 & 0.11111111111111 \end{bmatrix}. \tag{3.5}$$

Furthermore, the Radau technique was implemented to each generalized coordinate state ($\boldsymbol{q}$ and $\dot{\boldsymbol{q}}$) for the relevant trajectory tasks through the following equations:

$$\begin{aligned} \boldsymbol{q}(i,j) &= \boldsymbol{q}_0(i) + h(i)\sum_{k=1}^{3} \boldsymbol{a}(k,j)\dot{\boldsymbol{q}}(i,k), \\ \dot{\boldsymbol{q}}(i,j) &= \dot{\boldsymbol{q}}_0(i) + h(i)\sum_{k=1}^{3} \boldsymbol{a}(k,j)\ddot{\boldsymbol{q}}(i,k). \end{aligned} \tag{3.6}$$

$$\begin{aligned} \boldsymbol{q}_0(i) &= \boldsymbol{q}(i-1,3), \\ \dot{\boldsymbol{q}}_0(i) &= \dot{\boldsymbol{q}}(i-1,3). \end{aligned} \tag{3.7}$$

Where Equation 3.6 is used to implement the three point Radau technique to integrate the dynamic EoM and Equation 3.7 ensures that the third collocation point of the current node (i) is situated at the same location as the following node ($i+1$) to enable a continuous trajectory solution.

Cost Function

For a computed solution to become optimal, the optimizer must minimize a desired measure of performance defined by the cost function (J_{cost}). For the transient motions generated within in this research, an energy based cost function scaled by the maximum system torque and was employed as follows:

$$J_{cost} = \sum_{i=1}^{N} \left(\frac{\tau(i)}{\tau_{max}} \right)^2 h(i). \tag{3.8}$$

3.4.3. Constraints and Bounds

Numerous constraints and bounds were defined throughout the optimisation problem to describe and limit the motion of the trajectories. However, the most relevant constraints relating to the actuation and implicit contact determination of the model are defined in this section, along with several system boundary limits.

Motor Model

To ensure the comparative applicability of the computed trajectories for robotic applications, a motor model comprising of a linear power model was implemented to account for the no-load speed and stall torque trade-off of the selected motor [4, 75]. The motor model was implemented through the following constraint:

$$-\tau_{max} - \frac{\tau_{max}}{\omega_{max}}\omega(i) \leq \tau(i) \leq \tau_{max} - \frac{\tau_{max}}{\omega_{max}}\omega(i). \tag{3.9}$$

Where, τ_{max} and ω_{max}, respectively represent the specified stall torque and no load speed of the selected motor. Whereas, $\tau(i)$ and $\omega(i)$, respectively denote the applied torque and angular velocity at the i-th discrete node.

Complementarity Constraints

The implicit contact optimisation method used to determine the rigid contact events and foot slippage of the model was implemented through the use of complementarity constraints. Which enabled the optimizer to decide when contact occurred by evaluating two decision variables (α and β) with respect to each other and evidently allowed the optimizer to produce more robust solutions. The principle of complementarity is defined as follow [76]:

$$\alpha(i)\beta(i) \leq 0. \tag{3.10}$$

Notably, both α and β were constrained to be positive variables and were evaluated at each node according to Equation 3.10 to be less than or equal to zero. Evidently, this allowed one variable to contain a value while the other variable was forced to zero. In

the case of ground contact, α and β were replaced by the height of the foot and the vertical component of the GRF. Hence, as the height of the foot became zero and made contact with the ground, the relevant GRF could be applied to the system. Similarly, once the foot broke contact with the ground to resume an arbitrary height value, the GRF would return to zero as stipulated by the complementarity constraint. However, to improve the convergence time of the trajectory solution; the complementarity principle was modified to employ a regularization technique known as ϵ relaxation [4, 77]. This allowed the complementarity constraints to be solved iteratively by dividing ϵ by a factor of 10 upon each successful solve and resulted in the following adjusted principle:

$$\alpha(i)\beta(i) \leq \epsilon \tag{3.11}$$

Complementarity constraints were used to determine the vertical and horizontal GRF components of the model; however, this required the horizontal contact component of the foot to be separated into a positive and negative component. Evidently, this resulted in a re-defined GRF consisting of positive variables as shown below:

$$\begin{aligned} \lambda = [\lambda_x^+ - \lambda_x^-, \lambda_z]^T, \\ \lambda_z, \lambda_x^+, \lambda_x^- \geq 0. \end{aligned} \tag{3.12}$$

Furthermore, a friction cone was enforced while determining the systems GRF and utilized a coefficient of friction ($\mu = 0.95$) inline with the silicone rubber material of the physical robots foot. The friction cone was applied through the following constraint [11]:

$$\mu\lambda_z - \lambda_x^+ - \lambda_x^- \geq 0. \tag{3.13}$$

Subsequently, this enabled an equilibrium between the GRF components by ensuring the X-components were equivalent to the Z-component multiplied by the friction coefficient. Additionally, the constraints shown below in Equation 3.14 were used to determine the magnitude of the relative tangential velocity during contact.

$$\begin{aligned} \dot{\boldsymbol{X}}_{foot} + \dot{X}_{foot} \geq 0, \\ \dot{\boldsymbol{X}}_{foot} - \dot{X}_{foot} \geq 0, \\ \dot{\boldsymbol{X}}_{foot} \geq 0. \end{aligned} \tag{3.14}$$

Where $\dot{\boldsymbol{X}}_{foot}$ represents the magnitude of the foot's relative velocity and $\dot{X}_{foot}$ represents the relative tangential velocity of the foot. This was followed by the constraint shown in Equation 3.15, which ensured the computed friction force was located on the friction cone when the foot slides.

$$(\mu\lambda_z - \lambda_x^+ - \lambda_x^-)^T \dot{\boldsymbol{X}}_{foot} = 0. \tag{3.15}$$

Lastly, to ensure the horizontal component of the GRF opposed the sliding motion of the foot, two complementarity constraints were enforced as follows:

$$\begin{aligned}(\dot{\boldsymbol{X}}_{foot} + \dot{X}_{foot})^T \lambda_x^+ = 0,\\ (\dot{\boldsymbol{X}}_{foot} - \dot{X}_{foot})^T \lambda_x^- = 0.\end{aligned} \tag{3.16}$$

System Bounds

Numerous system bounds were defined within realistic ranges to comply with the actuation limitations of the physical robot. Evidently, this reduced the search domain for each of the optimized variables and assisted the solver in computing a feasible and optimal solution. Notably, the variable bounds minimized the possibility of unfeasible values emerging upon solver start up, which could have resulted in a failure to converge at a feasible or optimal solution. Each of the variables forming the generalized coordinates, along with their velocities were bounded in the following manner:

$$\begin{aligned}lower\ bound \leq \boldsymbol{q} \leq upper\ bound,\\ lower\ bound \leq \dot{\boldsymbol{q}} \leq upper\ bound.\end{aligned} \tag{3.17}$$

The exact defined bounds for each of the variables forming the generalized coordinate of the system can be found in Appendix A. Furthermore, the vertical (λ_z) and horizontal (λ_x) ground reaction forces were bounded within a suitable range to not exceed 10 times the total weight of the robot as shown below:

$$\begin{aligned}-10 \cdot m_{robot} \cdot g \leq \lambda_x \leq 10 \cdot m_{robot} \cdot g,\\ 0 \leq \lambda_z \leq 10 \cdot m_{robot} \cdot g.\end{aligned} \tag{3.18}$$

Lastly, to enable a comparison between the physical robot and the optimized solution; the systems applied force was bounded according to the robot's desired thrust force of 250 N as follows:

$$-250 \leq F_{applied} \leq 250. \tag{3.19}$$

3.4.4. Initial and Terminal Conditions

The initial and terminal conditions used to generate each of the trajectory optimisation maneuvers varied based on the computed task. The position and velocity constraints used to define the robots generalized coordinate conditions for the acceleration, steady-state and deceleration states are provided below.

1. Acceleration Phase Trajectory: The state initialization occurred at rest and termina-

tion was enforced at the steady-state trajectory apex height denoted as follows:

$$\begin{aligned} \boldsymbol{q}_0(1)_{Acc} &= \boldsymbol{q}_{rest}, \\ \dot{\boldsymbol{q}}_0(1)_{Acc} &= \dot{\boldsymbol{q}}_{rest} = 0, \\ \boldsymbol{q}_0(N)_{Acc} &= \boldsymbol{q}_0(1)_{ss}, \\ \dot{\boldsymbol{q}}_0(N)_{Acc} &= \dot{\boldsymbol{q}}_0(1)_{ss}. \end{aligned} \tag{3.20}$$

2. Steady-State Phase Trajectory: The state initialization for a vertical hopping maneuver occurred at the apex height and termination was enforced to match the initial conditions of the maneuver, generating periodic motion denoted by the following:

$$\begin{aligned} X_0(1) &= 0, \\ \dot{Z}_0(1) &= 0, \\ \dot{X}_0(1) &= 0, \\ \boldsymbol{q}_0(N)_{ss} &= \boldsymbol{q}_0(1)_{ss}, \\ \dot{\boldsymbol{q}}_0(N)_{ss} &= \dot{\boldsymbol{q}}_0(1)_{ss}. \end{aligned} \tag{3.21}$$

3. Deceleration Phase Trajectory: State initialization occurred at the steady-state trajectory apex height and termination was enforced at the models rest orientation denoted as follows:

$$\begin{aligned} \boldsymbol{q}_0(1)_{Dec} &= \boldsymbol{q}_0(1)_{ss}, \\ \dot{\boldsymbol{q}}_0(1)_{Dec} &= \dot{\boldsymbol{q}}_0(1)_{ss}, \\ \boldsymbol{q}_0(N)_{Dec} &= \boldsymbol{q}_{rest}, \\ \dot{\boldsymbol{q}}_0(N)_{Dec} &= \dot{\boldsymbol{q}}_{rest} = 0. \end{aligned} \tag{3.22}$$

Further details regrading the specific initial and terminal conditions of each state can be found in Appendix A.

3.4.5. Solver Setup

The computed trajectory optimisation tasks were iteratively solved through the use of the ϵ-relaxation technique, to satisfy the system's complementarity constraints. The solving process was initiated by providing each of the optimisation tasks with an initial seed that was used to warm start the optimizer [4, 16]. This technique effectively allowed the optimizer to utilize feasible initialization points to assist in iteratively solving the systems complementarity constraints below the defined ϵ value. Once the optimizer had successfully solved the first iteration, the achieved feasible solution was then used as the seed to the following iteration of the solving process; comprising of 8 iterations. However,

initial seeds that generated infeasible solutions on the first iteration were discarded and the optimization process was restarted with a new seed.

At the start of the first iteration ϵ was set to 1000 and a cost function equivalent to 1 was employed, enabling the optimizer to optimally satisfy all the defined constraints and produce a feasible set of initial variables. Thereafter, the energy cost function was employed while ϵ was divided by a factor of 10 during each iteration of the solve process. Once the solver had successfully completed all 8 iterations with a final ϵ value equivalent to $1E-4$, the solution was saved and the systems complementarity constraints were considered to be solved within adequate tolerance.

Following the completion of each of the individually computed trajectory tasks, a long-time-horizon solution was stitched together to form the complete periodic trajectory maneuver [4]. Lastly, this was accomplished by appending the computed generalized coordinate positions and velocities of each of the trajectory phases to a single matrix, placing special attention on the X variable during the post-processing procedure to ensure periodicity.

3.5. System Testing and Validation

Once the mechanical mechanism, electronics, control system and restraint infrastructure were all primed for operation; the platform was powered and each of the sensors were sequentially initialized and integrated into the system. This ensured that each component was responding and operating as anticipated to mitigate the possibility of communication or sensor errors during testing; which could have catastrophic effects on the robot. With the entire system integrated and functioning, the robot was calibrated to set the home position of each motor encoder in the desired zero orientation of the limbs.

Following the calibration procedure, initial compliant disturbance and drop test experiments were conducted on the robot to observe the systems behaviour over a range of control parameters. Additionally, the force proprioceptive feedback attained from the motors was validated during the compliant drop tests by comparing sensor data with the proprioceptive feedback results. Once sufficient data responses were captured by the initial experiments, the control parameters required for the various hopping states could be selected for the sequential state machine used in the virtual model controller.

The final objective of this research was to validate the agile and transient capabilities of the developed robots. This was addressed through conducted single hop and periodic planar hopping maneuvers, while maintaining the robot in the sagittal plane. Firstly, the

single hop experiments were used to determine the agility performance of the developed robots with respect to numerous existing legged platforms, as higher jumping heights were considered to represent increased agility [5, 8]. In addition to verifying the systems agility, the single hop experiments validated the design process of the platform by comparing the analytical jumping height to the physical height of the robot. Lastly, the several periodic hopping experiments were conducted and compared to the trajectory optimisation simulation to verify the accelerating capabilities of the robot for transient motion and evaluate the systems robustness.

Chapter 4

Robot Design Analysis

Leg design is a crucial feature towards the success of walking and running robots. While there are several available leg design approaches for dynamic legged robots; bioinspiration forms the foundation of most developed platforms either based on the biomimetics of humans' or animals' leg morphologies [2].

Legged robotic design can be viewed as an integrated problem with trade-offs between the structural mechanism and actuation. During locomotion, a trade-off is experienced between the capability of the robot to withstand high ground reaction forces and the actuators ability to rapidly reposition the limbs of the robot. As seen in nature, biological structures effectively overcome this trade-off through high strength, low inertia limbs [26]. Consequently, high ground reaction forces along with other uncertainties introduced through terrain irregularities create high stresses, which propagate throughout the leg and pose the risk of structural failure.

This chapter aims to present the iterative leg design process of the series articulated platform with particular focus on the principles and procedures governing the actuator selection and structural design of the platform. In addition, emphasis was placed on decreasing the mass and inertia of the leg to reduce the mechanical impedance of the system. Since legged robotic actuators and mechanical transmissions are primarily responsible for their locomotion, an incremental analytical analysis of a two joint articulated model was developed to ensure an adequate actuator was selected based on the jumping performance of the model. The jumping height of the robot was seen as a crucial aspect in the design phase of legged robots, as vertical hopping can be seen as the foundation of a running gait or motion, and exhibits the overall dynamic characteristics during the stance phase of motion [78].

4.1. Design Requirements and Specifications

The design requirements and specifications for the mechanical design of the bipedal robot required additional elaboration apart from the overall project requirements mentioned in

Chapter 3. The requirements and specifications mentioned below, in no specific order, place emphasis on the processes and procedures, structural integrity, geometry constraints and actuator considerations which were used to characterize the mechanical design of the platform.

1. Minimize manufacturing cost. Therefore, expensive and complicated manufacturing methods were avoided to achieve a low cost design.
2. Introduce safety systems and protocols to protect expensive components from damage such as safety harnesses, emergency stops and implementing software limitations.
3. Design for a minimum mechanical safety factor of 2.
4. The length of the femur and tibia limbs must be limited within the following link range: $0.2 < L_{link} < 0.35$ m.
5. The gear ratio for motors should not exceed 10 : 1, to avoid increased reflected inertia and lack of backdrivability experienced in conventional actuators [79, 80].
6. High torque density actuator with relatively high speed output.
7. Robust and durable against ground impacts experienced during aggressive maneuvers.

To ensure manufacturing process costs were significantly reduced, the manufacturing of parts was limited within the capabilities of the Stellenbosch University electronic department workshop with the exception of outsourcing laser cut parts through external fabricators. The complexity of parts were maintained at a level which ensured ease of manufacturability and replicability. Reducing the complexity of parts simultaneously reduced the expected lead time for manufacturing. The iterative design phase accounted for the above mentioned requirements and specifications, ensuring caution was taken to avoid compromising the structural integrity of the design.

Furthermore, Figure 4.1 illustrates the interactions between the system requirements and influential design principles governing the design process with the aim of minimizing the critical parameters of the robot; which included the system mass and inertia. Similarly to the design principles addressed in the literature study, the design process desired factors such as high torque density, low mechanical transmission, mechanical robustness and a conventional leg length; which required the femur and tibia limbs to embody the same geometric length. Additionally, the critical parameters directly influenced the interactive energy of the system as heavier systems generate larger impacts upon landing and impede on the dynamic characteristics of the robot.

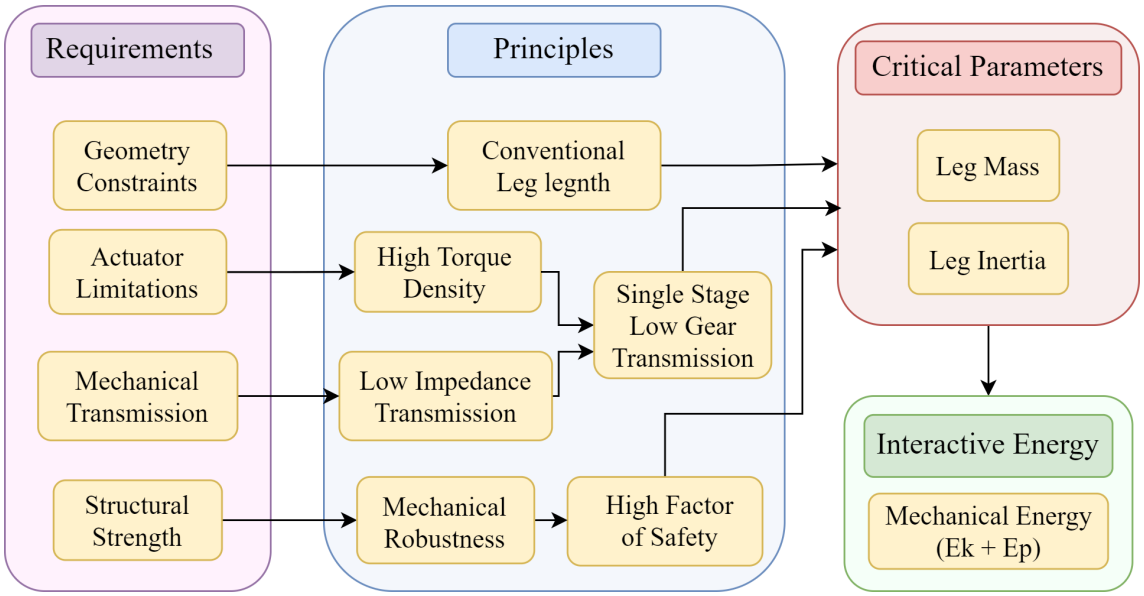

Figure 4.1: Design process flow diagram of the robot showing the interactions between the major design requirements and their respective design principles. The identified design principles each influence the critical parameters of the design process with the mass and inertia of the leg defining the mechanical energy of the system.

4.2. Articulated Leg Model

A simplified analytical model of the prototype platform was generated in MATLAB to assist in making an intuitive decision for the actuator selection. The simplified model proved to be advantageous by requiring less computational power due to the mitigation of time-based integration. Additionally, several assumptions were made to reduce the complexity of the model. Firstly, the symmetry of a bipedal robot about the sagittal plane allowed the model analysis to be reduced to a monopod, consisting of a two link leg and a torso [47, 81].

Monopedal models have been significantly favoured in the past, specifically constructed as testbeds in the design phase of bipedal robots for the purpose of testing model-based control techniques [41, 82]. The model assumed that the foot of the robot made contact with the ground at an ideal location with zero slip and negligible foot radius. Secondly, the torso was assumed as a point mass, fixed at the location of the hip joint. The proposed assumptions were regarded as acceptable as the analytical model only captured the relevant robot characteristics required for the design process.

The analytical MATLAB model used in the actuator analysis similarly followed that used by B. Knox in the design of the bipedal robot [47], KURMET, at The Ohio State University. The model proposed by Knox compared the analysis of a legged robot to that of a slider-crank mechanism [81] as seen in Figure 4.2, commonly

found in most internal combustion vehicles [83]. The vertical constraint of the sliders motion during operation allowed a vertical jump of a legged robot to be analysed kinematically as the power stroke of a slider-crank mechanism, with the primary focus placed on the modelling of the leg during this phase. In the case of a legged robot, the power stroke would be defined as the thrust phase of a jump from the instance of upward motion until take-off during which the actuators input power into the system [81].

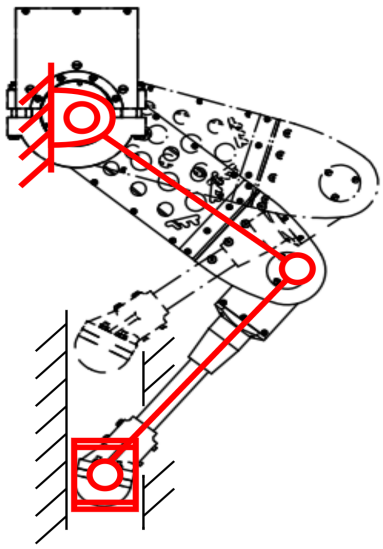

Figure 4.2: An overlay view of a slider crank mechanism on a monopodel robot, illustrating the similarity between the vertically constrained slider motion and the position of the robots foot during a jump.

Performing an incremental static force analysis over the power stroke yielded the ground reaction forces exerted by the foot, providing the leg with vertical motion through the implementation of a force manipulability ellipse. Furthermore, the achieved ground reaction forces were used to determine the total energy transferred into the leg and the corresponding maximum vertical jumping height. In addition to the actuator selection, the analytical model allowed the author to gain a better understanding of the kinematics of the leg morphology. This understanding was achieved by observing the jumping performance of the model while varying the geometry of the links, along with the starting position of the foot over an incremental range of values. An overview of the analytical analysis shown in Figure 4.3 illustrates the flow between the fundamental sub-models, namely the inverse kinematics, system input torque, ground reaction forces and jumping height determination used to characterize the jumping performance of the leg.

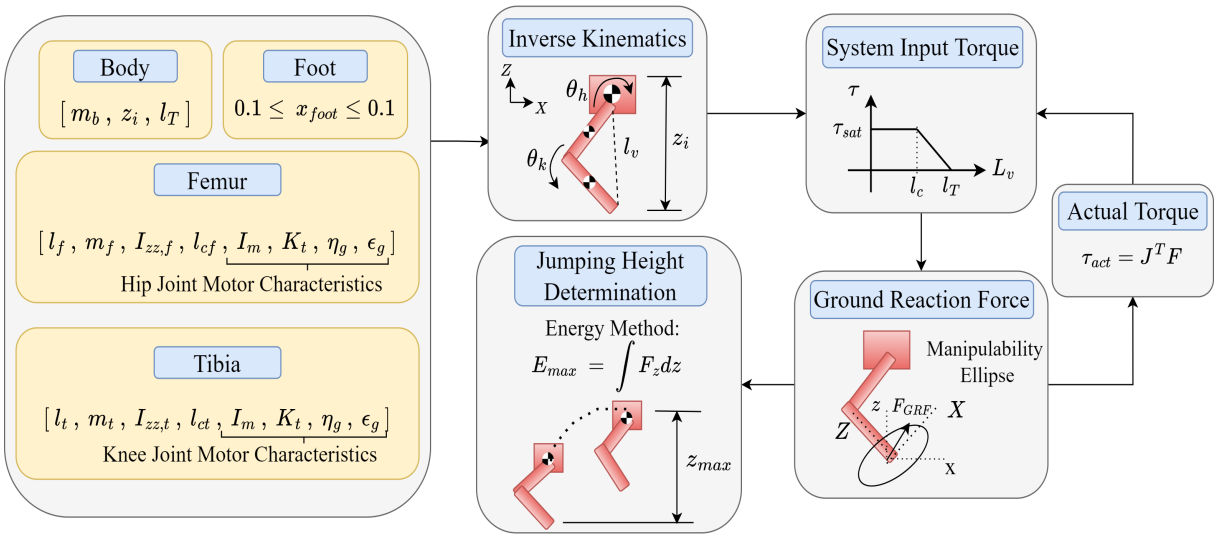

Figure 4.3: An overview of the incremental analytical analysis of a simplified monopedal model performed in MATLAB, illustrating the flow of the design process and identifying the fundamental sub-models utilized in determining the maximum theoretical jumping height of the leg.

4.2.1. Inverse Kinematics

An inverse kinematic model of the robot was developed to analytically compute the position and orientation of the robots joints in the design process of the platform. The inverse kinematic model was based on the kinematics of a slider-crank mechanism as mentioned in Section 4.2, allowing the articulated leg to be incrementally analysed through the power stroke using a simple two position synthesis method [83]. The derivation of the kinematic equations began by creating a vector loop of the slider-crank model, involving the labelled links shown in Figure 4.4. The vector loop equation for the model yields:

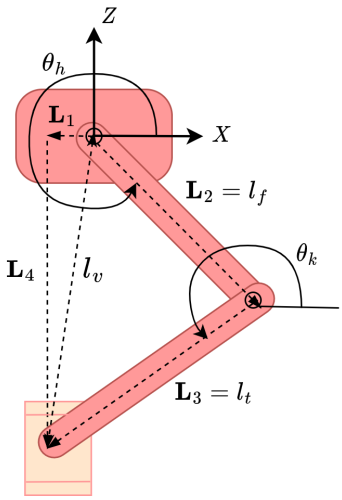

Figure 4.4: Inverse kinematic model diagram accounting for an offset foot position scenario of the slider-crank mechanism.

$$\mathbf{L}_2 + \mathbf{L}_3 = \mathbf{L}_1 + \mathbf{L}_4. \tag{4.1}$$

The magnitude of the vectors denoted by $\mathbf{L}_2$ and $\mathbf{L}_3$ represent the lengths of the femur (l_f) and tibia (l_t) links, respectively and provide the limiting foot position of the leg. Whereas, the vectors $\mathbf{L}_1$ and $\mathbf{L}_4$ represent the respective X and Z coordinates of the foot position and serve as the inputs of the inverse kinematic model. Expanding the vector loop equation into components allowed the model to be characterized in terms of the X-Z coordinate system. The expansion of the vector loop accounted for the hip and knee angles, measured from the horizontal axis and denoted as θ_h and θ_k, respectively. The expanded vector equations yielded the following:

$$X = l_f \cos\theta_h + l_t \cos\theta_k, \tag{4.2}$$

$$Z = l_f \sin\theta_h + l_t \sin\theta_k, \tag{4.3}$$

$$l_v = \sqrt{X^2 + Z^2}. \tag{4.4}$$

Where l_v denotes the virtual leg length of the monopod, representing the minimum distance from the foot position to the hip joint. Combining Equations 4.2 and 4.3 results in a simplified equation which eliminates θ_k through manipulation.

$$A\cos\theta_h - B\sin\theta_h + C = 0. \tag{4.5}$$

Where the variables A, B and C yield:

$$\begin{aligned} A &= -2l_f X, \\ B &= -2l_f Z, \\ C &= X^2 + Z^2 + {l_f}^2 - {l_t}^2. \end{aligned} \tag{4.6}$$

The rearrangement of Equation 4.5 along with the use of trigonometric half identities yielded an equation defining the hip angle of the model. Through further manipulation and substitution an equation for the knee angle was derived.

$$\theta_h = 2\tan^{-1}\left(\frac{-B + \sqrt{B^2 - C^2 + A^2}}{2(C - A)}\right), \tag{4.7}$$

$$\theta_k = \tan^{-1}\left(\frac{Z - l_f \sin\theta_h}{X - l_f \cos\theta_h}\right). \tag{4.8}$$

To perform an incremental force analysis on the leg model through the power stroke of the mechanism, an expression for the Jacobian matrix, denoted by $\boldsymbol{J}_{foot}$, was required. The Jacobian provided a fundamental relationship between the foot and joint velocities, as shown below:

$$\begin{bmatrix} \dot{X} \\ \dot{Z} \end{bmatrix} = \boldsymbol{J}_{foot} \begin{bmatrix} \dot{\theta_h} \\ \dot{\theta_k} \end{bmatrix}, \tag{4.9}$$

$$\boldsymbol{J}_{foot} = \begin{bmatrix} -l_f \sin\theta_h & -l_t \sin\theta_k \\ l_f \cos\theta_h & l_t \cos\theta_k \end{bmatrix}. \tag{4.10}$$

The Jacobian matrix was achieved through differentiating Equations 4.2 and 4.3. Additionally, the Jacobian matrix validated the inverse kinematic comparison between the slider-crank model and an active two DoF monopedial robot as the matrix resulted as function of both hip and knee angle.

4.2.2. System Input Torque

The system input torque addresses the method used to analyse the input torques produced by the motors actuating the hip and knee joints of the leg during the power stroke of a jump. The analytical model determined the input torque through the use of a saturated motor torque model in combination with a torque-leg length curve [81] in an attempt to increase the accuracy of the motor model dynamics. Additionally, a gravitational torque penalty was implemented to compensate for the effects of the link masses on the motor inputs.

Motor Torque Model

The saturated motor torque model assumed that the available torque at each joint of the leg remained constant throughout the power stroke of a jump, limited by the characteristics of the respective motors. The saturated motor torque was defined by:

$$\tau_{sat} = I_m K_t \eta_g \varepsilon_g. \tag{4.11}$$

Where, I_m and K_t respectively denote the maximum operational current and torque constant of the motor. The variables η_g and ε_g relate to the gearbox characteristics of the motors, with η_g denoting the reduction ratio and ε_g representing the efficiency of the gearbox. The incremental analytical analysis utilized a torque-leg length model generated by Knox [81] to implement a generic curve that created a simple relationship between the virtual leg length, l_v, and the motor torque. The incorporation of the torque-leg length model resulted after Knox concluded the assumption of constant torque throughout the power stroke was deemed unrepresentative of a physical system, due to the increase in rotational joint velocities [81]. The relationship was implemented in the form of a piecewise linear function, allowing the motor torque to be saturated for a percentage of the virtual leg length until a cutoff length, l_c, was reached. Thereafter, the motor torque linearly decreased to zero until the take-off leg length, l_T, was reached and contact with the ground

was broken. The equation defining the virtual cutoff leg length, l_c, and the piecewise linear function, τ_{max}, are shown below in Equations 4.12 and 4.13, respectively.

$$l_c = \eta_c(l_T - z_i) + z_i, \tag{4.12}$$

$$\tau_{max} = \begin{cases} \tau_{sat} & z_i \leq l_v \leq l_c, \\ \frac{\tau_{sat}}{l_T - l_c}(l_T - l_v) & l_c < l_v \leq l_T. \end{cases} \tag{4.13}$$

The variables z_i and η_c represent the initial leg height of the robot and the torque saturation limit, respectively specified by the author for each jumping scenario to achieve optimal performance.

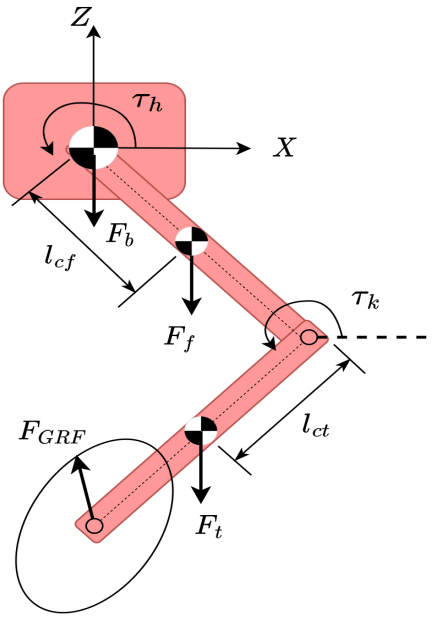

Figure 4.5: Free body diagram of the articulated monopod model, illustrating the forces located at the CoM of the body, femur, tibia and foot of the robot.

Gravitational Compensation

The implementation of the gravitational torque penalty compensated for the energy required to move the masses of each leg link through the power stroke, as the effects of gravity opposed the systems input torque during a performed jumping maneuver. The gravitational torque penalty may also be viewed as the torque required by each joint to keep the leg links statically stable throughout the power stroke. The actual torque, $\boldsymbol{\tau}_{act}$, subjected to the system, with $\boldsymbol{\tau}_g$ denoting the gravitational penalty, was hence defined as:

$$\boldsymbol{\tau}_{act} = \tau_{max} - \boldsymbol{\tau}_g, \tag{4.14}$$

$$\begin{bmatrix} \tau_{g,h} \\ \tau_{g,k} \end{bmatrix} = \begin{bmatrix} m_f l_{cf} \cos\theta_h + m_t(l_f \cos\theta_h + l_{ct} \cos\theta_k) \\ m_t l_{ct} \cos\theta_k \end{bmatrix} g. \tag{4.15}$$

The gravitational torque penalty was derived using the gravitational forces depicted in the free body diagram shown in Figure 4.5. The forces are located at the CoM of each leg link, with l_{cf} and l_{ct} representing the CoM lengths of the femur and tibia links, respectively. Similarly, the masses of the femur and tibia links are denoted by m_f and m_t, respectively.

4.2.3. Ground Reaction Forces

The ground reaction forces of the modelled leg were determined through a concept known as a manipulability ellipse, which described the velocity capability of an end-effector with respect to the motion limitations of the actuators [84]. The concept of a manipulabilty ellipse or manipulating force ellipse was developed with the purpose of determining the best position of a robotic end-effector in the workspace [85] as a function of joint configuration [86]. Therefore, indicating the kinematic dexterity of the robotic manipulator in numerous directions.

$$\boldsymbol{\tau} = \boldsymbol{J}_{foot}^{T}\mathbf{F}. \tag{4.16}$$

The Jacobian matrix of the end-effector determined in Equation 4.10 was used to create a relationship between the joint torques and ground reaction forces shown in Equation 4.16. This allowed the manipulating force ellipse to be used in determining the optimal forces and torques for the foot of the leg at a given configuration. In the case of the two-joint articulated leg model, the various possible foot forces were determined by satisfying the requirement that the norm of the joint torques be less than or equal to one. In comparison to alternative methods of determining ground reaction forces, the manipulabilty ellipse may not have produced the highest analytical jumping height. However, this method minimized joint torques [87], which increased the efficiency of the leg and provided sufficient motivation to pursue the method.

It is important to note that that ground reaction force determined using the manipulating force ellipse during the design phase of the leg was not the force experienced by the robot when landing on the ground. The force achieved from the developed joint torque profiles represented the force applied by the foot of the robot onto the ground during the power stroke of a jump to achieve flight. To ensure the maximum vertical thrusting force of the leg was produced during the power stroke, the joint torques were determined using the largest vertical component of the ground reaction force. The manipulating force ellipse was determined using the normalized Jacobian of the maximum allowable joint torques to ensure no joint exceeds the torque limitations of its motor. The normalized Jacobian,

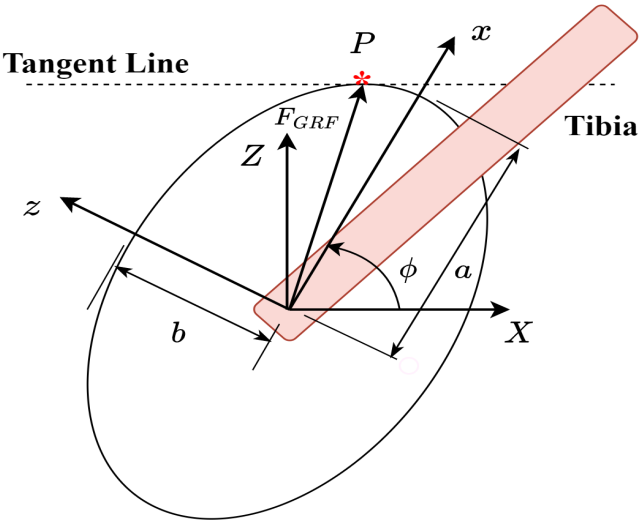

Figure 4.6: Concept of the Manipulating Force Ellipse. Note the orientation of the principle x-z coordinate frame, located at angle (ϕ) from the global X-axis to accommodate the tangential connection between the horizontal line and the ellipse.

$\boldsymbol{J}_{\hat{foot}}$, was defined as follows:

$$\boldsymbol{J}_{\hat{foot}} = \left[\begin{bmatrix} \tau_h^{-1} & 0 \\ 0 & \tau_k^{-1} \end{bmatrix} \boldsymbol{J}_{foot}^{T} \right]^{T}. \tag{4.17}$$

The torques τ_h and τ_k represent either the actual or saturation torque of the joint depending on the motor model as detailed in Section 4.2.2. The manipulating force ellipse follows the conventional ellipse equation and utilizes the eigenvalues of matrix $\boldsymbol{J}_{foot}^{\hat{T}}\boldsymbol{J}_{\hat{foot}}$ to relate the principal axes of the ellipse, with the eigenvectors of the matrix determining the direction of the principal axes. The manipulating force ellipse was defined as follows:

$$\begin{aligned} 1 &= \frac{x^2}{a^2} + \frac{z^2}{b^2}, \\ a &= \sqrt{\boldsymbol{E}_{11}}, \\ b &= \sqrt{\boldsymbol{E}_{22}}. \end{aligned} \tag{4.18}$$

Where $\boldsymbol{E}$ represent a two by two matrix of the eigenvalues of matrix $\boldsymbol{J}_{foot}^{\hat{T}}\boldsymbol{J}_{\hat{foot}}$, which relate to the principal axes half length variables a and b. The largest vertical component of the ground reaction force corresponds to a force vector, denoted by $\boldsymbol{F}_{GRF}$, in Figure 4.6, from the centre of the ellipse to a point P on the ellipse which formed a horizontal tangential line. The horizontal tangential line on the ellipse caused the ellipse to be orientated at an angle ϕ from the X-axis. The orientation angle was determined with respect to the global X-Z coordinate frame using the eigenvectors of matrix $\boldsymbol{J}_{foot}^{\hat{T}}\boldsymbol{J}_{\hat{foot}}$.

The orientation angle ϕ was determined as follows:

$$\tan\phi = \frac{\boldsymbol{V}_{21}}{\boldsymbol{V}_{11}}. \tag{4.19}$$

Where $\boldsymbol{V}$ represents a two by two matrix of the eigenvectors. The coordinates of point, P, on the ellipse were required to be translated to the principal x-z coordinate frame to align its coordinate frame with the specified manipulating force ellipse coordinate frame. The coordinates of the tangential point, P, were determined through equating the the slope of a line at an angle $-\phi$ for the principal x-axis to the derivative of the general ellipse equation. The components of the P coordinate in the principal x-z coordinate frame were determined as follows:

$$\begin{aligned} \frac{dx}{dz} &= \frac{-b^2 P_x}{a^2 P_z} = \tan(-\phi), \\ P_x &= \frac{a^2 \tan\phi}{\sqrt{a^2\tan\phi + b^2}}, \\ P_z &= \frac{b^2}{\sqrt{a^2\tan\phi + b^2}}. \end{aligned} \tag{4.20}$$

The ground reaction forces subjected to the robot for maximum jumping height analysis were obtained by transposing the principal coordinates of the point, P, into the global X-Z coordinate frame. The transposed, P, coordinate and ground reaction force matrices result to the following:

$$\begin{bmatrix} P_X \\ P_Z \end{bmatrix} = \begin{bmatrix} \cos\phi & -\sin\phi \\ \sin\phi & \cos\phi \end{bmatrix} \begin{bmatrix} P_x \\ P_z \end{bmatrix} + \begin{bmatrix} X \\ Z \end{bmatrix}, \tag{4.21}$$

$$\begin{bmatrix} F_X \\ F_Z \end{bmatrix} = \begin{bmatrix} P_X - X \\ P_Z - Z \end{bmatrix}. \tag{4.22}$$

Where, F_X and F_Z, denote the respective X and Z components of the ground reaction force. The actual motor joint torques required to produce the desired ground reaction forces were then back calculated through the Jacobian matrix and subjected to the gravitational torque penalty.

4.2.4. Jumping Height Determination

The maximum theoretical jumping height determination was a crucial sub-model of the analytical analysis as it produced the results required to evaluate actuator performance and analyse different link lengths for the design of the leg. The incremental nature of the analytical analysis allowed the maximum jumping height to be determined by iterating through a single power stroke cycle of the monopedal leg, over a range of foot positions at a defined constant starting height. This identified the need for a parameter to quantify

the end of the power stroke of the leg. Which in essence referred to the take-off instance of the robot, at which foot contact with the ground was broken and the energy input to the leg was concluded. The incorporation of a take-off instance aided in improving the reliability of the model by making it more representative of a physical system. The accuracy of the quantified take-off instance of the robot was a pivotal aspect of analysis, as a shortened power stroke would result in a reduction of energy input to the system and an underestimated theoretical jumping height. Similarly, an extended power stroke would result in a surplus of energy input to the system and an overestimated jumping height, which would evidently deem the predicted jumping height of the model unrepresentative of a physical platform.

An energy approach was implemented in determining the maximum theoretical jumping height of the model, allowing the robotic leg to be described in terms of energy transformations. The accuracy of the take-off instance could be maintained with this approach by characterizing take-off as the point at which maximum kinetic energy occurred on the leg. Similarly, the maximum jumping height of the model was characterized as the point at which the kinetic energy of the leg converted to potential energy. The implemented energy approach utilized the vertical ground reaction force, F_z, in determining the maximum jumping height of the robot as it assumed that the vertical ground reaction force acting over the jumping height, z, contributed all the energy required by the system to create vertical motion. The maximum kinetic energy of the leg denoted by E_{max} was determined as follows using trapezoidal numerical integration:

$$E_{max} = \int F_z \, dz. \tag{4.23}$$

A gravitational penalty was applied to the determined maximum kinetic energy to account for the effect of the monopod's body moving upward through a gravitational field. The available kinetic energy produced by the leg for vertical motion resulted to the following:

$$E_{act} = E_{max} - m_b g(L_T - z_i), \tag{4.24}$$

$$z_{max} = \frac{E_{act}}{(m_b + m_t + m_f)g} + z_i. \tag{4.25}$$

Using the actual available kinetic energy, E_{act}, shown above in Equation 4.24, the resultant height of the robot produced at the point of complete energy transformation was obtained. The estimated take-off leg length, L_T, in combination with the resultant energy transformation height was used to determine the maximum theoretical jumping height of the robot, denoted by z_{max}, shown above in Equation 4.25.

4.3. Actuator Analysis

Actuator analysis and selection for legged robots, as with any robotic system, is a pivotal aspect which requires a considerable amount of time due to the unique challenges introduced to the design process by legged locomotion. High speed, accurate actuation of the hip and knee joints are essential for transient locomotion as the actuators alternate between periods of high speed swing in flight and high force delivery in stance [26]. In addition, the actuators are required to withstand shock loads caused by high impacts generated when the robot makes and breaks contact with the ground at various angles in transition [12, 26, 35]. The under or over design in actuator selection directly affects the transmission objectives and system specifications outlined in Section 3.1, which influence the dynamic nature and maneuverability of the robot.

Using the MATLAB incremental analytical analysis described throughout Section 4.2, different actuators could be analysed and assessed through the jumping performance of the model. Acknowledging the design specifications outlined in Section 4.1, a conventional equal link length for the femur and tibia segments of the leg were analysed within the specified range. A range of foot placement positions were explored to examine the robot's jumping height at different foot placement configurations, due to the inability of a physical robot to make contact with the ground at an ideal location. Similarly, due to the uncertainty of the exact take-off length of the robot, an estimation of the length was assumed by the author over an incremental range of values from 75% to 90% of the robot's maximum vertical length, l_{max}.

Table 4.1 shows the detailed design parameters used throughout the actuator analysis to obtain a better understanding of the robot's jumping performance. For simplicity purposes, a constant design mass and inertia of the robot was estimated throughout the actuator analysis based off initial design concepts and the prototyping parameters of existing platforms [8, 47].

Table 4.1: Design Parameter Details.

Parameter	Value	Units
l_{cf}	$0.5l_f$	m
l_{ct}	$0.5l_t$	m
l_{Link}	$0.2 \leftrightarrow 0.35$	m
x_{foot}	$-0.1 \leftrightarrow 0.1$	m
l_T	$0.75l_{max} \leftrightarrow 0.9l_{max}$	m
m_b	1.775	kg
m_f	1.75	kg
m_t	0.675	kg
$I_{zz,f}$	0.015	kg.m^2
$I_{zz,t}$	0.0015	kg.m^2
ε_g	0.8	%
η_c	0.95	%

4.3.1. Torque Actuator Comparison

Using the knowledge gathered from the numerous actuators studied in Section 2.3 of the Literature Review and the actuator transmission objectives noted in Section 3.1, a process of elimination could commence to determine the optimal torque actuator for the series articulated configuration. The elimination process was aided by a comparison of the available actuator strategies evaluated against each of the transmission objectives shown in Figure 4.7. The downfalls noted for the various torque actuators are as follows:

1. Geared motors (GM) perform poorly throughout all aspects of the transmission objectives. The augmentation of a motor and gearbox allows the torque density of the actuator to increase by orders of magnitude while adding control complexities, increased reflected inertia and reduced mechanical robustness [3, 50]. Non-linearities associated with backlash, internal stress and friction created within the gear train [3] contribute to the increased complexities in modeling these actuators, effectively reducing their desirability for use in legged locomotion.

2. Direct Drive (DD) actuators produce ideal performance throughout majority of the transmission objectives and are still used in legged robots despite their lack of crucial torque density. DD actuators suffer from high energy losses due to operating at high speeds and low torques, creating the problem of poor heat dissipation for the actuator [8, 12]. With the uncertainty surrounding the peak torque required to

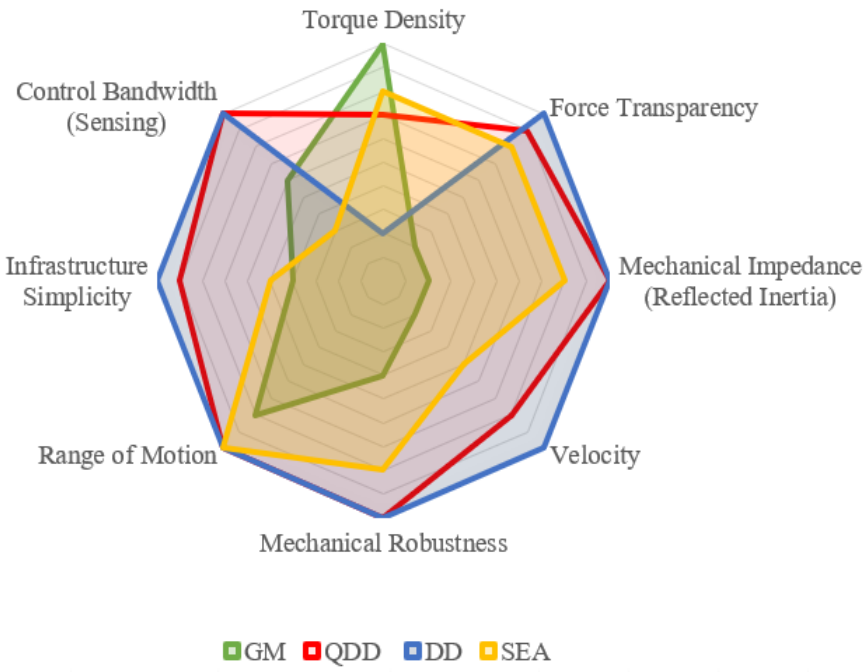

Figure 4.7: Comparison of the torque actuation strategies with respect to the various transmission objectives. An optimal actuation strategy could be identified by comparing the enclosed area's of the web per actuator as better performance for the transmission objectives are defined by the outer layers of the web. Evidently, DD and QDD actuators offer the best overall performance maintaining a good balance between the various objectives. Image adapted from [3, 8].

perform transient maneuvers, DD actuators posed a risk to the robot's design due to their limited torque.

3. The stiffness of Series Elastic Actuators (SEA) is designed around the desired motion of the robot, which is difficult to achieve due to the minimal research concerning transient maneuvers in legged robotics [8]. SEA's are typically required to compromise performance in control bandwidth to improve compliance. Resulting in an increase in the complexity of the system and critical system parameter such as the dimension and mass [79], essentially limiting the practical benefits in legged robots.

The ideal versatile actuator for dynamic legged locomotion which balances the trade-offs between torque density and high speed, while producing high control bandwidth and offering low reflected inertia was selected in this thesis to be the Quasi-Direct Drive (QDD) actuator. In addition, the high control bandwidth offered by QDD actuators permits the use of virtual compliance. The CubeMars AK-series range of BLDC motors was selected for analysis in the design process with the three available actuator options shown in Figure 4.8.

(a) AK80-6. Image from [88]. **(b)** AK80-9. Image from [89]. **(c)** AK70-10. Image from [90].

Figure 4.8: Comparison of the three highly integrated CubeMars BLDC torque modules selected for analysis.

CubeMars BLDC Torque Module

The CubeMars AK-series is a specialised range of compact quasi-direct drive BLDC modules, selected based on the internal motor controller, internal gearbox and internal encoder; which simplify several aspects involved in coupling actuator transmissions. The compact nature of the CubeMars QDD dynamic modules allow the motors to be used in a direct drive fashion as they mitigate the need for external gear reducers. Additional motivation for the selection of the CubeMars AK-series modules include the following features:

- Built-in planetary gear reduction.
- Embedded controller utilising Field Oriented Control (FOC) and the CAN communication protocol.
- Single loop absolute 12-Bit encoder.
- High precision control with 0.1° accuracy.
- Backlash of 0.2° (12 arcmin).

The built-in controller utilizes the MIT open source software developed for the low cost actuators used in the fabrication of the MIT mini cheetah robot [32]. The MIT open source software along with the flexible controller scheme allows the module to operate as a positional controller, velocity controller or torque controller based on the desired operational control mode. The detailed specifications of the three analysed CubeMars modules are provided in Table 4.2.

Table 4.2: Motor specification comparison between the different CubeMars AK-series BLDC torque modules analysed for the robot. Note the increase in stall torque of the modules proportional to the increase in gearbox reduction.

Motor Specifications	Units	BLDC Motor Model		
		CubeMars AK80-6	CubeMars AK80-9	CubeMars AK70-10
Mass	g	485	485	521
Peak Current	A	24	24	26.1
Gear Reduction	-	6:1	9:1	10:1
K_t	N.m/A	0.091	0.091	0.095
Angular Velocity	rpm	365	245	400
Stall Torque	N.m	12	18	24.8
Torque Density	N.m/kg	24	37	47.6
Number of Pole Pairs	-	21	21	21
Resistance Phase to Phase	mΩ	170±5	170±5	272±5
Inductance Phase to Phase	μH	57±10	57±10	113±10
Module Diameter	mm	98	98	89
Module Width	mm	38.5	38.5	50.2

Table 4.3: Different motor configuration scenarios used in the jumping height analysis to characterize the actuators capabilities and assist in validating the appropriate configuration selection.

Configuration	Hip Joint	Knee Joint
1	AK80-6	AK80-6
2	AK80-9	AK80-9
3	AK70-10	AK70-10
4	AK80-9	AK80-6

Actuator Scenarios

The jumping height analysis was examined for all possible motor configurations involving the three CubeMars modules considered for this design. However, this thesis addresses the four most feasible actuator configuration scenarios as illustrated in Table 4.3. The first three configurations utilized the same actuator for the hip and knee joints, ensuring equal mass distribution at the location of the hip joint. Upon analysis it was noted that the knee joint required less torque in comparison to the hip joint to initiate a jumping

maneuver. This motivated the addition of a fourth configuration utilising two motors of the same mass with different gear reductions to explore the possibility of achieving increased performance at a lower cost.

4.3.2. Geometry Realisation

Quantifying an ideal platform size requires balance between geometric specifications and actuator performance, as the size of the robot is limited within the capabilities of the actuator. In addition to the jumping performance of the robot in this thesis, the following external limiting factors attributed to the sizing determination:

1. Available experiment space.
2. Safety.
3. Fabrication and assembly.
4. Number of people required to operate the platform.

The current infrastructure of the ESL does not allow the laboratory to accommodate large robots due to the lack of large open areas required for executing desired maneuvers. In terms of safety, robots with increased geometric specifications require more caution during operation as the platform's potential to seriously injury an individual increases proportionally with size. The operation of the robot should be limited to a maximum of two people to avoid congestion and reduce safety risks. Despite the negative factors concerning large robots, a trade-off is introduced through fabrication and assembly as the robot should be large enough to reduce the complexity and cost of manufacturing and ease assembly. Based on the above mentioned influential factors, the author regarded the exploration of link lengths greater than 0.35 m impractical and unrealistic to operate safely given the environmental conditions of the laboratory.

Analysing the jumping performance of the specified range of link lengths shown in Figure 4.9, a visible relationship emerged between the link length of the robot and the jumping performance. The jumping height of the robot increases linearly with an increase in link length. However, the jumping height performance produced by the actuator configurations degrades with respect to the maximum vertical length of the robot, indicating that shorter, compact links produce optimal performance. To maintain sufficient jumping height performance and satisfy the external influential sizing factors of this thesis, the length of the femur and tibia segments of the leg were selected to be 0.27 m.

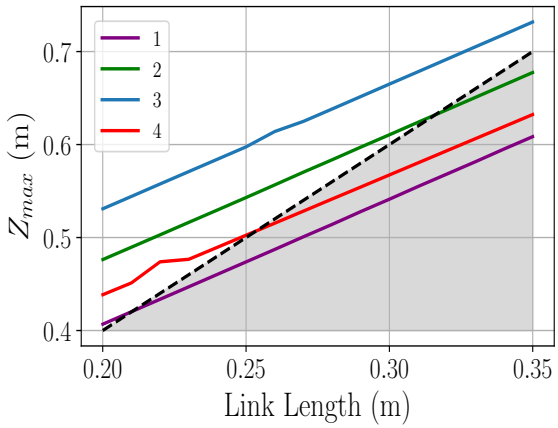

Figure 4.9: The maximum jumping height performance of the robot with respect to link length for the stated actuator configurations shown in Table 4.3 using an initial starting height of $0.5l_{max}$ and fixed takeoff leg length of $0.8l_{max}$. The maximum vertical length of the robot, l_{max}, is indicated by the black dashed line with the shaded area below the line representing undesirable jumping performance.

4.3.3. Jumping Height Realisation

Due to the assumptious nature of design, the jumping height determination was analysed over a range of values as mentioned and shown in Table 4.1. The following factors were explored with the aim of identifying performance trends amongst the selected motor configurations, due to their direct influence in characterizing the jumping performance of the robot in the analytical analysis:

- Effect of different take-off lengths.
- Effect of the initial foot position.

With the results of the analysis shown in Figure 4.10, it is interesting to note how a 15% difference in take-off length impacts the jumping performance of the robot. The jumping height of each configuration increases linearly with an increase in take-off length, however, motor configurations with higher torque density experience greater change in jumping height.

Considering the jumping height performance of the analytical model, the CubeMars AK70-10 module was selected for use in this thesis. Despite the slight increase in module weight, the AK70-10 module produced the best performance in all aspects of analysis as a result of the modules higher torque density. Additionally, due to the unknown torques required to produce transient maneuvers, the AK70-10 module proved to be the safest option as the jumping height analysis results displayed heights greater than the robot's maximum vertical length of 0.54 m. Indicating, the actuator's capability to propel the robot off the ground.

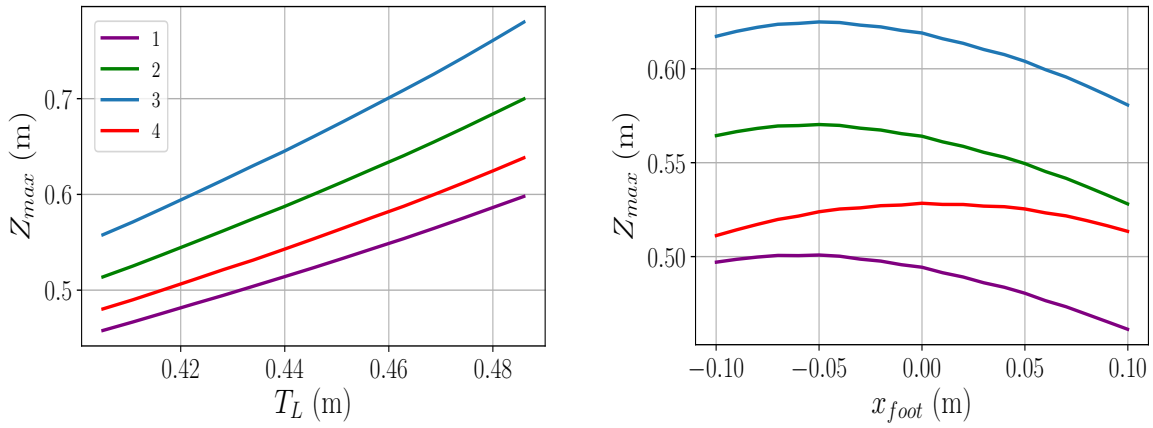

Figure 4.10: The analytical jumping height of the robot with respect to take-off length (left) and initial foot position (right) for the motor configurations shown in Table 4.3. The initial foot position plot was analyzed at a take-off length of $0.8l_{max}$ and displayed observable trends. Configurations utilizing the same motor at both joints experienced reduced jumping heights as the initial foot position was placed underneath the body. Whereas, motor configuration 4, which utilizes two different motors, exhibited more consistent jumping performance over various initial foot positions.

4.4. Summary

This chapter presented the design requirements and specifications used to embody the design process of the bipedal robot through conducting an incremental analytical analysis of the system prior to the structural design. The analytical analysis detailed throughout this chapter, focused on the modelling of the robot's kinematics, torques and ground reaction forces for a monopedal scenario due to the symmetry introduced about the sagittal plane of a biped. Thereafter, a torque actuator evaluation was conducted and resulted in the analysis of three CubeMars BLDC modules. Finally, the analytical analysis assessed the jumping performance produced by the three actuators for various actuator configurations and leg lengths; resulting in the selection of the CubeMars AK70-10 module for the robot design.

Chapter 5

Mechanical Design

The mechanical design of the platform was an extended process which continued throughout the entire duration of this thesis requiring multiple iterations and reviews. The following chapter describes the iterative design process of the mechanical components, detailing the build-up of an initial proof of concept in the form of a monopedal platform followed by an extension to the desired bipedal platform. Emphasis was placed on the design of the femur, tibia and foot of the robot with the aim of minimizing the weight and inertia of the platform while satisfying the necessary strength and stiffness requirements of the links. Fabrication and assembly considerations were accounted for in the design, ensuring the complexity of the parts were within the capabilities of the Stellenbosch University electronic department workshop.

The design decisions taken by the author should not be viewed as the limiting factor for the potential of the platform, but rather as an initial step in creating a dynamic, lightweight and robust robot for future generations within the ESL research group [13] to expand and implement design improvements. Adapting the platform to perform alternative maneuvers and with an increased budget, endless possibilities exist.

5.1. Prototype Development

The design development process of the robot consisted of generating multiple concepts in Inventor with the purpose of examining each of the design trade-offs. The identified trade-offs were used to address focal design aspects and justify the consistency of specific design choices throughout the concept development phase. A brief summary of the initial generated concepts is presented as follows:

First Concept: The femur consisted of a CNC machined split case design utilizing studs to connect and align the two halves of femur correctly. To reduce the weight and inertia of the design, sections of material were removed through triangular cutouts on the upper part of the femur. In addition, the tibia was also designed to be CNC machined in the shape of I-beam creating a light weight, structurally sound limb.

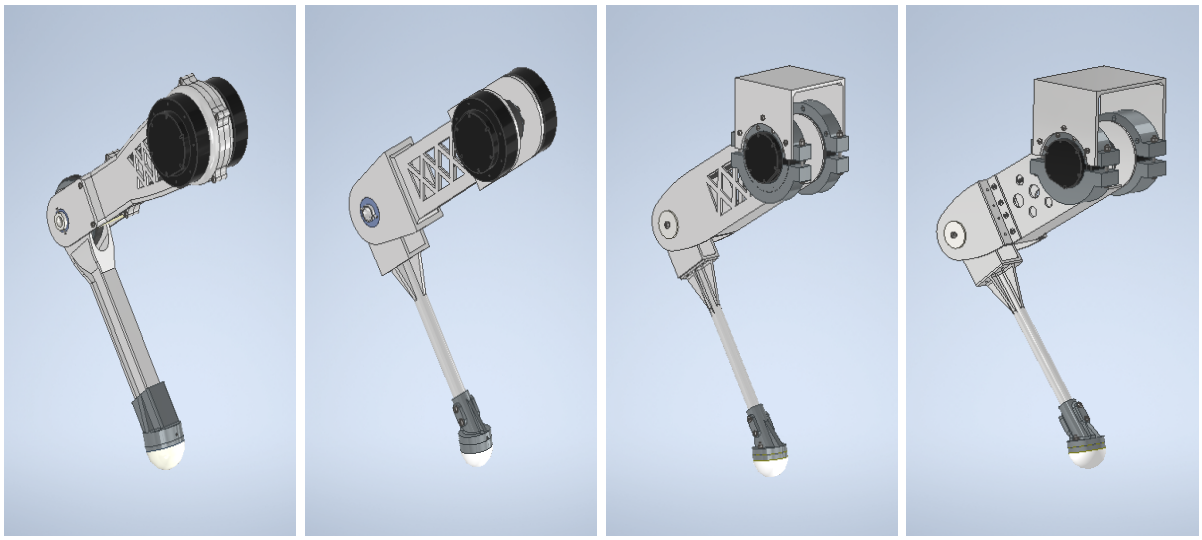

(a) First Concept. **(b)** Second Concept. **(c)** Third Concept. **(d)** Fourth Concept.

Figure 5.1: A comparison of the numerous design concepts generated for the prototyping phase of the platform. The generated concepts present the evolution of the platform design process as the mechanical and manufacturing flaws identified for each concept were used to inspire the design modifications implemented in succeeding iterations.

Second Concept: The femur design consisted of three welded sections fabricated from standard low cost aluminium rectangular tubing. Similarly to the first concept, triangular material cutouts were removed from the femur limb of the robot. The tibia limb of the leg consisted of a section of aluminium round tubing attached to an aluminium yoke and supported by four welded ribs.

Third Concept: The femur limb of the robot utilized a simplistic design fabricated entirely from a single section of low cost aluminium rectangular tubing. Similarly to the previous two concepts, triangular material cutouts were removed from the upper femur of the robot. A torso bracket along with motor brackets were designed to house and support the actuating motors of the robot. The tibia design developed in the second concept was utilized in this design as it was regarded as a structural sound initial concept.

Fourth Concept: This concept presented an improved iteration of the third concept with the only difference being the design of the femur limb. The improved femur design consisted of a section of aluminium rectangular tubing containing circular material cutouts to allow for in house fabrication. The major difference between the two concepts occurred at the knee location of femur. As the improved iteration incorporated aluminium plated brackets to create more assembly room at the knee joint, while reducing the deformation and stress experienced at the knee shaft location.

The focal design aspects governing the generated initial concepts, along with further

actions required to improve the overall manufacturability and design of the robot where categorized as follows:

- Motor placement.
- Manufacturing processes and assembly.
- Foot implementation.

Due to the iterative nature of the concept generation process, the fourth concept shown in Figure 5.1, was selected to form the basis of the preliminary prototype as it addressed majority of the outlined focal aspects required in order to proceed with finer modifications.

Motor Placement

All four initial concepts generated during the design of the series articulated leg utilized a coaxial motor configuration located at the hip of the leg as shown in Figure 5.2. Utilizing a coaxial configuration instead of placing the tibia limb motor at the knee joint, benefits the design of the platform by minimizing the inertia and mechanical impedance added to the femur. After generating the second design concept, a decision was made to detach the knee actuator from the femur and to support it using the torso of the leg, due to a lack of information regard the shaft strength of the AK70-10 module. In addition to reducing the bending stress experienced by the hip actuator shaft, the use of the torso support served as an attempt to further reduce the inertia and mechanical impedance of the femur.

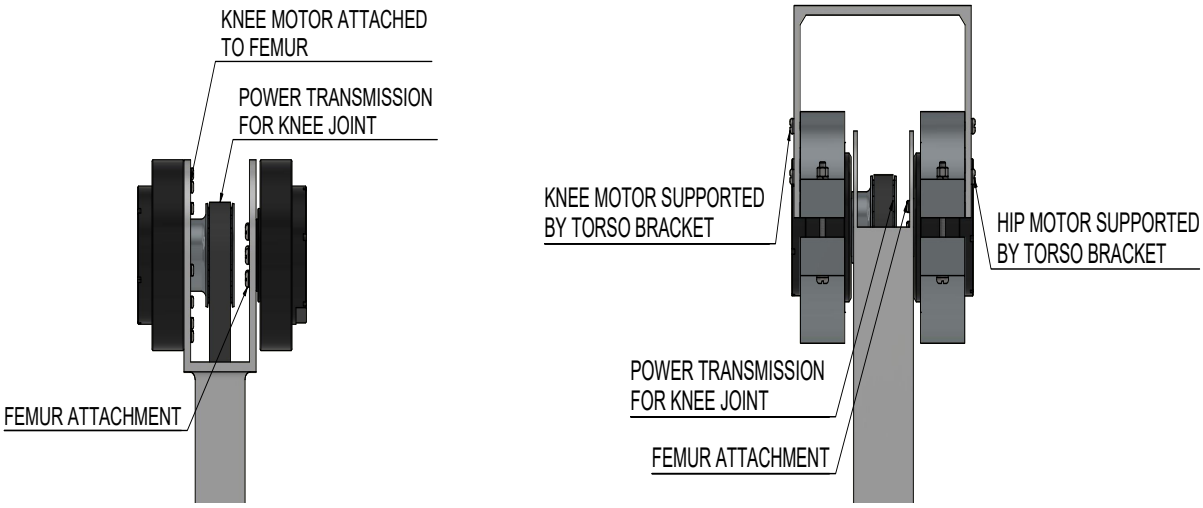

(a) Fixed Knee Motor **(b)** Detached Knee Motor

Figure 5.2: An annotated comparison of the two coaxial motor placement configurations. Take note of the load reduction experienced by the hip motor through the incorporation of a torso bracket.

Manufacturing Processes and Assembly

The manufacturability of the design concepts involved successive discussions and reviews with the workshop foreman to eliminate the use of processes such as CNC machining, due to inadequate equipment for in house manufacturing and to avoid high expenses from outsourced manufacturers. Welding processes were avoided as the process reduces the accuracy of replicating parts requiring fine tolerances and increases the difficulty of replacing parts. The use of 3D printing aided rapid prototyping of smaller components allowing the author to physically assess the feasibility, identify flaws and ensure correct tolerancing before proceeding with manufacturing using costly materials.

Low density material options were assessed in the form of rectangular tubing and aluminium plating for the construction of femur limb of the leg. Aluminium plating offered the ability to vary the wall thickness of parts, inherently increasing the strength of the structure. These two option were evaluated for the intended application through the use of a finite element analysis (FEA), revealing increased deformation occurring in the rectangular tubing due to the narrow wall thickness exhibited in standard tubing; evidently promoting the use of aluminium plating. Additionally, portions of material were removed from the femur link through laser cutting, to reduce the mass and inertia of the femur while maintaining the strength and rigidity of the mechanical structure.

Foot Implementation

Multiple end-effector implementations regarding damped and undamped feet were considered during the prototyping phase of the foot. A decision was made to design a custom molded sole for the foot of the robot using silicone rubber compound. The silicone rubber sole acted as a mechanical damper assisting in shock absorption of impacts experienced during landing or jumping [3, 91], (which have a detrimental effect on the durability and life cycle of mechanical components such as bearings, belt transmissions, gear reducers and sensors [30]) evidently filtering out high frequency impulses from reaching the planetary gear reduction of the AK70-10 motors. The following issues concerning the use of 3D printed parts with silicone rubber compound were addressed during the prototyping phase:

1. The adhesive quality of silicone rubber compound on PLA plastic.
2. The molding capability of general purpose silicone rubber compound.

Figure 5.3 shows the outcome of the initial foot prototype addressing the identified concerning issues. In conclusion, the silicone rubber compound sufficiently adhered to the PLA plastic part, producing a robust sole and confirmed the applicability of the material for the design.

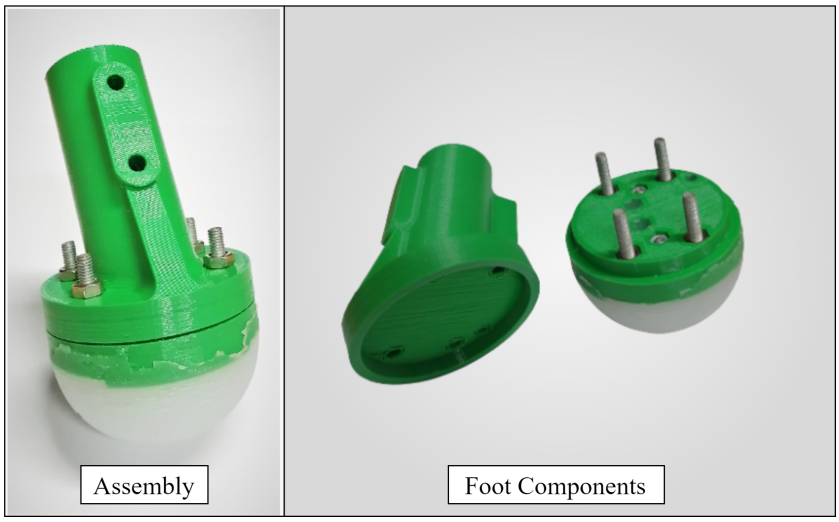

Figure 5.3: An initial 3D printed and molded concept of the foot assembly including the individual components of the foot. Note the uniform circumferential finish of the foot sole acquired during the molding process using silicone rubber compound.

5.2. Monopedal Platform

Upon several iterations of the fourth design concept, the prototype monopodal robot was finalised and fabricated taking into account the manufacturing processes and concerns outlined above in Section 5.1. The initial design concept of the femur and torso bracket were adapted to be manufactured entirely from aluminium plating with additional material removed from the structural components to reduce the mass of the robot. Similarly, the welded support ribs shown in the initial design of the tibia were replaced with a cone design, which easily accommodated the aluminium tube section of the limb. The orthogonal and isometric views of the developed monopedal robot are shown in Figure 5.4.

Table 5.1 details the robot's properties describing the mass, inertia and dimensions of the individual components. While the total mass of the robot including the on board controller electronics resulted to 4.098 kg. Furthermore, the fabricated prototype contained a total range of motion of 120° at the hip joint and 270° at the knee joint without the limbs colliding with the mechanical structure.

During assembly and initial testing it was noted that large deflections occurred on the knee motor side of the torso bracket, due to the large moment created by the weight of motor and a lack of stiffness in the design of the torso bracket. To account for the experienced deflection in the torso bracket, two M8 threaded rods were fitted through the bracket to brace the sides of the torso. Although the addition of the threaded rods eliminated majority of the deflection, deflection continued to occur between the femur and knee motor. Evidently, causing the belt drive transmission to slip over the pulleys

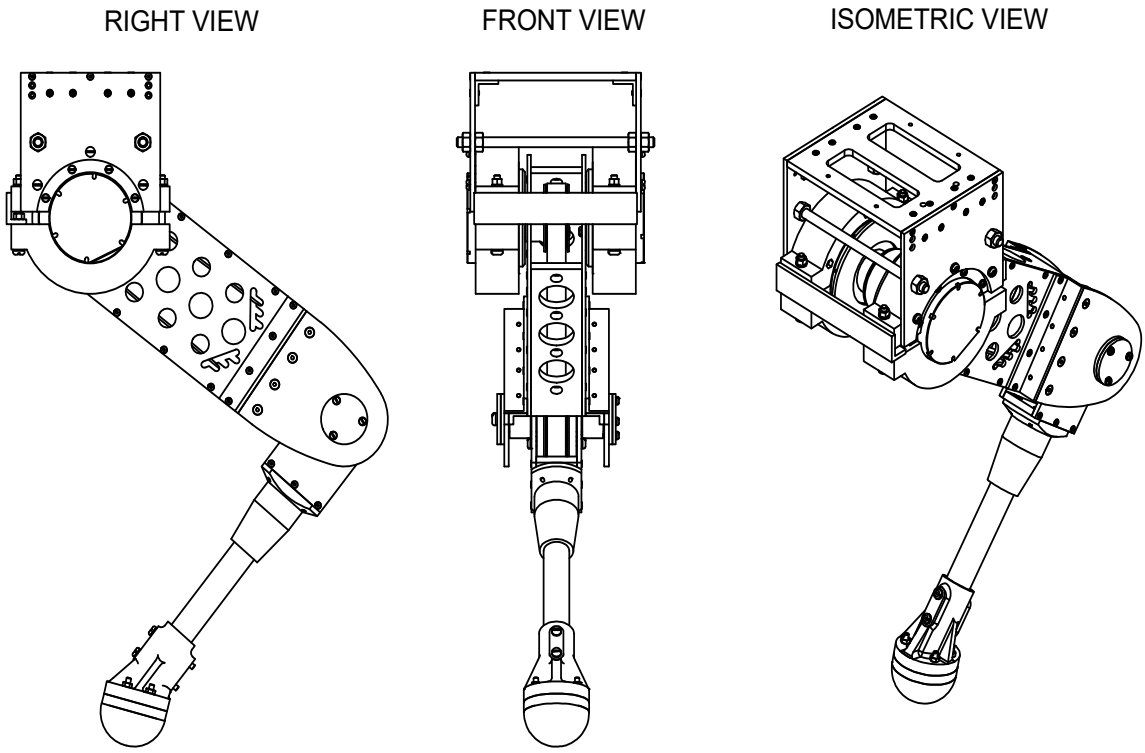

Figure 5.4: Rendered orthogonal and isometric views of the developed monopedial robot.

under high torques. The incorporation of a torso support plate located across the front of the motors, along with acetal bushes fitted between the driver pulley and the femur limb resolved the deformation issues experienced by the robot. Figure 5.5 shows labelled images of the monopodal robot identifying the components incorporated to eliminate the experienced deformation.

Table 5.1: Inventor model properties describing the mass,inertia and dimensions of the monopedal robot.

	Robot Properties			
	Mass (kg)	I_{xx} (kg.m^2)	I_{zz} (kg.m^2)	Dimensions (mm)
Femur	0.995	0.001915	0.009139	270x100x90
Tibia	0.369	0.000145	0.0012224	270x62x∅22
Torso Bracket	0.723	0.001833	0.002065	120x110x144.5
Foot	0.303	0.000336	0.000265	∅56x38

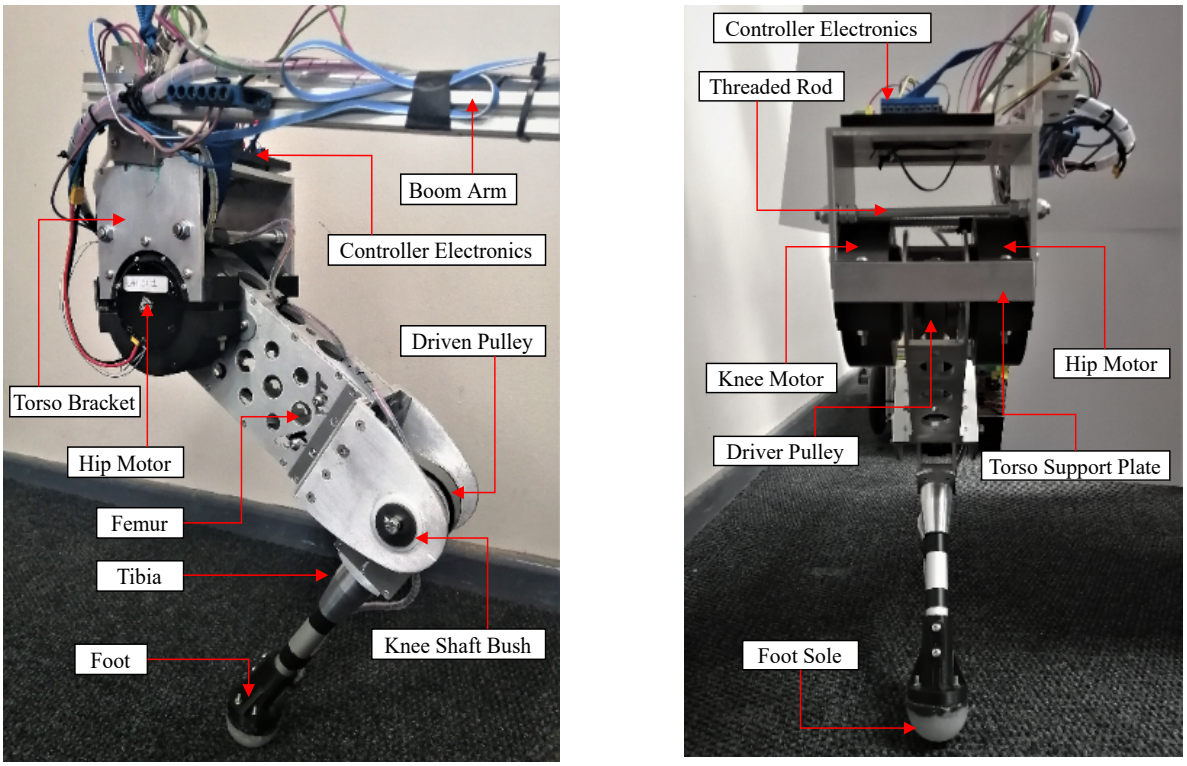

(a) Right View **(b)** Front View

Figure 5.5: Labelled images of the monopedal prototype identifying different parts of the platform.

Power Transmission

A belt drive transmission was selected to actuate the tibia limb of the leg. The belt transmission passed through the hollow structure of the femur connecting the knee joint to its driving motor situated at the hip of the leg as shown in Figure 5.6. Following the belt selection guidelines outlined in [92], the Optibelt 16 mm T10 belt was selected for the power transmission of the tibia. The selected Optibelt belt drive is a polyurethane timing belt fitted with steel tensioning cords capable of withstanding a maximum allowable tension of 1730 N and containing a breaking strength of 8650 N.

In addition, a transmission ratio of 1.25:1 was selected for the system; which increased the torque reduction at the knee joint through the use of a larger driven pulley. To ensure smooth transmission at the knee, a SKF deep groove ball bearing was located within the driven pulley. With a static and dynamic load rating of 5 kN and 9.36 kN respectively, the capabilities of the selected bearing indicated sufficient support required to withstand the impact loads experienced during dynamic maneuvers. The increased torque reduction introduced through the transmission ratio was accounted for through Equations 5.1 and 5.2, to ensure the correct output torque was produced by the knee motor.

$$\tau_{mot}\omega_{mot} = \tau_{out}\omega_{out}. \tag{5.1}$$

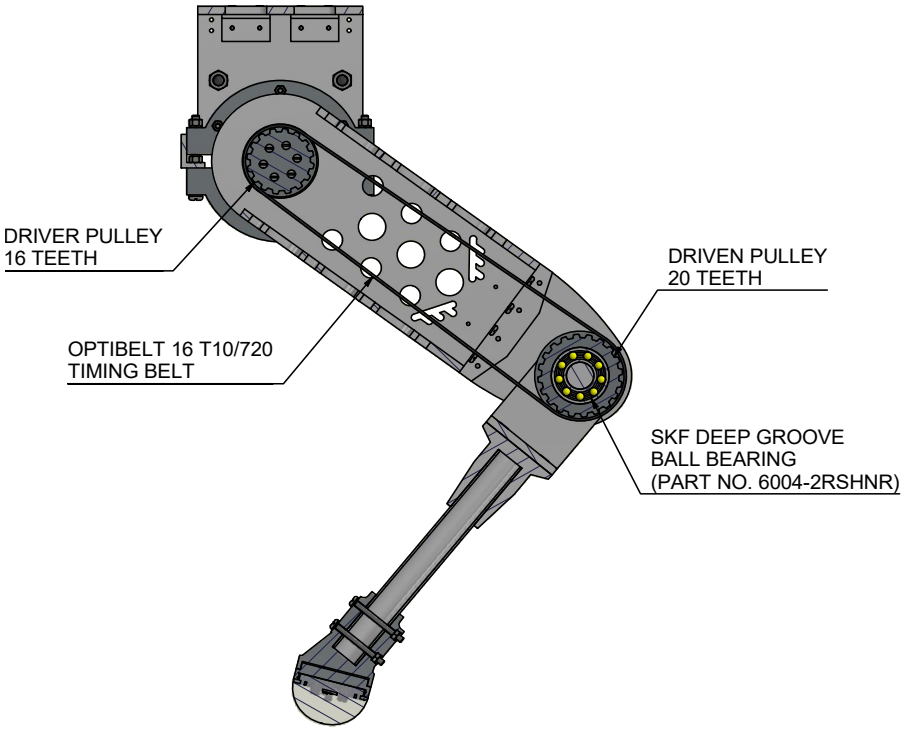

Figure 5.6: Annotated cross sectional view of the monopedal platform detailing the transmission information of the belt drive system.

$$\frac{\tau_{mot}}{\tau_{out}} = \frac{N_{mot}}{N_{out}} = \frac{\omega_{out}}{\omega_{mot}}. \tag{5.2}$$

Where τ, N and ω respectively represent the torque, number of pulley teeth and the angular velocity of the motor and knee output. Upon initial testing it was noted that the influence of the transmission ratio on knee joint angle extended beyond the simple relationship established in Equation 5.2. When the femur was rotated 90°, the tibia was unable maintain its zero position due to transmission ratio despite the driver pulley remaining stationary. Evidently, this observation identified that the true knee angle was a function of both hip and knee motor angles. The true knee angle was defined as follows:

$$\theta_k = \theta_{k,mot}\left(\frac{N_{mot}}{N_{out}}\right) - \theta_{h,mot}\left(1 - \frac{N_{mot}}{N_{out}}\right)\left(\frac{\theta_{h,mot}}{1.48353}\right). \tag{5.3}$$

The increased torque reduction and computing complexity of the knee angle was viewed as a design trade-off, occurring in all power transmission schemes implementing a transmission ratio other than 1:1. Furthermore, the use of a belt drive transmission was considered a design compromise in terms of force control bandwidth. The stiffness and compliance of belt teeth effectively limit the control bandwidth of belt drive transmissions to the resonant frequency of the belt [32]. Therefore, the closed loop torque control of the robot was limited by the resonant frequency of the knee joint. Should the belt drive transmission become the limiting factor in the dynamic performance of the robot, it could

be replaced by a chain transmission which would introduce a higher stiffness. However, chains are considerably expensive in comparison to belts, which motivated their initial omission from the design process.

Strength Analysis

A finite element analysis (FEA) was conducted using Ansys Mechanical [93] simulation software to determine the expected stresses and deformation experienced by the platform during operation. The femur and tibia limbs were regarded as the critical components of the leg and were required to withstand impact forces, while the remaining components were regarded as less critical due their ability to be rapidly reproduced. The simulated forces, torques and bending moments applied to the structures were obtained using the incremental analytical analysis. Additionally, the FEA assisted in determining an appropriate grade of aluminium alloy to ensure sufficient structural strength and allowed the author to maximize component weight reduction without compromising the structural integrity. The structural integrity of the analysed components were quantified through the use of a factor of safety (FoS) defined as follows:

$$FoS = \frac{\sigma_y}{\sigma_{eq}} \tag{5.4}$$

Where the factor of safety represents the ratio of the maximum allowable stress denoted by the yield strength of the material, σ_y, to the equivalent von-Mises stress, σ_{eq}, experienced during a working load. Ratios of greater than 1 were required to achieve an acceptable design, as ratios less than 1 indicate structural failure due to yielding. A desired FoS of 2 was selected for the structural evaluation of the components to ensure the robustness of the platform during impacts loads.

5.2.1. Femur Design

Since mass reduction formed a critical objective in ensuring a lightweight robot structure was produced. A comparison, shown in Table 5.2, was performed to analyse the impact created by the material cut-outs on the mass and inertia of the femur limb. Evidently, the incorporation of the material cut-outs enabled a mass reduction of 120 g resulting in a $\pm 12\%$ difference with respect to an uncut structure. The wall thickness of the femur limb varied throughout the structure as 3 mm, 4 mm and 6 mm aluminium plating was used to enhance the strength around the knee shaft location as shown in Figure 5.7. In addition to reinforcing the femur structure, the use of various wall thicknesses aided the manufacturing and assembly processes by ensuring machine screw could be located adequately. Further details and information regarding the femur limb components can be found in Appendix B.

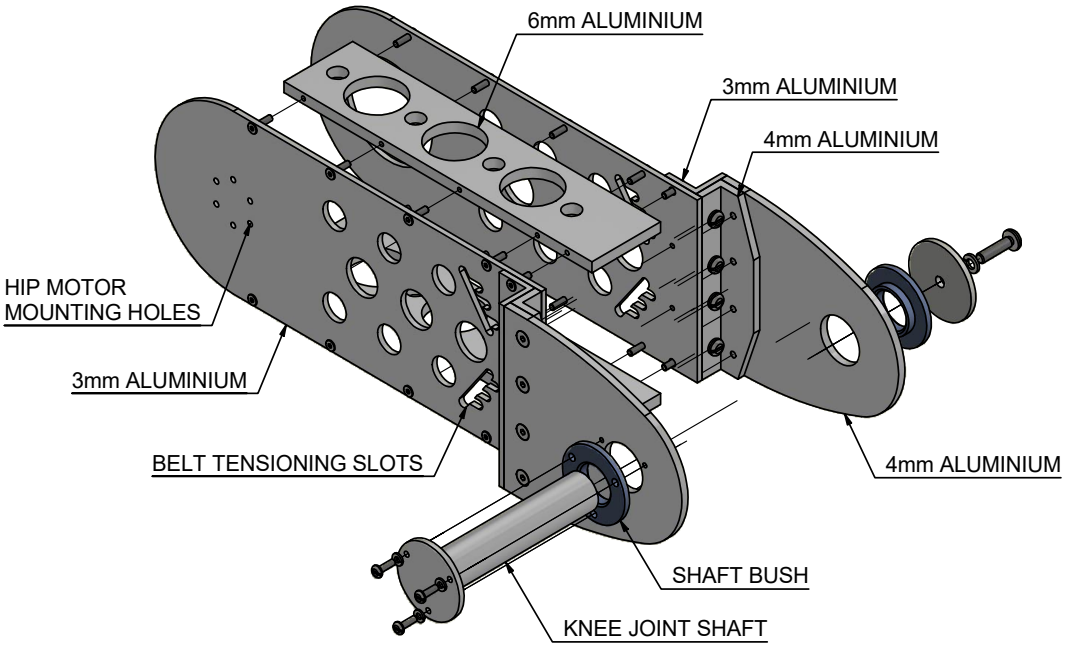

Figure 5.7: An annotated exploded view of the femur assembly.

Table 5.2: Impact of the cut-out material portions on the structural properties of the femur limb.

	Cut-out	Uncut	Difference (%)
Mass (kg)	0.883	1.003	11.96
I_{xx} (kg.m^2)	0.001776	0.001994	10.93
I_{zz} (kg.m^2)	0.007324	0.007764	5.67

The FEA analysis consisted of simulating the structure at the most critical loading period occurring during a jumping or landing maneuver. During the analysis, the mounting holes of hip motor were constrained with cylindrical supports while moments equivalent to the stall torque of the motors (24.8 N.m) were applied to the hip axis and knee joint shaft. In addition, a resultant force of 89.44 N obtained from the incremental analytical analysis was applied at the centre of the knee joint shaft to represent the force generated by the tibia on the shaft during a jumping maneuver. The analysis of the von-Mises stress and deformation results shown in Figure 5.8, showed the maximum stress indicated by the red tag on the image occurring on a bolt at the knee shaft. While the minimum stress occurred on the top of the structure indicated by the blue tag. Similarly, the maximum and minimum deformation were represented by the red and blue tags, respectively with the maximum occurring at the end of the knee shaft and the minimum at the location of the hip axis.

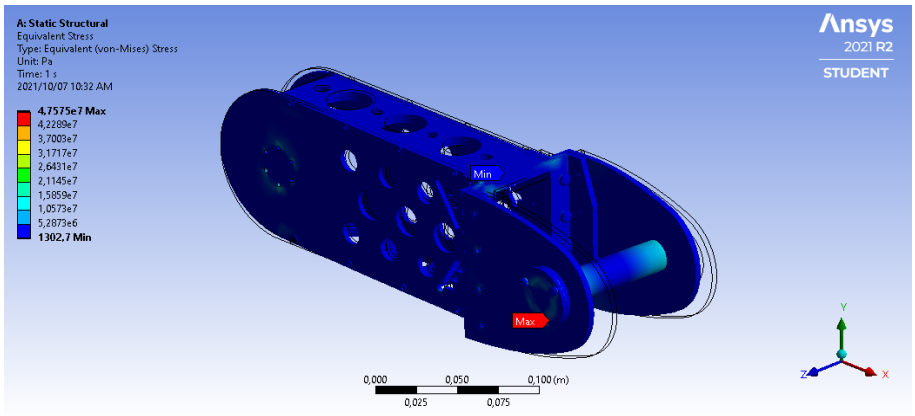

(a) von-Mises Stress Analysis

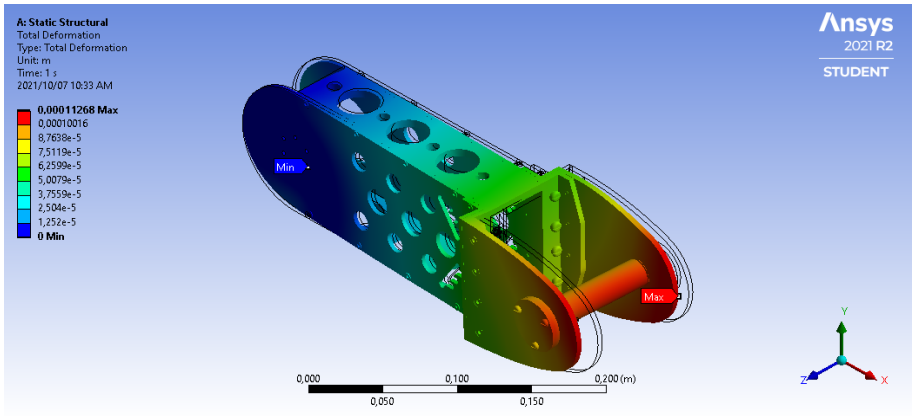

(b) Deformation Analysis

Figure 5.8: FEA simulation results of the femur limb structure.

Table 5.3 shows the maximum deformation and von-Mises stress for the use of standard grade aluminium 1050, which contains a tensile yield strength of 110 MPa. Examining the recorded maxima, the obtained FoS indicated that standard grade aluminium 1050 was a suitable grade of material for the design by surpassing the desired specification of 2. While the maximum recorded deformity was considered minute for the critical loading period of the robot indicating sufficient structural strength in the design of the limb.

Table 5.3: Factor of safety for the femur limb structure obtained from the FEA analysis.

Deformation (mm)	von-Mises Stress (MPa)	FoS
0.11268	47.475	2.317

5.2.2. Tibia Design

The tibia limb of the robot adopted a simplistic design comprising of three major components shown in Figure 5.9, namely the tibia yoke, cone and tube. Where, the yoke of the tibia consisted of three aluminium plates fastened together using machine

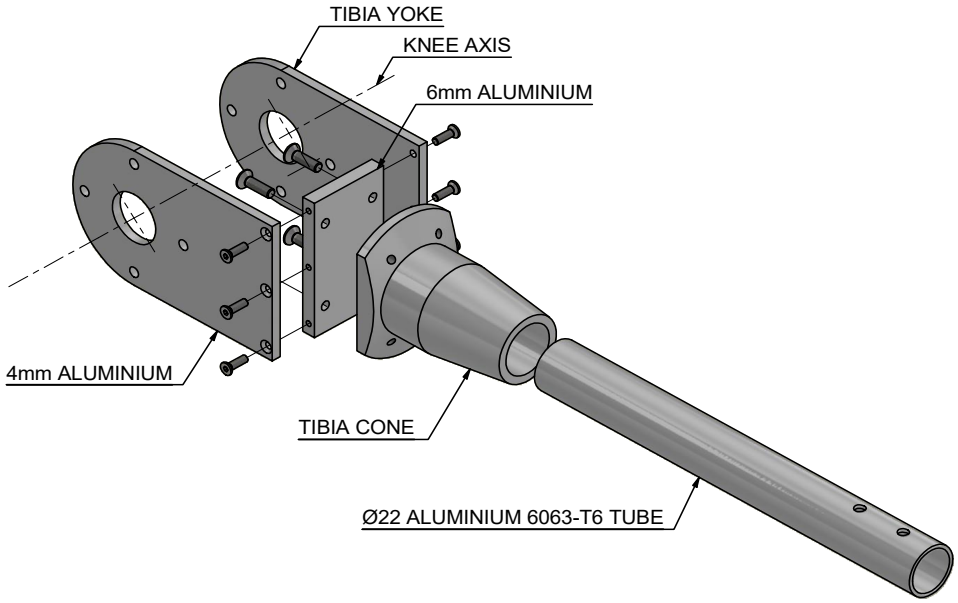

Figure 5.9: An annotated exploded view of the tibia assembly.

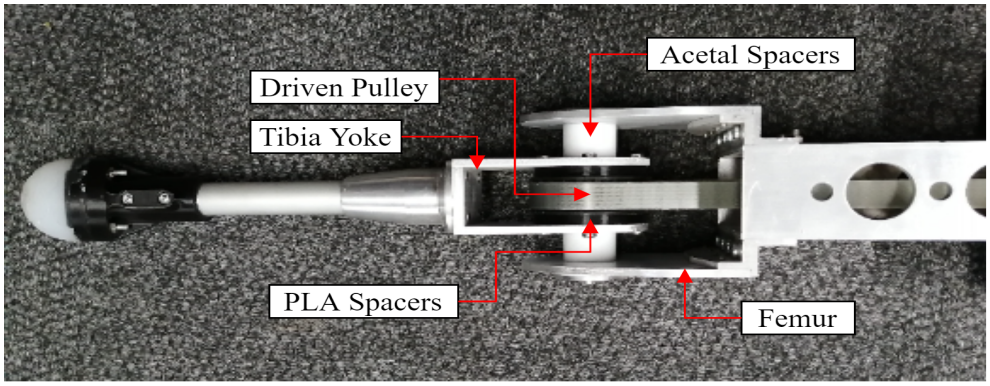

Figure 5.10: Labelled image of the knee joint identifying the components contributing to the torsional stiffness of the joint.

screws. The yoke essentially acted as a gimbal for the tibia limb, permitting the rotation of the structure about the knee axis. With the yoke forming the base of the structure, the remainder of the limb consisted of the tibia cone and tube; which were joined together using compound adhesive and attached to the yoke via machine screws.

A large effort was made to prevent the effects of twisting at the knee joint. With the driven pulley of the belt drive transmission located and fasten within the yoke of the tibia as shown in Figure 5.10. 3D printed PLA spacers were positioned between the walls of the yoke and the pulley to produce a compact and stiff joint. Ensuring the motion of driven transmission was directly transferred through the limb, without the effects of non-linear vibrations influencing the motion of the tibia due to a lack of joint stiffness. In addition, acetal spacers were placed on the knee shaft between the tibia and femur to prevent the joint from translating and twisting. Which eliminated the possibility of inducing unwanted

oscillations in the tibia and substantially increased the torsional stiffness of the knee joint.

Similarly to the femur design in Section 5.2.1, an FEA analysis was conducted to examine the structural behaviour of the tibia at the most critical loading period of a dynamic maneuver. During the structural simulation, the mounting holes located on the sides of the yoke were constrained to cylindrical supports; while a moment equivalent to the stall torque of the knee motor (24.8 N.m) was applied at the centre of the knee axis. An additional cylindrical support was applied to the tibia cone and tube to resemble the adhesive compound used to bond the two components. Lastly, a resultant force of 89.44 N, resembling the ground reaction force of a jumping maneuver obtained from the analytical analysis was applied at the end of the tibia.

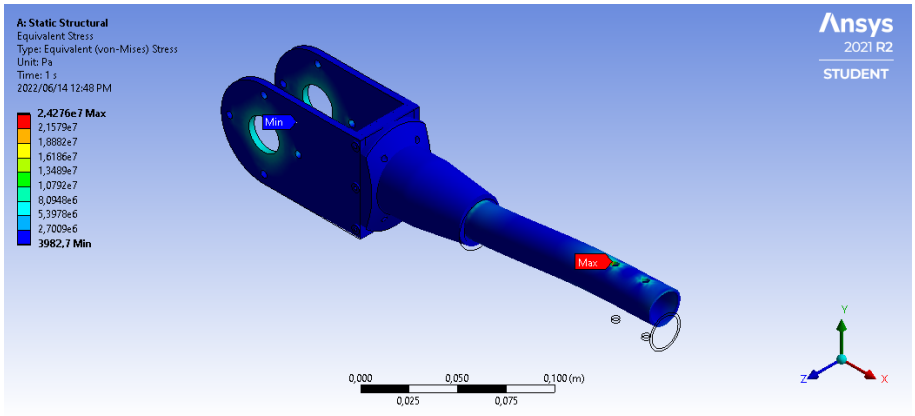

(a) von-Mises Stress Analysis

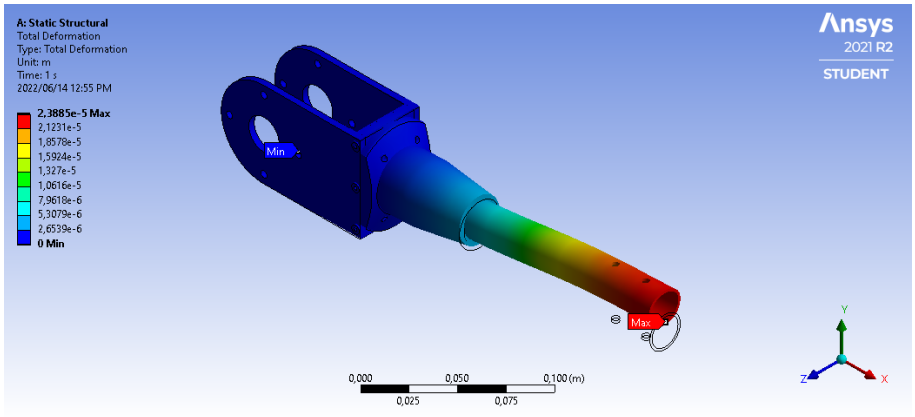

(b) Deformation Analysis

Figure 5.11: FEA simulation results of the tibia limb structure.

The analysis of the von-Mises stress and deformation results shown in Figure 5.11, showed the maximum stress location occurring on a mounting hole at the end of the tibia tube. While the minimum stress location was recorded on the side wall of the tibia yoke. Similarly to the femur FEA analysis, the maximum and minimum locations of the analyses were indicated by the red and blue tags respectively. The deformation analysis showed maximum deformity occurring at the cross sectional end of the tibia tube and minimal

Table 5.4: Factor of safety for the tibia limb structure obtained from the FEA analysis.

Deformation (mm)	von-Mises Stress (MPa)	FoS
0.023885	24.276	8.815

deformity occurring on one of the mounting holes located on the yoke. Furthermore, the initial wire outline of the structure shown in Figure 5.11 can be used to exaggerate the deformation of the structure from a visual perspective as it resembles a scaled version of the deformity. Lastly, the yoke and cone of the tibia utilised standard grade aluminium 1050 similar to femur components. Whereas, the tibia tube utilized aluminium 6063-T6 alloy containing a tensile yielding strength of 214 MPa. Examining the recorded maxima shown in Table 5.4, the obtained FoS for the tibia structure indicated that a suitable grade of material had been selected by surpassing the desired specification of 2. While the maximum recorded deformation was considered negligible indicating sufficient structural strength in the design of the limb.

5.2.3. Foot Design

As mentioned in Section 5.1, silicone rubber compound was selected as the molding material of the foot sole. Some guiding principles used to establish the foot design and justify the material selection were as follows:

1. Damping: Although an underdamped foot may behave in a oscillatory manner causing it to break contact with the ground during landing maneuvers [32], it is still capable of operating in a compliant manner through the implementation of an appropriate control scheme. Evidently, this was preferred over a well-damped foot which dissipates energy on each footstep.

2. Surface Contact: To avoid the foot from slipping during operation, a material with a high coefficient of friction was required. The natural tackiness of silicone rubber along with it's friction coefficient of approximately 1, motivated its selection as the foot sole material.

3. Versatility: As seen in nature, feet in animals are highly adapted to their living environment with the ability to change form based on their mode of usage, due to the hard and soft tissue material in their feet [94]. This adaptive behaviour makes replicating these complex biological structures extremely difficult with minimal known benefits in terms of additional compliance. Consequently, leading to the oversimplification of robotic feet in comparison to their animal counterparts [94]; with simplistic implementation approaches such as ball (point) feet [31] or compliant bending structures incorporating series elastic elements [95]. Therefore, an

interchangeable ball foot design was selected for the robot. Introducing versatility through an adaptable sole and allowing ground contact to be approximated as a discrete point.

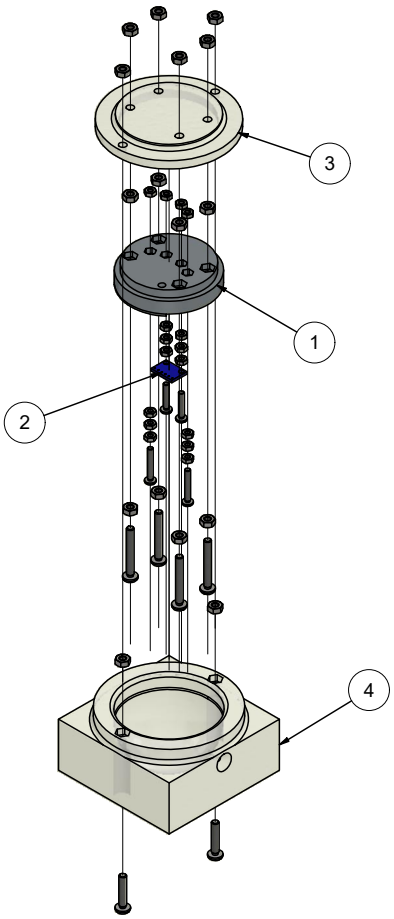

(a) Exploded isometric view identifying the major components of the molding assembly: 1) Sole Plate. 2) BMP280 Pressure Sensor. 3) Mold Lid. 4) Mold Cavity.

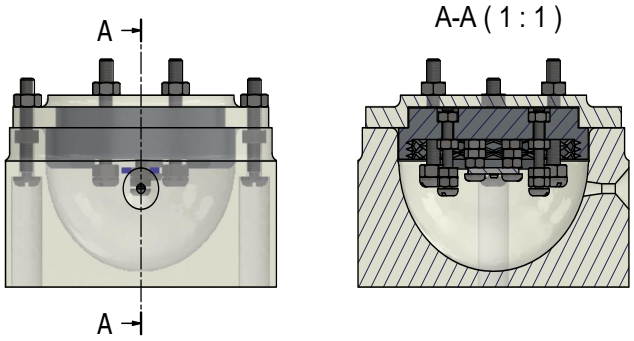

(b) Sectioned orthogonal view of the molding assembly showing the casting sprue located on the right hand side of the cavity.

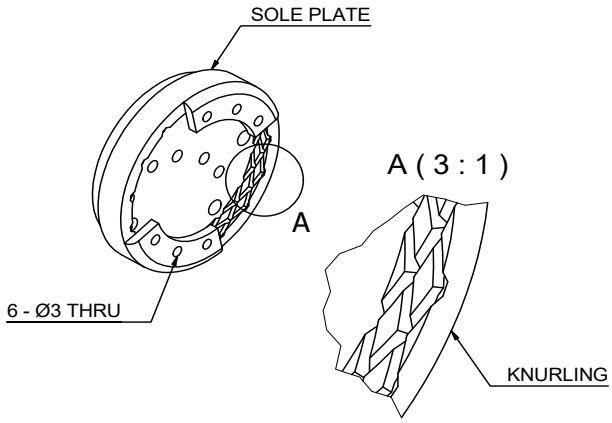

(c) Detailed sectional view of the sole plate showing the incorporated features used to aid the silicone rubber compound adhesion properties and increase the durability of the molded sole.

Figure 5.12: Inventor renderings of the molding assembly and detailed foot sole features.

Numerous challenges surrounded the molding process of the foot sole due to the unconventional molding nature of silicone rubber compound paste. This included concerns surrounding the viscosity and solidification properties of the molding material. Which led to the development of a custom mold design, as standard techniques such as casting and injection molding processes were unsuitable. Despite the unconventional nature of the compound paste, the custom mold consisted of a 3D printed cavity along with a sprue used to pump the material into the mold as seen in Figure 5.12a and 5.12b. However, additional standardized features such as runners and vents were unnecessary and excluded from the mold design due the prolonged solidification period of the paste.

To ensure proper adhesion between the compound paste and the 3D printed sole plate, four M4 bolts were fastened into the plate to provide additional contact surface. Further efforts to ensure durable adhesion included the incorporation of overhanging lips and knurling to the inner circumference of the sole plate as shown in Figure 5.12c. Lastly, a BMP280 pressure sensor was molded into the centre of the sole, allowing the author to obtain force feedback from the foot during ground contact.

5.3. Bipedal Platform

The modular design of the preliminary monopedal robot significantly aided in transitioning the robot into the desired bipedal form. Firstly, the extensive effort placed into design reviews, fault identification and debugging during the development of the initial prototype allowed the author to ensure all design flaws were addressed. Evidently resulting in a comprehensive functional unit. The expansion of the platform simply involved securing two monopedal units adjacent to each other, maintaining a concentric motor alignment. As can be seen by the final bipedal robot shown in Figure 5.13, two 3 mm aluminium 6063-T3 alloy angle iron extrusions were used to form the connective link between the two legs. The aluminium extrusions were fastened to the top plate of the individual torso's using M5 machine screws. In addition, the two M8 threaded rods featured in the torso of the monopedal design were extended to pass through the entire torso structure. Subsequently enhancing the stiffness of the structure, while mitigating previously encountered deflections.

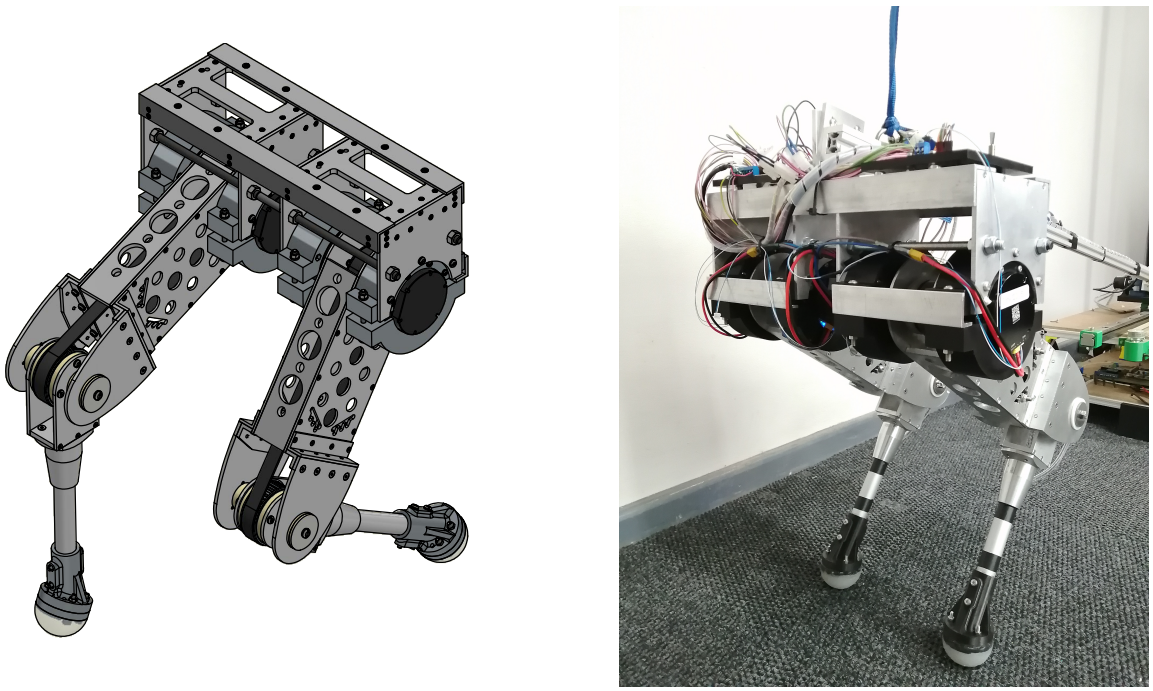

(a) (b)

Figure 5.13: (a) An isometric CAD rendering of the final robot design captured from the rear. (b) Front view of the assembled bipedal robot attached to the support system.

The final assembled bipedal robot including the onboard controller electronics weighed 8.91 kg. Whereas the effective weight of the robot, while attached to the boom arm of the artificial restraint system was measured at 9.1 kg. In comparison to the weight of existing bipedal platforms such as Baleka and ATRIAS, which measured at 15.62 kg [59] and 60 kg [41], respectively; the weight of the developed biped can seen as considerably lower. Therefore, the measured weight of robot can be viewed as a significant achievement in prioritizing the reduction of critical design parameters such as mass, as described in Section 4.1.

5.3.1. Sensing and Electronics

The developed electronic network used to control and enable the desired functionality of the robotic platforms consisted of an array of devices and sensors. A Teensy 4.0 micro-controller equipped with a ARM Cortex-M7 processor, operating at a clock speed of 600 MHz was selected to implement the robot's controllers. In addition, the Teensy 4.0 contains 40 digital IO pins, 3 SPI ports and 3 I2C ports; providing the robot with sufficient specification and features to allow on board processing and data capturing. Thereafter, captured data was transmitted via serial communication to a base station computer as shown in Figure 5.14.

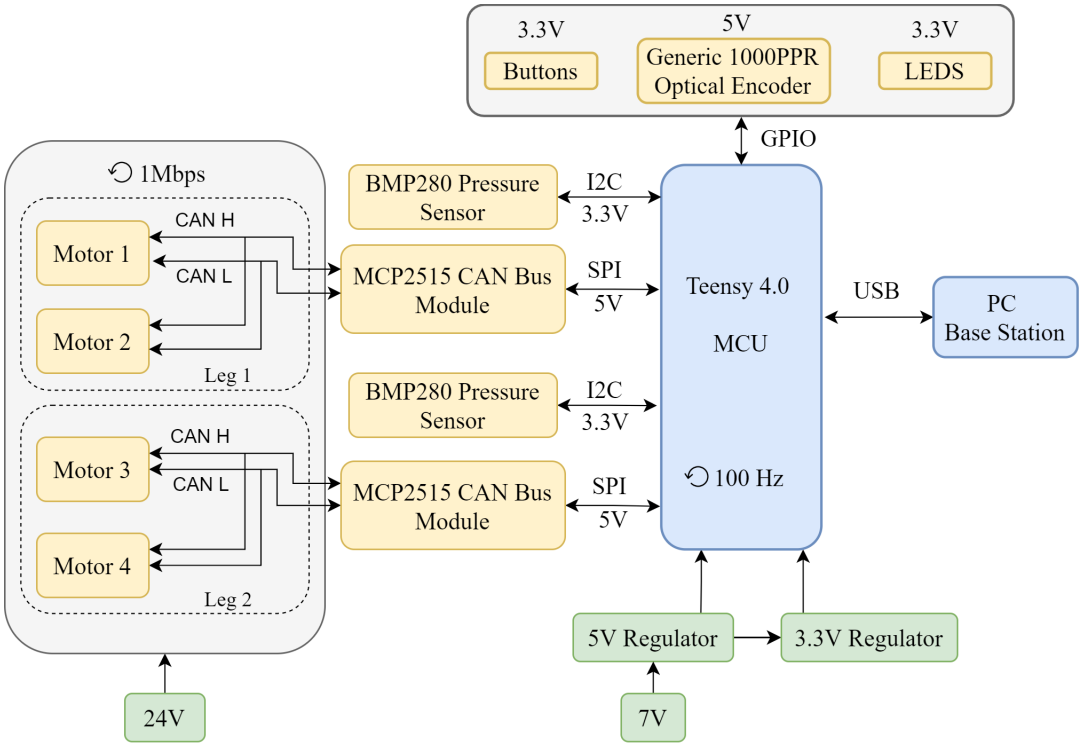

Figure 5.14: Functional block diagram of the bipedal system illustrating the respective communication protocols amongst the different devices along with their operating voltages.

Actuator communication was established through the use of two MCP2515 CAN Bus modules. The MCP2515 modules interfaced with the micro-controller via SPI

communication and were able to operate on the same bus using different chip select pins. Following the standard CAN communication protocol, 120 Ω termination resistors were connected across the CAN-H and CAN-L lines of the module. The four CubeMars AK70-10 motors were initialized and calibrated via UART through a serial to UART adapter at the start of the experimental testing phase. Once initialized the motors were enabled and received torque commands via CAN communication, operating at a baud rate of 1 Mbps. The oscillator frequency on the MCP2515 CAN module was set to 8 MHz to establish communication with the AK70-10 on-board motor controller. In addition, the motor's built-in 12-bit absolute encoders transmitted the joint position, angular velocity and applied torque at the executed control frequency of 100 Hz.

The two BMP280 pressure sensors molded in the feet of the robot were connected to the Teensy 4.0 micro-controller via I2C communication. This allowed the sensor to utilize the pressure difference upon impact to validate the proprioceptive force feedback received from the motors. In addition to the built-in absolute encoders, a Generic 1000PPR optical encoder was implemented at the pivot axis of the boom arm to capture the vertical height of the robot during experimental maneuvers. Communication between the micro-controller and optical encoder was established via GPIO pins to determine the direction and magnitude of the optical encoder through two phase pulse signals [12]. Furthermore, LEDs and buttons were implemented in the system through GPIO pins to indicate the operational state of the robots and serve as a safety mechanism to activate or de-activate the controller via a kill switch.

The electronic system was powered by a voltage regulated circuit consisting of a LM7805 (5V regulator) and MCP1700 (3.3V regulator). The circuit received an input voltage of 7V from a bench power supply and provided power to the independent components based on their required operating voltage. The motors were powered directly by an Aim-TTi QPX12000SP 1.2 kW bench power supply at 24V with an applied current limit of 35A. While conducting experiments on the bipedal platform, over voltage protection (OVP) issues were experienced with the power supply. The experienced OVP issues resulted due to a lack of shunt regulation required to dissipate regenerative energy created by the backdrivable motion of the motors. Notably, the motor manufacturers failed to specify if the internal motor controller compensated for regenerative energy using on-board shunt resistor. Consequently, the motor load was split between two power supplies to conclude the bipedal experiments. In the future, this problem can be avoided through the implementation of a shunt regulator or by replacing the bench power supply with lithium polymer (LiPo) batteries; which are capable of absorbing regenerative energy. However, as this problem was only encountered towards the final stages of testing the bipedal robot, replacing the power supply with LiPo batteries fell beyond the scope of this thesis.

5.4. Artificial Restraint System

From the literature covered in Section 2.4, some trade-offs between the pivot axis boom and 2-D planarizer systems were identified for the design of the robotic restraint system required to support and constrain the developed robots in the sagittal plane. Notably, traditional boom arm systems generally require large testing facilities to enable larger boom arms, typically 2 m in length [4], as larger walking circumferences are desired to emulate straight locomotion. Additionally, larger boom arm have the tendency to flex and impose on the dynamics of the robot. Whereas, 2-D vertical planarizer systems require fixed gantry structures and treadmills, which are expensive. However, both techniques of robotic restraint presented positive traits.

This resulted in the development of a concept to combine both techniques into an automated system capable of enabling forward locomotion within the sagittal plane, while utilizing a pivot axis boom arm. This was achieved through a vertical planarizing cart design as shown in Figure 5.15. The main objective of the cart system was to actively track and support the movement of the robot, while maintaining the pivot axis of the boom arm in the centre of the cart. Additionally, during the initial testing and periodic hopping maneuvers, the pivot axis could be clamped in the centre of the cart to avoid translation in the sagittal plane.

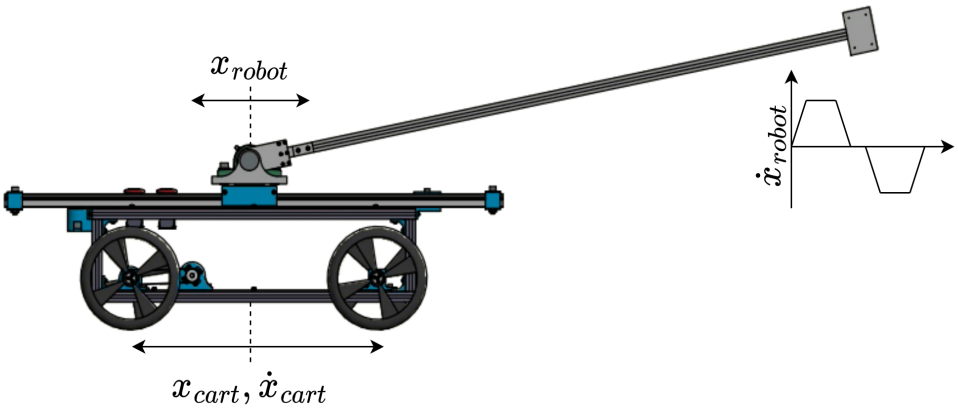

Figure 5.15: The concept of the vertical planarizing cart system. Note, the objective of the cart system was to maintain the pivot axis of the boom arm centred with respect to the cart as the robot accelerates or decelerates.

The research conducted in this thesis did not utilize the full functionality of the planarizing system, as the cart was constrained in a stationary position due to the limited testing period acquired to validate the dynamic capabilities of the developed robots. Therefore, details regarding the automation and control of the system were retracted from this thesis. However, the system was developed with future robotic maneuvers in mind and contained the desired hardware infrastructure to enable forward locomotion support

and tracking. Additionally, the Raibert control architecture used to inspire the virtual model controller detailed in Chapter 6, contained a forward velocity control component; which motivated the need for the developed restraint system to follow the motion of the robot.

5.4.1. Vertical Planarizing Cart

The vertical planarizing cart system was designed to consist of a light weight frame and boom structure with a maximum system mass of 15 kg; capable of achieving a forward velocity and acceleration of 1 m/s and 2 m/s^2, respectively. The orthogonal and isometric views of the developed cart system can be seen below in Figure 5.16 and 5.17.

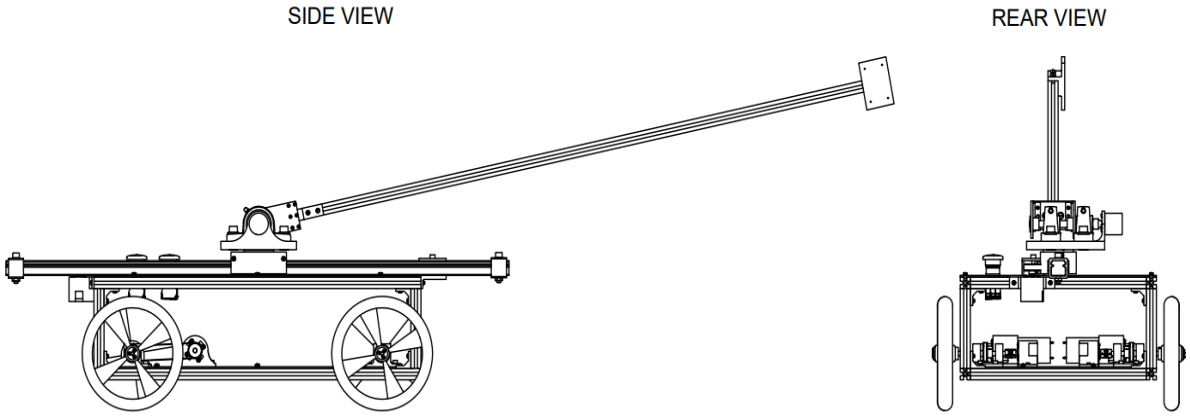

Figure 5.16: An orthogonal rendering of the developed vertical planarizing cart system.

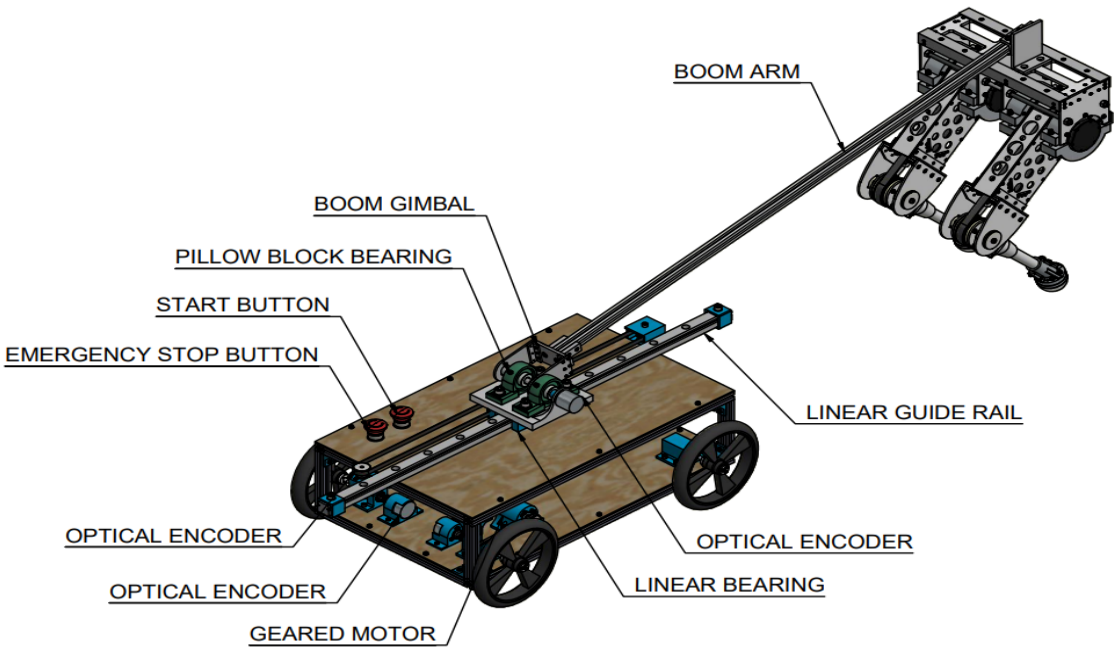

Figure 5.17: An annotated isometric rendering of the bipedal platform attached to the vertical planarizing cart system.

Hardware Infrastructure

The frame of the planarizing cart system was constructed using 20x20 mm aluminium extrusion and assembled through the use of 3D printed PLA connective brackets. Thereafter, 5 mm hardboard was attached to the aluminium structure to form the top and bottom surfaces, providing the cart with housing room for the system's electronics, wheel bearing blocks, actuators and linear guide rail. The actuator transmission designed to drive the system was located on the base surface of the cart and comprised of two 12V gear motors, fitted with planetary gearboxes containing gear ratios of $49:1$, along with maximum stall torques of 1.8 N.m. The geared motors utilized a belt drive transmission with a transmission ratio of $1:1$ to drive an offset output shaft connected to the rear wheels of the platform. In addition, optical encoders were coupled to each of the offset output shafts to monitor the rotational position of the motors.

A NSK NH30 linear guide rail and bearing block was situated on the top surface of the cart and ensured translation of the robot in the sagittal plane with minimal friction. Furthermore, the pivot axis of the boom was located directly above the linear bearing block and utilized two UCP201 pillow block bearings to support the rotating gimbal and shaft attached to the boom arm. Unlike traditional booms, the vertical constraint of the developed cart system allowed the length of the boom arm to be shortened to 1.2 m. Additionally, optical encoders were attached to the pivot axis shaft and the linear bearing block to capture the vertical and forward displacement and velocity of the robot during maneuvers. The buttons used to start and stop the robots controller were located on the top surface of the cart to ensure the safety of the operator in case the robot went unstable. Lastly, a simple connection between the boom arm and robot was established through a section of aluminium angle iron, which was fastened between the robot and the end of the boom arm.

5.5. Summary

This chapter detailed the iterative mechanical design process of the bipedal robot by presenting the initial concept generation phase leading up to the development of the monopedal prototype. Following the selection of the final monopedal concept, an extensive structural analysis of the individual limbs was provided, including a discussion on the belt drive transmission used to actuate the knee. Furthermore, the molding process of the robot's feet was covered followed by the expansion of the monopod to the biped, which discussed the systems electronics and communication protocols. Finally, this chapter concluded by detailing the vertical planarizing cart used to support and constrain the robot in the sagittal plane. Future recommendations can be found in Chapter 8.

Chapter 6

Controller Design

This chapter details the design of a validation controller used to embody the dynamic properties and characteristics of the developed system. The purpose of this controller was to effectively regulate the axial and rotational quantities of the robot in the sagittal plane to enable mechanical dexterity and emulate active compliance in the legs. With active compliance introduced through virtual model controllers, accurate force proprioception was enabled for the purpose of validating transient and agile locomotion.

Over the years numerous advanced control schemes for legged locomotion have been developed that mainly focus on the modelling of legged systems and effectively account for the system dynamics in great detail. The design of such a controller was considered beyond the scope of this thesis, as the focal point was placed on validating the developed platform. Therefore, a Raibert inspired controller in the form of virtual model control, as mentioned in Section 2.5, was selected to form the foundation of the virtual model control scheme by harnessing the natural dynamics of the system to inspire the emulated active compliance.

6.1. Raibert Controller

Raibert's research into actively balancing legged machines and locomotion in the early 1980's, led to the accomplishment of the first truely dynamic one-legged planar hopping machine [27]. The success of this platform was solely based of the development of Raibert's control algorithm, which allowed hopping in monopedal, bipedal and quadrupedal legged robots under the same control scheme implementation. Raibert's control framework avoided complex system modelling and decomposed hopping and running of legged machines into three simple parts:

1. Hopping height.
2. Forward velocity.
3. Body attitude (posture).

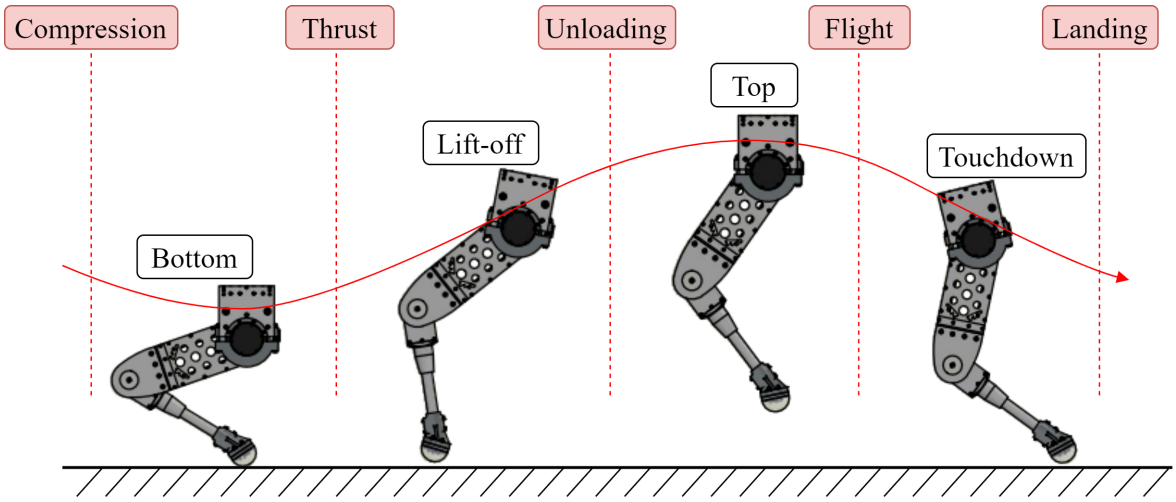

Figure 6.1: The four events encompassing the hopping and running cycle of a robotic leg, including the action states used in the finite state machine to define Raibert's hopping controller.

With each of the these parts forming decoupled 1-DoF controllers operating in parallel under a finite-state machine (FSM). The implemented states of the FSM were determined through the four events encompassing the hopping/running cycle of a legged machine; namely: 1) bottom, 2) lift-off, 3) top, and 4) touchdown as illustrated in Figure 6.1. Harnessing the natural dynamics of the cycle allowed Raibert's controller to embody dynamic motion through the following five action states [27]:

- Compression: The leg contracts during stance, rotating the body by actuating the hip to the desired attitude.
- Thrust: The pressurized leg extends, rotating the body by actuating the hip.
- Unloading: The leg extends to achieve the maximum virtual leg length, while terminating the thrust phase and removing the hip torque.
- Flight: The leg enters a ballistic trajectory phase as the foot becomes airborne and re-positions the leg for landing.
- Landing: The foot resumes ground contact with zero hip torque applied to the leg.

Raibert was inspired by machines developed in the early 1960's with the purpose of balancing inverted pendulums and identified the Spring-Loaded Inverted Pendulum (SLIP) model as being a primary tool and important precursor to future work in legged locomotion [27]. Subsequently, Raibert's three decoupled 1-DoF controllers were represented by the SLIP model. Similarly, this research (inspired through Raibert's controller shown in Figure 6.2) applies the SLIP model in the form of virtual compliance controllers; implemented in a FSM to emulate the action states obtained by Raibert's three decoupled controllers.

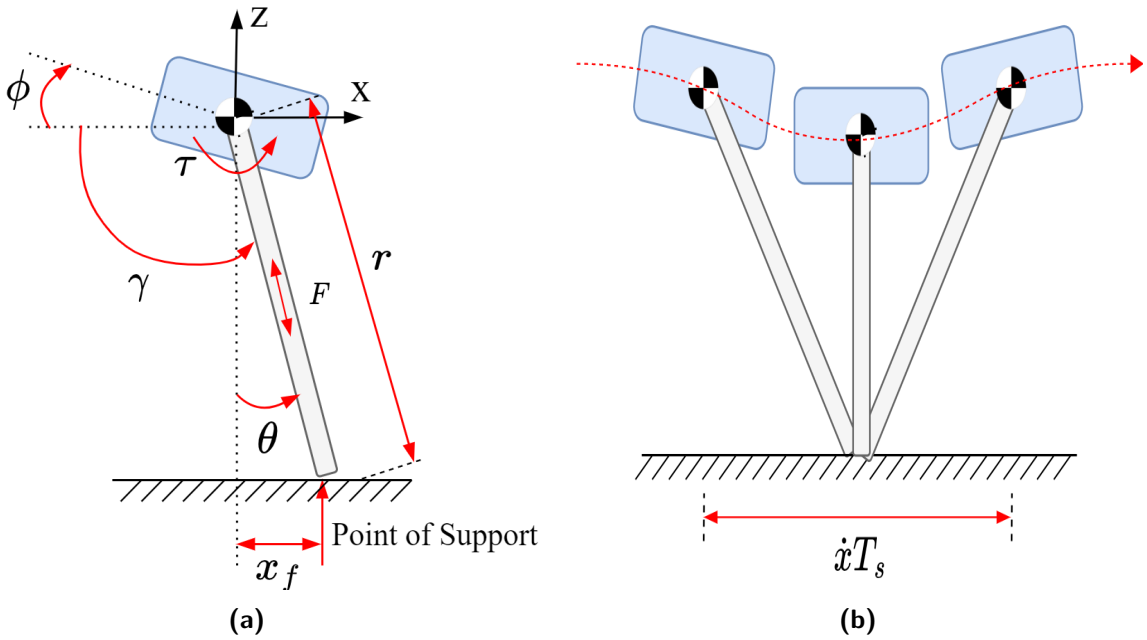

Figure 6.2: Diagram of a planar one-legged system used for Raibert's parallel control scheme. **(a)** A general SLIP model of the system showing the placement of the foot (x_f) relative to the body CoM (neutral position) to control the forward running velocity. Where ϕ represents the pitch angle of the body, θ represents the angle of the leg from the neutral point, τ represents the hip torque, r represents the leg length, γ represents the angle between the body and the leg and lastly, F represents the prismatic leg force. **(b)** A symmetric SLIP trajectory during stance, showing the modelled stride as a function of forward velocity ($\dot{x}$) and stance time (T_s).

Hopping Height

The first 1-DoF controller was used to regulate the height of the system during an excited cyclic hopping motion, by delivering vertical leg thrust during stance for a specified duration to sustain the oscillator motion of the machine. Where the delivered thrust force aids in accelerating the unsprung leg mass by inputting energy into the system to overcome energy lost due to friction or impact upon landing. With a complex relationship existing between the applied thrust and hopping height, Raibert suggested selecting a fixed thrust value which would produce an acceptable hopping height given a range of experiments.

Forward Velocity

The forward velocity controller regulates the forward speed of the system by determining the foot placement of the leg (x_{f0}) with respect to the body CoM during touchdown of a landing maneuver. Observing the symmetric trajectory of the stance state shown in Figure 6.2b, the neutral position of the foot occurs in front of the body CoM upon touchdown and ends behind the body CoM as the body moves forwards, preparing the leg for flight. The location of the foot's neutral position can be calculated using the stride duration and forward velocity of the symmetric motion as follows:

$$x_{f0} = \frac{\dot{x}T_s}{2}. \tag{6.1}$$

The symmetry of the SLIP model on touchdown results in a net forward acceleration of zero at the neutral position. As the forward and backward tipping motions of the system compensate for each other during stance, which balance the horizontal components of the axial leg force and assume the axial leg force to be an even function of time during stance. A non-zero net acceleration can be created by introducing asymmetric motion through displacing the foot touchdown placement, either behind or in front of the neutral position. The foot placement (x_f) is determined using following algorithm, where $k_{\dot{x}}$ represents a feedback gain and $\dot{x_d}$ represents the desired forward velocity [27]:

$$x_f = x_{f0} + k_{\dot{x}}(\dot{x} - \dot{x_d}). \tag{6.2}$$

After determining the desired foot touchdown placement, the algorithm proceeds to compute the angle (γ) between the leg and the body using the inverse kinematics of the model. With the SLIP model shown in Figure 6.2a only consisting of leg length and the hip angle, simple manipulation of the inverse kinematics reduces γ to the following:

$$\gamma = \phi - \arcsin\left(\frac{\dot{x}T_s}{2r} + \frac{k_{\dot{x}}(\dot{x} - \dot{x_d})}{r}\right). \tag{6.3}$$

Lastly, torque is applied to the pitch angle of the legged robot to achieve the desired body posture and stabilize the leg during stance. The following torque formula is used to control the pitch angle, where k_p and k_v represent position and velocity feedback gains respectively and $\dot{\gamma_d}$ represents the desired angle:

$$\tau = -k_p(\gamma - \gamma_d) - k_v(\dot{\gamma_d}). \tag{6.4}$$

Raibert implemented each of the three formulae forming part of the forward velocity controller as closed loop controllers. With the foot placement algorithm utilizing a simple Proportional (P) controller, whereas Proportional and Derivative (PD) controllers were implemented for the hip torque and γ angle algorithms.

Body Attitude

The body attitude controller forms the final 1-DoF controller in Raibert's decoupled control scheme, which was responsible for maintaining an upright body posture during stance by applying torques about the hip; to servo the pitch of the body. Furthermore, the body attitude controller regulates the systems change in angular momentum during stance, as a result of the friction between the foot and ground, without subjecting the leg to large

accelerations [27]. The body attitude algorithm is defined as follows:

$$\tau = -k_p(\phi - \phi_d) - k_v(\dot{\phi}). \tag{6.5}$$

Similarly to the applied torque algorithm implemented in the forward velocity controller, the body attitude controller utilizes a PD controller with k_p and k_v representing the position and velocity gains respectively.

Therefore, Raibert's three decoupled parallel 1-DoF controllers detailed through this section were used to inspire a virtual model control template discussed in the following section. Which enabled the controller to condense Raibert's framework into a single dynamic controller. This effectively allows the robot to assess each of Raibert's 1-DoF controllers based on the desired locomotion by dynamically altering the system control parameters in real time through a state machine implementation.

6.2. Dynamic Virtual Model Control

The virtual model control strategy initially developed by Pratt et al. [96] is a force-based motion control framework for planar bipedal walking robots. The control framework utilizes virtual components to emulate active compliant forces during interactions between the robotic system environment and the virtual components. The notion of virtual model control is directed toward borrowing ideas from traditional techniques such as hybrid position-force control, stiffness control and impedance control to characterize a desired system with a simple set of virtual components [96].

Similarly to Raibert's controller, virtual model control avoids complex system modeling and mitigates the use of inverse dynamics, due to the computational complexity associated with plant inversion and the created contrast in comparison to the natural dynamics of the system. Instead, virtual model control augments the natural dynamics of the system with virtual components to achieve mechanical dexterity though mimicking physical components such as mechanical springs, dampers, masses, dashpots, latches and nonlinear potential fields [3, 96]. Inspired by Raibert's control algorithm, the virtual model control framework functions in terms of setpoints, which serve as targets for the controller and are dynamically altered within the FSM. This allows the system to smoothly transitions between states and emulate the behaviour demonstrated by Raibert's planar hopping controller.

6.2.1. Impedance Control

Considering the above mentioned complexities in Section 6.2, including the irregularities emerging through the hybrid nature of underactuacted robots during periods of rapid

transition [33]; a virtual model controller was inspired through traditional techniques. Therefore, a closed loop Cartesian impedance controller was implemented to embody the virtual components of the robot [66]. The controller made use of a simplified SLIP model control template, which regulated the stiffness and damping quantities of the robot using the radial position and velocity of the modelled leg. The SLIP template consisted of two spring-damper models, namely a prismatic model and a rotational model as shown in Figure 6.3. The prismatic spring-damper model defined by Equation 6.6 served in generating a force, F_v required to excite a hopping motion and mimic Raibert's hopping height controller. Whereas, the rotational model controlled the posture of the leg by generating a torque, τ_v, defined by Equation 6.7 used to place the foot at a desired location.

$$F_v = -K_l(r - r_{neutral}) - C_l\dot{r} + F_{thrust} \tag{6.6}$$

$$\tau_v = -K_\theta(\theta_v - \theta_{neutral}) - C_\theta\dot{\theta}_v \tag{6.7}$$

Where K_l (N/m) and K_θ (N/rad) represent the prismatic length and rotational spring coefficients of the models respectively. Similarly, C_l (Ns/m) and C_θ (Ns/rad) represent the damping coefficient of prismatic length and rotational models. $r_{neutral}$ defines the virtual leg length setpoint and $\theta_{neutral}$ defines the neutral rotational angle setpoint of the virtual leg. The prismatic spring-damper model includes a user defined force, F_{thrust}, used to experimentally determine and regulate the hopping height during the thrust phase of the robot.

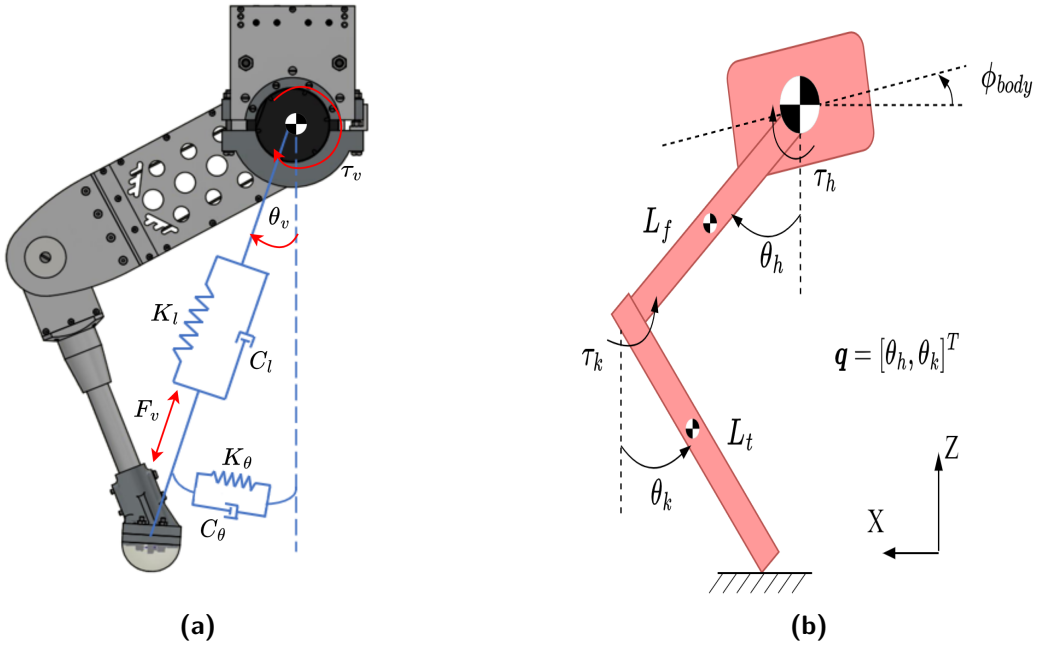

Figure 6.3: **(a)** Overlay of the Spring Loaded Inverted Pendulum (SLIP) template on the developed platform, illustrating the two spring-damper models used to control the leg length and angle of the robot. **(b)** Generalized coordinates and actuated joints of the physical robot.

The closed loop impedance controller was implemented at a frequency of 100 Hz, which proved to be sufficient in executing the agile and transient maneuvers conducted on the robot. Through dynamically altering the prismatic and rotational setpoints, spring constants and damping coefficients; the behaviour demonstrated by Raiberts forward velocity and body attitude controllers could be emulated within the virtual model controller. However, due to the spring-damper model's use of radial quantities, a transformation from polar to the Cartesian coordinate frame was required. This was achieved through Equation 6.8, which was used to the map the desired virtual components determined through the impedance controller into the joint space required by the respective motors.

$$\begin{bmatrix} \tau_h \\ \tau_k \end{bmatrix} = \boldsymbol{J}_v^T \begin{bmatrix} F_v \\ \tau_v \end{bmatrix}, \tag{6.8}$$

$$\boldsymbol{J}_v = jacobian([r, \theta_v], \boldsymbol{q}). \tag{6.9}$$

Where the Jacobian matrix ($\boldsymbol{J}_v$) shown in Equation 6.9 represents the Jacobian of the robots virtual leg components with respect to the generalized coordinates of the physical platform, denoted by $\boldsymbol{q}$ and illustrated in Figure 6.3b.

6.2.2. Torque Mapping Simulation

A simulation of the virtual model controller was created in MATLAB's Simulink environment for the purpose of verifying the controller behaviour and torque mapping transformation. An active 2-DoF monopod model, as shown in Figure 6.3b was used to simulate the prismatic and rotational 1-DoF spring-damper models at 100 Hz. The simulation comprised of exciting the 2-DoF leg with a minor thrust force to verify the direction and magnitude of the resulting torques. As well as examine the oscillatory behaviour of the virtual components, influenced by the spring constants and damping coefficients. Furthermore, the simulation was used to assess controller parameters during the initial selection process. The implemented control architecture of the simulation is shown below in Figure 6.4.

The simulation began by defining the EoM of the active 2-DoF leg, which followed the manipulator equation described in the trajectory optimisation model setup in Section 3.4. The EoM included a set of initial position and velocity conditions for the robot. The joints acceleration denoted in terms of generalized coordinates and illustrated by $\ddot{\boldsymbol{q}}$ in Figure 6.4, proceeded through integrator blocks to determine the joint velocity, $\dot{\boldsymbol{q}}$, and position, $\boldsymbol{q}$ of the robot.

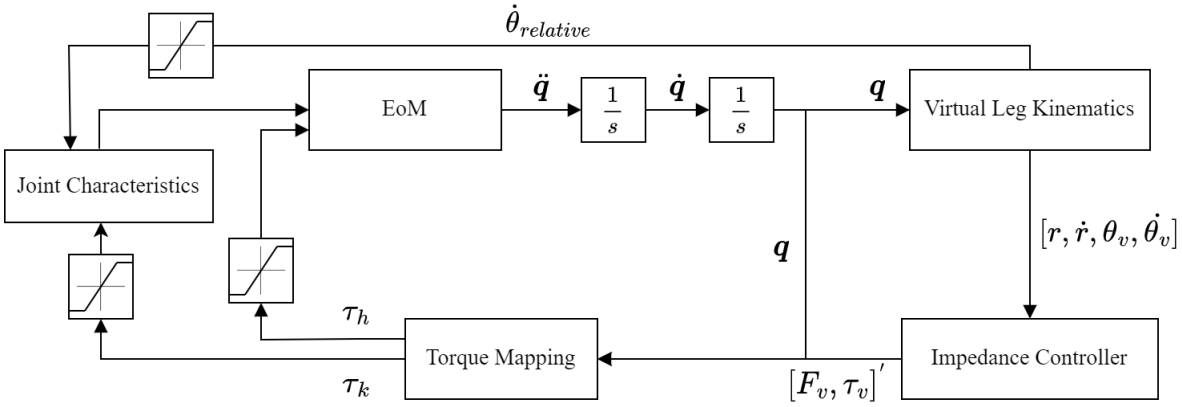

Figure 6.4: Schematic of the control architecture used in the Simulink simulation to verify the impedance controller and torque mapping before executing it on the physical robot.

Thereafter, the virtual length and angle of the leg, including the derivatives of these variables were determined using the kinematic model. The impedance controller proceeded to utilize these kinematic quantities to enforce the virtual spring-damper models on the system. The virtual force and torque components of the controller, together with the updated generalized coordinates were transformed and mapped to the required motor torques through the relationship of the Jacobian transpose. Additionally, the knee motor torque was scaled by a factor of 0.8 during the mapping process to account for transmission ratio of the belt drive system.

Lastly, the calculated joint torques were limited within the velocity and torque saturation bounds of the motors. While the mapped knee torque (τ_k) was passed through a joint characteristic function defined by the following piecewise linear function:

$$\tau = \begin{cases} \left(\frac{-\tau_{max}}{\omega_{max}}\right)\dot{\theta}_{relative} + \tau_{max} & \tau_k > \tau, \\ \left(\frac{-\tau_{max}}{\omega_{max}}\right)\dot{\theta}_{relative} - \tau_{max} & \tau_k < \tau. \end{cases} \tag{6.10}$$

Which ensured the relative joint velocity subjected to the knee motor torque, denoted by $\dot{\theta}_{relative}$, remained constrained within the motor's limitations. Once regulated by the saturation limits, the joint torques were used to update the EoM function for the next time iteration; resulting in a simulated system loop.

6.3. Finite State Machine

A sequential finite state machine (FSM) was implemented to determine the control state required to achieve the desired motion of the robot based on the defined events used to transition states. The monopod and bipedal robots were able to operate under the same FSM template. Despite the difficulties that come with controlling multiple legs, operating

the control template on both robots was possible through executing identical maneuvers (continuous hopping) during the validation process.

6.3.1. FSM Implementation

The FSM controller used to implement the closed loop impedance algorithm described in Section 6.2.1 comprised of two distinct states, namely a **Stance** and **Flight** state. Upon examining the events encompassing the hopping cycle of a robot shown in Figure 6.1; additional controller distinctions were established and resulted in the division of the stance state into two sub-states being **Thrust** and **Stance**. Furthermore, the ballistic motion experienced by the robot between the lift-off and touchdown transition events was used to promote a simplified flight state; utilizing the momentum generated during the thrust state along with the influential role of the systems natural dynamics to maintain stable motion. Additionally, the thrust and stance sub-states were activated while the foot of the robot remained in contact with the ground and allowed the two action states to be categorized as a single state.

The FSM implementation of the three established control states effectively provided the virtual model controller with the framework required to emulate Raibert's control architecture. In the case of forward hopping motion, the flight state of the FSM would enable the controller to represent Raibert's forward velocity controller, while the stance state would represent the body attitude controller and lastly, the thrust state would emulate the hopping height and body attitude controllers. However, due to the fixed body periodic hopping maneuvers conducted in this thesis to validate the developed robots, only Raibert's hopping height controller was replicated through the virtual model controller.

A simplified flow diagram of the FSM hopping template shown in Figure 6.5 was implemented on the Teensy 4.0 micro-controller. Before entering the state machine, the virtual length ($r_{neutral}$) and angle ($\theta_{neutral}$) setpoints of the system were defined during the initialization process to position the robot in an initial crouched orientation. Note, the initialization process occurred while the robot was suspended above the ground, with the foot of the robot supported at the desired virtual length to ensure consistency during repetitive experiments. Once initialized in the crouched orientation, the robot was placed on the ground to resume surface contact. Thereafter, the controller entered a 30 s buffer period prior to activating the state machine; providing the author with sufficient time to ensure all communications system and data logging procedures were actively responding to record the experiment.

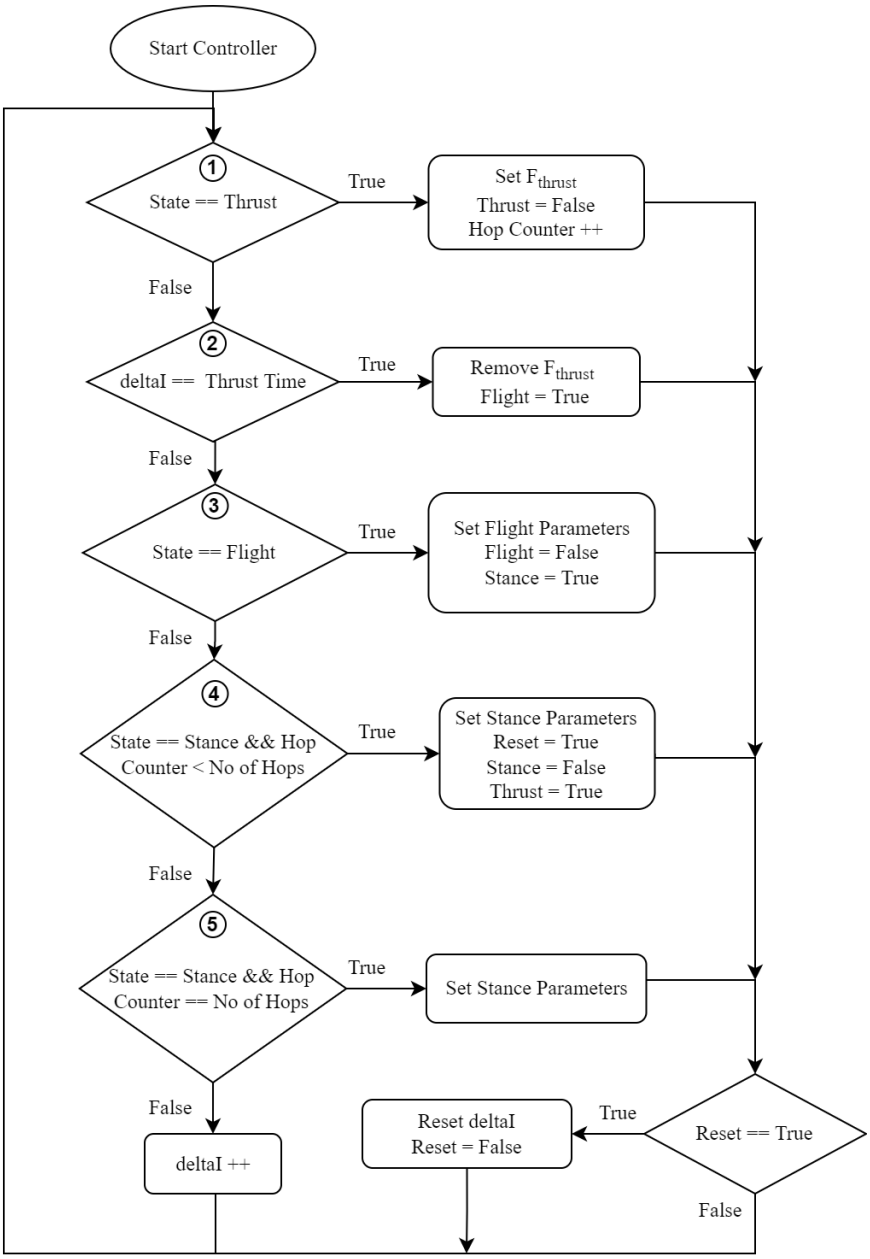

Figure 6.5: Simplified flow diagram of the FSM hopping template implemented on the Teensy 4.0 MCU.

The thrust state was initiated upon entering the FSM controller, exciting the robot with the desired thrust force and incrementing the number of performed hops. The prismatic and rotational spring-damper models proceeded to deliver thrust for approximately 170-200 ms (thrust time); which was regulated by the variable, *deltaI,* used to record the number of sample times, shown in the second argument of Figure 6.5. Once the thrust time had expired, the force was removed from the system and the flight state was activated using force proprioceptive feedback from the motors to determine the lift-off instance. As state transitioning occurred from thrust to flight, the virtual length setpoint of prismatic spring-damper model was updated to the virtual length of the robot at the lift-off instance. This reduced the oscillations experienced

by the robot while dynamically repositioning the foot during flight. In addition, the virtual angle setpoint was initialized to zero and remained constant throughout the FSM to maintain the foot of the robot in a vertical position throughout state transitions.

As the robot experienced ballistic motion, the flight state of the sequential controller was maintained in anticipation for landing. Once touchdown had occurred, the stance state was activated under the condition that ground contact had resumed and the height of the robot was equivalent to the initial torso height recorded in the crouched position. The ground contact condition was evaluated using force proprioceptive feedback and resulted in a flight time of approximately 500 ms from thrust to touchdown. Furthermore, the virtual length setpoint of the controller was updated during the stance phase to the initial setpoint value used to orientate the robot in the crouched position. If the robot was required to perform multiple hops; the state machine proceeded to reset the variable, *deltaI*, before transitioning back to the thrust state to repeat the hopping cycle. Lastly, if the number of desired hops had been achieved; the stance controller actively maneuvered the robot through the bottom phase of the landing and concluded the hopping cycle with the robot oriented in the initial crouched position.

6.3.2. FSM Control Parameters

The impedance controller parameters were determined using disturbance responses produced by initial experiments conducted on the robotic platforms. The MATLAB Simulink simulation aided in validating the stability of these control parameters prior to their implementation on the robot to ensure the safety of people within the direct testing vicinity. Despite simulating the initial control parameters, minor teething problems were experienced with the stability of the system while generating the disturbance responses. Notably, the stability problems encountered during this process occurred while the robot was airborne as the MATLAB Simulink simulation only accounted for ground contact conditions.

Therefore, the numerous non-linear effects experienced by the robot during flight were not simulated. However, through consulting the following literature [3, 8], the flight state controller parameters were adapted accordingly to produce stable motion by lowering the stiffness of the virtual spring and enforcing a virtual leg length setpoint equivalent to take-off length. The disturbance responses obtained from the initial compliant disturbance test conducted on the physical robot were able to display the systems behaviour, including the compliance and non-compliance of the robot across a range of stiffness and damping values. Through assessing the disturbance responses, suitable controller parameters were selected for the FSM of the hopping controller. Further details regarding the disturbance

response and behaviour of the system are provided in Chapter 7.

Table 6.1: Stiffness and damping impedance parameters implemented in the FSM controller phases of the hopping cycle.

	Monopod			Biped		
Controller Parameters	Thrust	Flight	Stance	Thrust	Flight	Stance
K_l [N/m]	1200	750	1250	1200	750	1250
C_l [Ns/m]	65	40	65	45	40	45
K_θ [N/rad]	15	20	15	15	20	15
C_θ [Ns/rad]	3	3	3	3	3	3
F_{thrust} [N]	150	0	0	120	0	0

The stiffness and damping impedance parameters used throughout the states encompassing the hopping cycle of the monopod and bipedal robots are detailed in Table 6.1. Notably, very few distinctions emerged between the state parameters of the two robots with the only distinctions being the applied thrust force and damping coefficient of the prismatic model. The stiffness and damping controller parameters for the thrust and stance states were selected based on the requirement that the parameters were capable of supporting the effective weight of the robot while maintaining stability. Therefore, due to the single contact point supporting the effective weight of the monopod robot; a moderately higher damping coefficient was implemented on the prismatic model. Effectively reducing oscillations and ensuring the vertical posture and balance of the robot. Whereas, the additional contact support and even weight distribution created by symmetry about the sagittal plane allowed the bipedal robot to operate under a lower damping coefficient. As disturbances were balanced between the two legs during surface contact.

The flight state impedance parameters remained constant throughout both robots. During this phase of the FSM, the spring constant and damping coefficient parameters were decreased to avoid oscillations created while re-positioning the foot of the robot during ballistic motion. Essentially increasing the influence of the rotational model while preparing the leg for landing. Upon the touchdown instance of the leg, the stiffness and damping parameters were increased as the controller transitioned to the stance state to absorb the impact of landing. In addition, the increased spring constant enabled the robot to complete the hopping trajectory as close as possible to the initial crouched height. Lastly, the thrust force used to excite the hopping trajectory of the two robots was experimentally determined, as described by Raibert's hopping height controller to achieve a sustainable hopping cycle. However, the thrust force used to excite the bipedal robot

was also limited by the OVP power supply issues encountered during the later stages of testing as mentioned in Section 5.3.1.

6.4. Summary

This chapter provided a detailed discussion into the operation of Raibert's controller, including the transition events and states required to initiate and maintain the hopping cycle of a legged robot. Inspired by Raibert's control architecture, this chapter presented the development and implementation of virtual model control in the form of an impedance controller; used to emulate active compliance by harnessing the natural dynamics of the system. The impedance controller embraced the SLIP model template through the use of a prismatic and rotational spring-damper model. A MATLAB Simulink simulation was conducted to verify the controller prior to physical implementation and assess the behaviour of control parameters. Furthermore, details regrading the FSM used to implement physical hopping on the robot were provided. Lastly, this chapter concluded with the discussion and selection of initial control parameters.

Chapter 7

Physical Experiments and Validation

The following chapter details the physical platform experiments conducted to validate the dynamic performance of the developed monopedal and bipedal robots. The experiments covered in this chapter are categorized into three subsets. Firstly, the calibration procedure and testing setup for the robot will be discussed along with the initial experiments performed to examine the control behaviour of the robots. Thereafter, the vertical specific agility of the robots are provided through single hop tests from an initial stationary position, followed by continuous hopping tests used to validate the simulated trajectory model. In concluding this chapter, a discussion based on the notable results and characteristics observed throughout the experiments are provided. Additionally, a video repository of the hopping maneuvers conducted and discussed throughout this chapter can be found here.

7.1. Initial Robot Experiments

This section details the initialization and calibration procedure of the developed robots, including the initial experiments used to examine the robots' behaviour using the implemented virtual model controller discussed in Section 6.2. The initial performed experiments consist of disturbance and drop tests used to observe the robots' control behaviour while in contact with the ground and upon landing; motivating the control parameter selection embodied by the hopping control sequence displayed in Table 6.1.

7.1.1. Robot Initialization and Calibration

The initialization process of the experimental setup consisted of suspending the developed robots' from an elevated wall bracket using a ratchet strap and claw hook, attached to the boom arm of the system. The ratchet strap served as a safety mechanism to hoist the robot in the event of instability to avoid damaging any robotic components through undesirable impacts. Additionally, the vertical planarizing cart was elevated off the ground through the use of 3D printed PLA blocks to ensure the cart remained stationary during testing; while the linear bearing block was clamped in the centre of the linear guide rail to prevent the robot from translating. The vertical orientation of the robot and boom arm angle illustrated by the yellow dashed lines in Figure 7.1 shows the calibrated zero

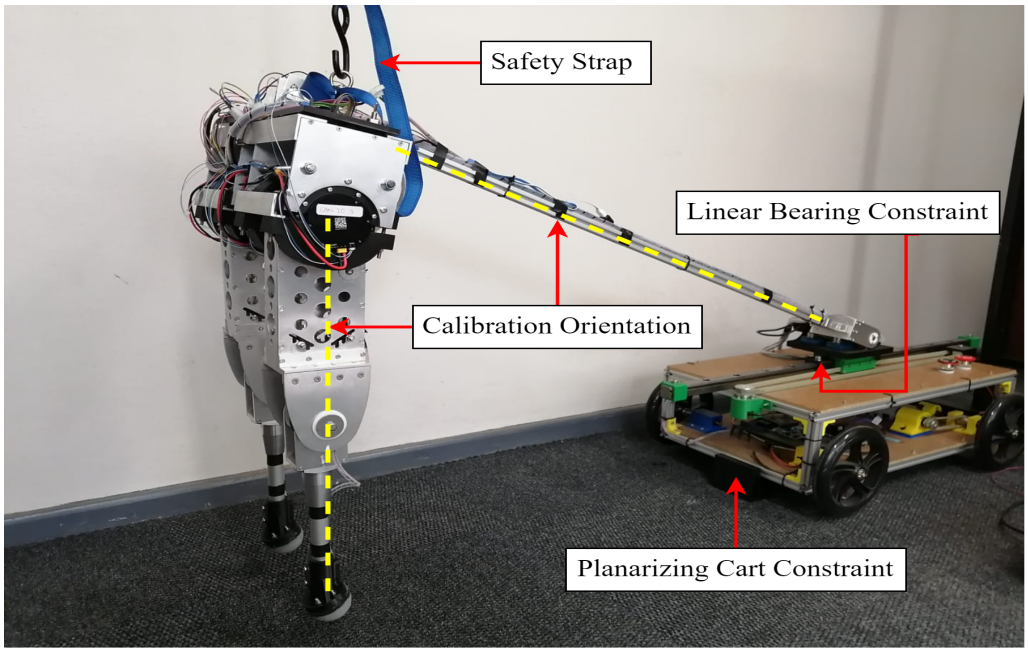

Figure 7.1: The initialization and calibration orientation of the biped robot before each conducted experiment. Note, the implemented features to constrain the planarizing cart and linear bearing block in a stationary position.

position of the experimental setup.

The CubeMars Upper Computer Program was used to calibrate the on-board absolute encoders of the motors and set the vertical zero position of the mechanical limbs on the built-in motor controller via a UART connection. Notably, the motor calibration process was performed once at the start of the testing phase of the robot. Furthermore, during this calibration phase the CAN ID's of the respective motor controllers were initialized and utilized CAN ID 1 to 4. Following the calibration process, at the start of each experiment a wooden stand was placed beneath the robot to support the feet of the system; while manually configuring the orientation of the joints to attain a desired neutral length for the virtual model controller. Thereafter, the physical virtual model controller could be activated.

7.1.2. Disturbance Test

Virtual compliant disturbance tests were conducted over a range of damping values to observe the oscillatory behaviour of the system. The main objective of this experiment was to determine damping coefficients that produced minimal oscillations for a spring constant capable of supporting the weight of robot within 5% of the desired neutral length setpoint; while promoting stable and compliant maneuverability during ground contact. The testing setup illustrated in Figure 7.2, consisted of setting the neutral length setpoint ($r_{neutral}$) of the robot to 0.4 m (approximately 75% of the fully extended length) and placing the robot

on the ground. Thereafter, a downward disturbance force was applied on the robots torso and released to observe the systems response. Implementing a neutral length of 0.4 m for the virtual spring model allowed the robot to generate a larger virtual force, due to an increased displacement in length created by the applied force. Evidently, producing a more distinct system response. Additionally, the controller's neutral angle setpoint ($\theta_{neutral}$) was maintained at 0 rad throughout the conducted disturbance tests.

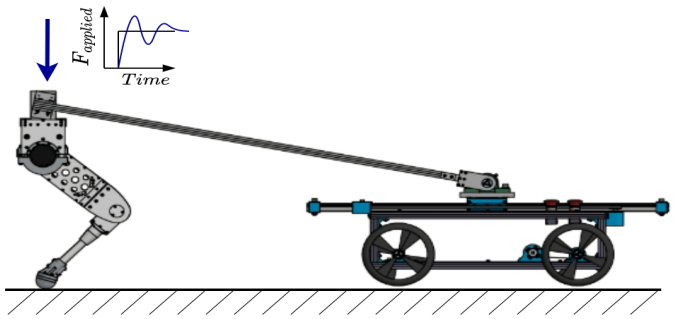

Figure 7.2: An illustration of the disturbance testing scenario involving an applied force on the robots torso to examine the oscillatory behaviour system in contact with the ground.

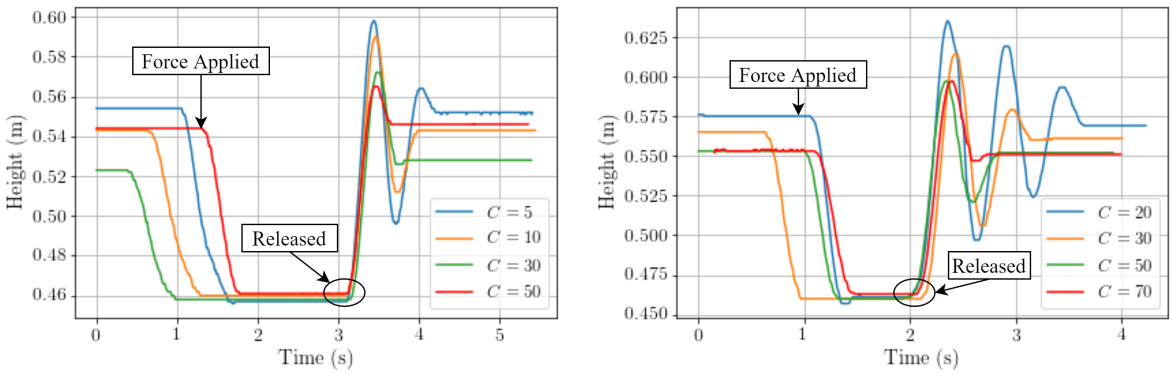

(a) Monopedal Response **(b)** Bipedal Response

Figure 7.3: The disturbance responses for the monopod and biped robots using a virtual spring constant of $K_l = 1350$ N/m. Notably, the biped experienced increased oscillatory behaviour in comparison to the monopod, which exhibited moderately damped behaviour.

The monopedal disturbance responses shown in Figure 7.3a exhibited moderately damped behaviour with the damping coefficients of 30 Ns/m and 50 Ns/m only experiencing minor overshoot of approximately 2 - 4 cm, before settling at the robots initial height. Whereas, the disturbance responses for the lower damping coefficients of 5 Ns/m and 10 Ns/m, produced a single oscillation containing an amplitude of approximately 5 cm. This revealed the system's robustness against disturbances on the ground, however, damping coefficients above 30 Ns/m were preferred for the stance phase of the hopping sequence to ensure system stability.

The biped disturbance responses shown in Figure 7.3b presented increased oscillatory behaviour compared to the monopod robot, with the damping coefficient of 20 Ns/m producing multiple oscillations while containing a maximum amplitude of approximately 6 cm. Additionally, this response exhibited undesired motion as the robot broke contact with the ground upon the release of the applied force. Despite the increased oscillation, the spring-damper system was able to maintain stability throughout each of the disturbance responses. Similarly to the monopod, increased damping coefficients (specifically 50 Ns/m and 70 Ns/m) experienced minor overshoot containing amplitudes of approximately 5 cm and were preferred for the stance phase of the hopping sequence. Furthermore, discrepancies between the behaviour of the two robots were due to the additional force contributed by the second leg of the biped, along with additional contact point which aided support and allowed the weight of the boom arm to be equally distributed over both legs.

7.1.3. Force Transparency Test

Force transparency through the use of proprioceptive feedback is a highly desired feature in legged robots as discussed throughout the literature study. Therefore, virtual compliant drop tests were conducted to validated the accuracy of the force transparency and observe the robots' behaviour during landing maneuvers over a range of spring constants. The system setup for the compliant drop tests illustrated in Figure 7.4, consisted of manually suspending and releasing the robot from an airborne position to observe the ground contact behaviour. Similarly to the disturbance test, the following experiments implemented a virtual neutral length setpoint ($r_{neutral}$) of 0.4 m and virtual neutral angle setpoint of ($\theta_{neutral}$) of 0 rad. The extended virtual length setpoint enabled the robot to absorb impact upon landing without inflicting damage on the system.

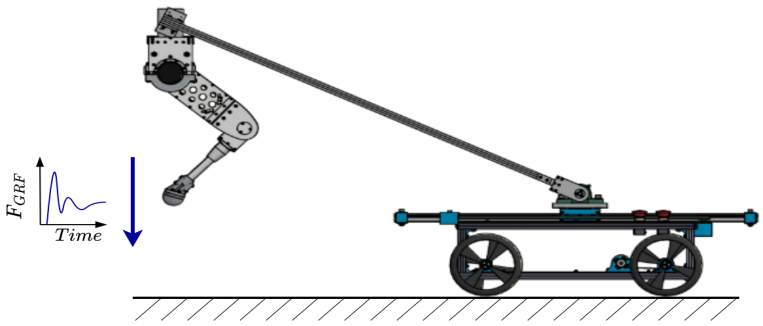

Figure 7.4: An illustration of the virtual compliant drop test scenario showing the suspended robot before being dropped to examine ground contact behaviour.

The proprioceptive force feedback was determined through multiplying the inverse Jacobian transpose of the robots forward kinematics by the internal torque feedback produced by the CubeMars AK70-10 motors, as detailed in Equation 2.1. This allowed

the robot to actively emulate the ground reaction force (GRF) experienced by the legs and was compared to the actual force captured by the pressure sensor molding inside the robots feet. A distinct correlation emerged between the proprioceptive feedback and the sensor data shown in Figure 7.5.

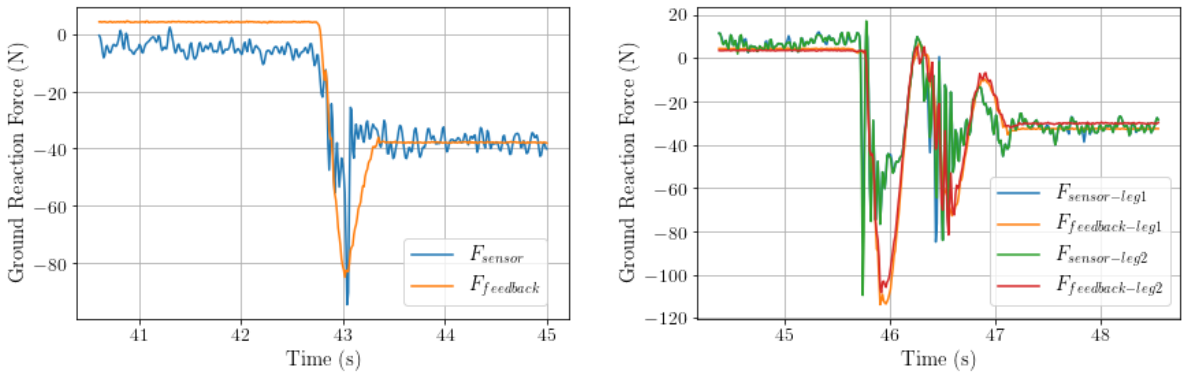

(a) Monopod Force Transparency **(b)** Biped Force Transparency

Figure 7.5: A comparison between the proprioceptive feedback produced by the motors and the pressure sensor molded in the feet of the robot to validate the accuracy of the force transparency.

The displayed pressure sensor data was passed through a low pass filter to reduce error spikes within the captured readings without altering the characteristics of the data. Notably, the proprioceptive feedback for the monopod robot accurately aligned with the pressure sensor reading and settled at roughly 40 N, which directly corresponded to the weight of the system. Whereas, the pressure sensor data captured for the bipedal drop test momentarily spiked to the peak proprioceptive force before exhibiting a 30 N error in amplitude. However, as the bipedal robot oscillated and settled, the force feedback was observed to align with the pressure sensor reading with minimal error. The discrepancy experienced between the two data sets either occurred as a result of the silicone rubber foot partially dampening the impact before reaching the pressure module or due to a misaligned contact angle of the foot. Despite this discrepancy, the low cost pressure sensor validated the suitable accuracy of the force transparency, which was solely used throughout subsequent experiments.

Following the validation of the systems force transparency, successive drop tests were performed on both robots to examine the landing behaviour of the system to identify compliant spring constants for the hopping controller detailed in Table 6.1. Throughout the conducted drop tests shown in Figure 7.6, lower spring constants were observed to produce compliant landing and exhibit reduced ground reaction forces for both robots. However, the monopod experienced non-compliant landing for spring constants above 1200 N/m and above 1000 N/m for the biped. This would cause the robots to break contact

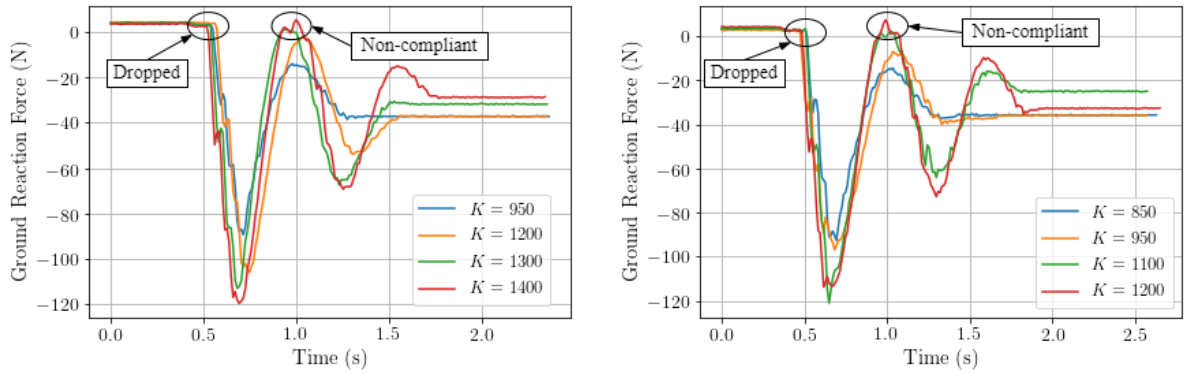

(a) Monopod Drop Test **(b)** Biped Drop Test

Figure 7.6: The compliant drop test results for the developed platforms using a constant damping coefficient of $C_l = 55$ Ns/m. Additionally, spring constants producing non-compliant behaviour due to double contact motion upon impact are identified.

with the ground upon landing and evidently create a double contact motion before settling on the ground. Therefore, spring constants below 1000 N/m were considered suitable for flight and landing maneuvers in the hopping control sequence. Furthermore, analyzing the produced contact forces, an average ground reaction force of 2.62 times the weight of a single leg was obtained.

7.2. Vertical Specific Agility

To assess the agility of the developed robots, a performance metric introduced by Duperret [97] known as vertical specific agility was identified to enable a comparison of leaping-from-rest transitions between robots of different scales and morphologies. Similarly to the explosive agility characteristic exhibited in animal mobility, research has shown high vertical agility to be a fundamental characteristic in producing rapid transient motions in legged robots [97, 98]. Vertical specific agility is defined as the mass normalized change in extrinsic body energy during stance, motivated by tasks involving significant vertical ascent [5, 43]. The vertical specific agility performance metric (α_v) is determined as follows:

$$\alpha_v = h_{max} g. \tag{7.1}$$

Where the maximum experimental jumping height of the robot is denoted by h_{max} and g represents the gravitational acceleration. Additionally, vertical specific agility assumes horizontal translational and rotational quantities to be negligible, as the friction experienced between the foot and ground to generate forward planar agility is unrelated to the power of the system [8]. Therefore, single hop tests were conducted in this section to determine the vertical specific agility performance of the developed robots in comparison to existing platforms.

7.2.1. Single Hop Test

The conducted single hop test served two main purposes in justifying the performance of the robots. Firstly, as mentioned above, a leaping-from-rest transition such as a hop test is used as a measurement in quantifying the vertical agility of a robot. In addition, the executed single hop test was used to validate the incremental analytical analysis detailed in Chapter 4, which utilized the maximum jumping height as a performance metric in the design of robot. For the conducted hop tests, the robots' embodied the virtual model control template described in Section 6.2 and 6.3, and involved configuring the robots' in an initial stance position before activating the thrust phase of the hopping sequence. Images of the robots performing the hop test can be seen in Figure 7.7, which illustrates the motion of system from stance to the apex of the maneuver.

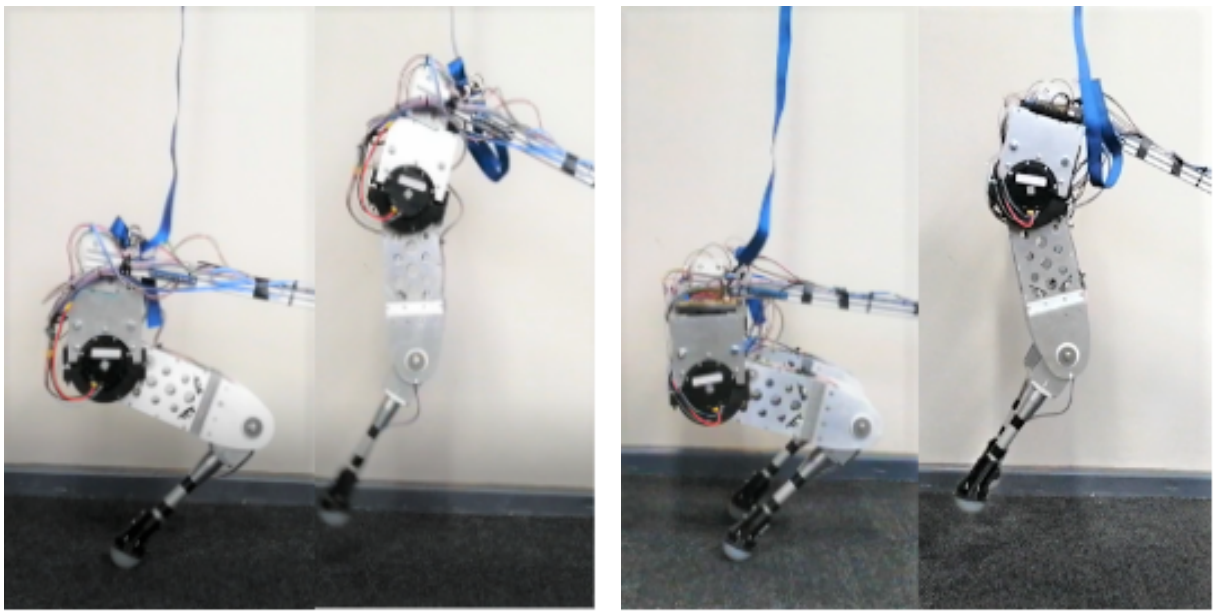

(a) Monopod Single Hop **(b)** Biped Single Hop

Figure 7.7: The monopod and biped robots performing maximum single hop vertical agility tests while constrained in the sagittal plane by the vertical planarizing cart system. The snapshots taken of this test shows the transition of the robot from its initial stance position to the apex height of the maneuver.

Multiple single hop tests were conducted for both systems using a thrust force of 250 N and produced an average virtual take-off length of 0.49 m, which corresponded to a maximum analytical jumping height of 0.78 m. Observing the height of the three superimposed single hop tests shown in Figure 7.8, it is clear that both the monopod and biped platforms were capable of producing the analytical designed height of the robot. As the monopod and biped robots respectively achieved maximum leaping heights of 0.784 m and 0.81 m, evidently validating the accuracy of the analytical design approach. However, comparing the height trajectory of the two robots it can be seen that the biped experiences a larger oscillation upon impact before settling

due to the increased weight of the robot. Although, this matches the experienced behaviour observed between the two robots during the preliminary disturbance and drop tests.

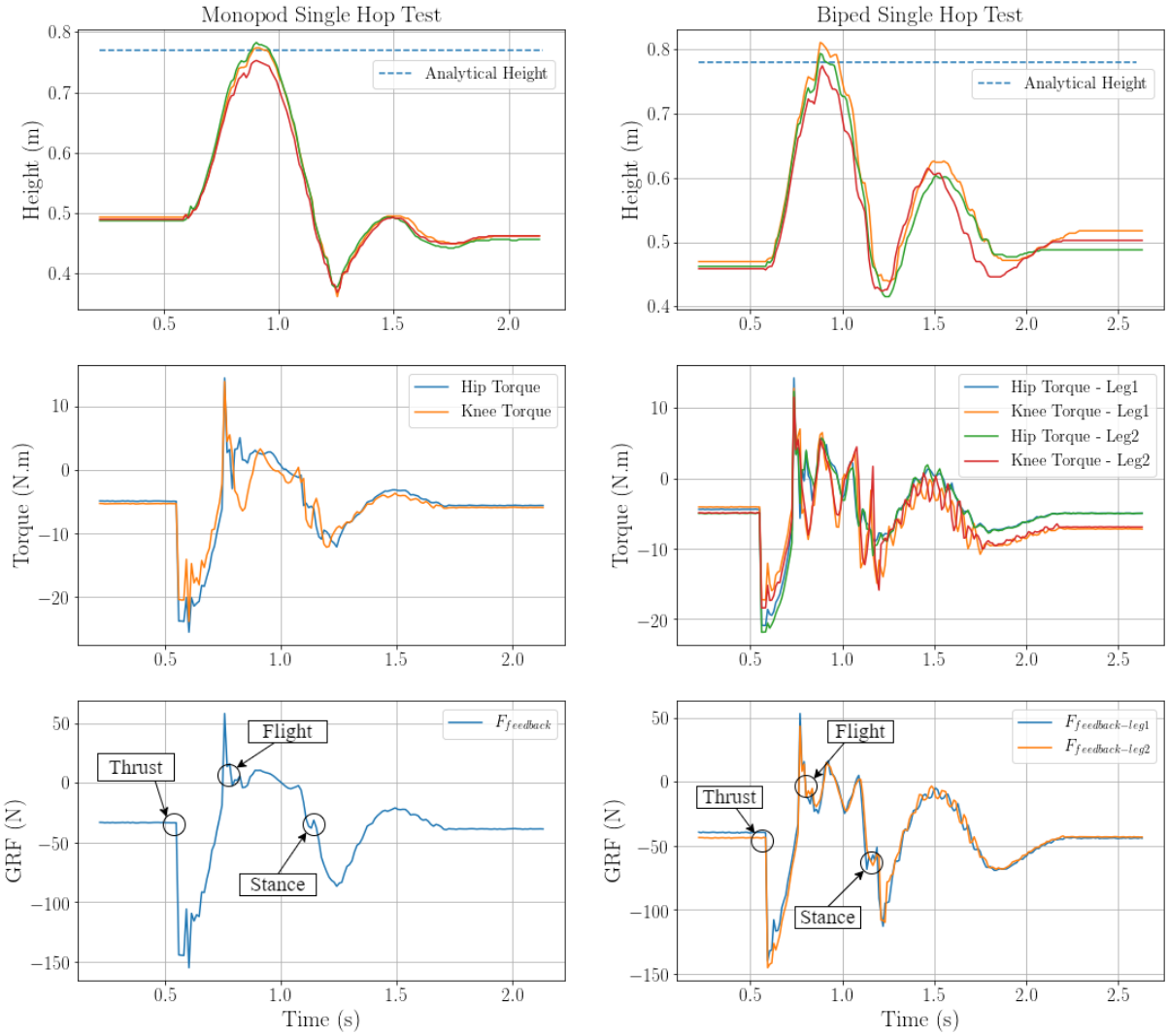

(a) Monopod Single Hop Data **(b)** Biped Single Hop Data

Figure 7.8: The single hop test data produced by the developed robots comparing the maximum leaping height of three successive tests utilizing a 250 N thrust force against the analytical height. Furthermore, the produced motor torques and labelled ground reaction force of the maneuver is shown, identifying the activated control states at their respective time intervals.

Observing the produced motor torques shown in Figure 7.8, it was noted that the physical robot produced better performance in comparison to the analytical model. Despite minor height differences between the models, the physical robots observed a maximum motor torque output of 20.67 N.m, which corresponded to 83.3% of the maximum available torque capacity. Whereas the analytical design analysis of the robot assumed a torque saturation limit of 95%. Therefore, with a slightly increased thrust force the physical robots could exceed the analytical jumping height. However, this was avoided to mitigate

possible damage to the system as the produced leaping height was deemed sufficient to validate the robots dynamic properties. Furthermore, the compliant landing of the robots can be seen in the ground reaction force plot of the maneuver along with identified control states. Note, the ground reaction force spikes to approximately 50 N upon flight due to the repositioning of the foot as the orientation of the robot dynamically changes with the radius of curvature of the boom arm.

Vertical Specific Agility Results

Using the maximum change in jumping height and Equation 7.1, the vertical specific agility for the monopod and biped robots were calculated to be 2.84 $(m/s)^2$ and 3.34 $(m/s)^2$ respectively. The increased agility exhibited by the biped in comparison to the monopod resulted due to the reduction in additional boom weight per leg, along with the systems doubled mass and power provided by the second leg of the robot.

Table 7.1: Vertical specific agility performance comparison of existing dynamic legged robot containing different physical features and properties. The physical properties, specifications and performance metrics of Q-Bert are added to the table to evaluate the the systems vertical agility performance. Note, the leg length and max height detailed below refers to the mean virtual leg length and maximum change in jumping height. The data shown in this table is adapted from [3, 5, 8].

Robot	No. Legs	Gear Ratio	DoF	Leg Length m	Body Mass kg	Motor Mass %	Max. Height m	α_v $(m/s)^2$
Q-Bert Mono	1	10	2	0.32	4.096	25.44	0.29	2.84
Q-Bert Bi	2	10	4	0.32	8.91	23.39	0.34	3.34
Minitaur	4	1	8	0.2	5	40	0.48	4.71
Baleka	2	7	4	0.5	15.62	22.37	0.92	9.03
Delta Hopper	1	1	3	0.2	2	38	0.35	3.44
GOAT	1	1	3	0.26	2.5	25.20	0.82	8.04
Jerbora	2	1	4	0.105	2.5	40	0.14	1.37
MIT Cheetah	4	5.8	12	0.275	33	24	0.5	4.91
StarlETH	4	100	12	0.2	23	16	0.32	3.09
Cheetah Cub	4	300	8	0.069	1	16	0.02	0.20
ATRIAS	2	50	6	0.42	60	11	0.11	1.08

Table 7.1 presents a comparison of Q-Bert against the physical properties and specifications of existing robotic platforms including vertical agility. From this comparison it is clear to see that Q-Bert, in both the monopod and biped formats, outperforms some of the existing dynamic robots and is placed within a competitive region amongst existing dynamic legged robots. Notably, the monopod version of Q-Bert was capable of surpassing the agility produced by bipedal robots such as Jerbora (1.37 $(m/s)^2$) and ATRIAS (1.08 $(m/s)^2$); whereas the bipedal version of Q-Bert approximately tripled the agility seen in these robots. Unfortunately, Q-Bert failed to compete with the most agile developed robots

being Baleka and GOAT, producing phenomenal vertical specific agility performances of 9.03 $(m/s)^2$ and 8.04 $(m/s)^2$ respectively. However, upon further inspection of Baleka's vertical agility it was noted that the robot produced a torque output 2.77 times greater than Q-Bert, hence the drastic difference in agility [8]. Furthermore, unlike Q-Bert, GOAT does not accommodate on-board electronics which provides the robot with an unfair advantages as it mitigates the impedance contributed by additional system mass.

7.2.2. Virtual Model Control Performance

The behaviour and robustness of the virtual model control template is a pivotal aspect in attaining continuous dynamic locomotion. Therefore, the single hop test served as a method for evaluating the performance and expected behaviour of the control algorithm during the state transitions of a single trajectory from start-to-end. The regulated virtual length and angle control states of the respective platforms for a single hop test are shown below in Figure 7.9.

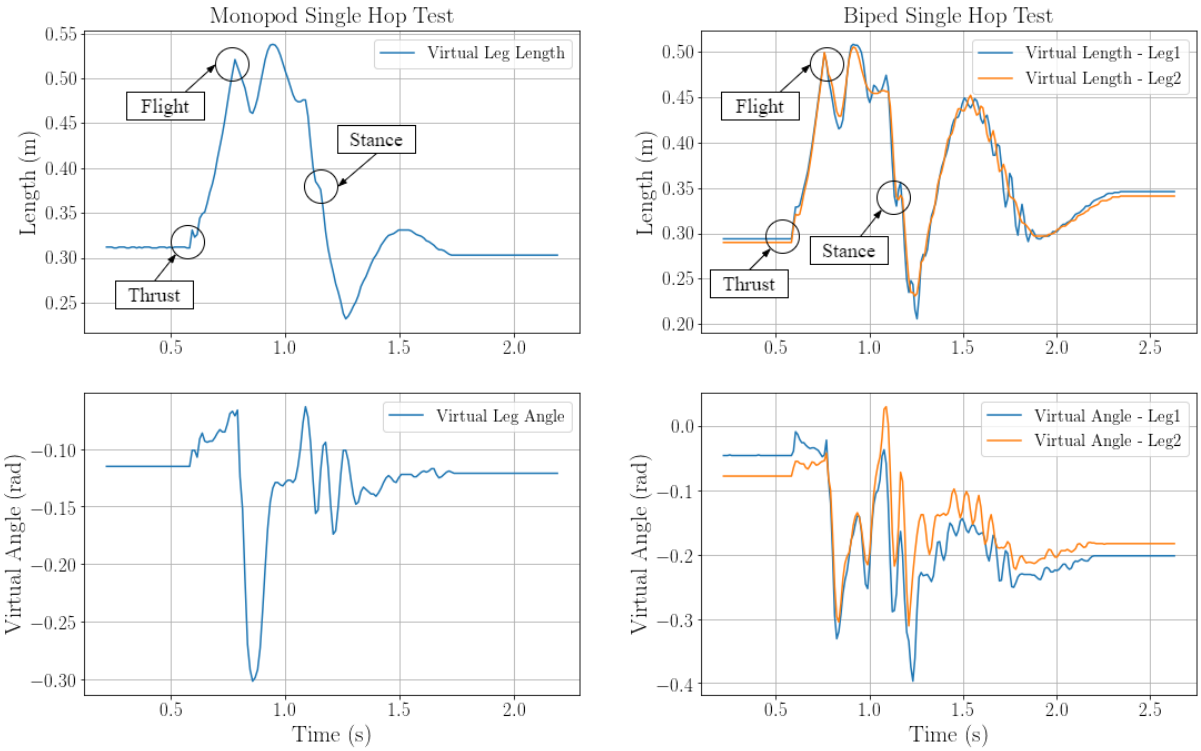

(a) Monopod Control States

(b) Biped Control States

Figure 7.9: An evaluation of the virtual model control performance in regulating the virtual length and angle setpoints of the system. Note the oscillation shown in the virtual length and angle upon lift-off due to the repositioning of the foot during flight.

Analyzing the monopod control data shown in Figure 7.9a, revealed oscillations in both the virtual length and angle upon lift-off and proceeded to stabilize upon landing. The data indicated a rather smooth transition with the minor oscillations occurring after the

initial take-off point, which caused the virtual angle to spike to −0.3 rad. Notably, both the virtual length and angle settled at the initial starting values, while minor deviations from the virtual angle setpoint of 0 rad occurred due to human error when placing the robot on the ground before executing the maneuver.

Similarly, analyzing the biped control data shown in Figure 7.9b, revealed oscillatory behaviour upon take-off and stabilization upon landing as seen in the monopod test. However, the virtual angle experienced increased oscillations and completed the trajectory with the foot slightly in front of the robot. This was seen by the deviation in the final virtual length and angle of the robot compared to the initial value. The increased oscillations experienced during flight in the biped were due to the legs counter balancing the motion of repositioning the feet of the robot. In light of these oscillations, the controller presented adequate robustness as it prevented the system from instability when presented with minor discrepancies or perturbations.

7.3. Periodic Hopping Maneuvers

To verify the dynamic performance of the robot for transient maneuvers involving rapid acceleration, the robot was subjected to continuous vertical hopping tests while embodying the virtual model control hopping sequence detailed in Section 6.3.2. The generated periodic trajectories of the developed robots were then compared to the trajectory optimisation simulation of the SLIP model detailed in Section 3.4. The generated trajectory simulation enabled the robotic locomotion to be compared to a predetermined desired motion based on the thrust force of the robot. Effectively, assisting in verifying the dynamic performance of the robots by emulating the desired transient maneuvers through simulation, which implemented the hardware characteristics of the physical robot as systematic bounds and constraints. Additionally, Raibert's hopping height controller emerged from the trajectory optimisation simulation, which motivated the implementation of the virtual model control template. Consequently, the vertical constraint of the robot's periodic motion mitigated the implementation of Raibert's attitude and forward velocity controllers in the virtual model controller, due to a net zero forward thrust applied on the robot.

The continuous hopping maneuvers generated through the trajectory optimisation simulation comprised of three separate trajectories phases (acceleration, steady-state and deceleration) used to emulate the initial accelerating hop up, continuous hopping and decelerating landing motions. These individual trajectory phases were processed and stitched together post-simulation to form a long-time-horizon trajectory which began and ended with the robot in a rest position. Table 7.2 indicates the number of variable

time-step nodes used to regulate the simulation time of each of the trajectories to achieve the desired motions displayed throughout this section.

Table 7.2: The variable time-step nodes used to regulate the simulation time of the generated trajectories for the developed robots.

	Number of Nodes		
Robot Trajectory	Acceleration	Steady-State	Deceleration
Monopod	30	50	70
Biped	30	50	50

7.3.1. Monopod Continuous Hopping

Vertical continuous hopping was conducted on the monopod using a thrust force of 150 N and was compared to the simulated trajectory as shown in Figure 7.10 and 7.11. Through analyzing the hopping height and vertical velocity graphs of the physical robot trajectory in Figure 7.10, it can be seen that the robot achieved a steady-state hopping height of 0.7264 m at a hopping frequency of 1.715 Hz. Additionally, the monopod produced a vertical hopping velocity of 1.73 m/s throughout the executed periodic maneuver.

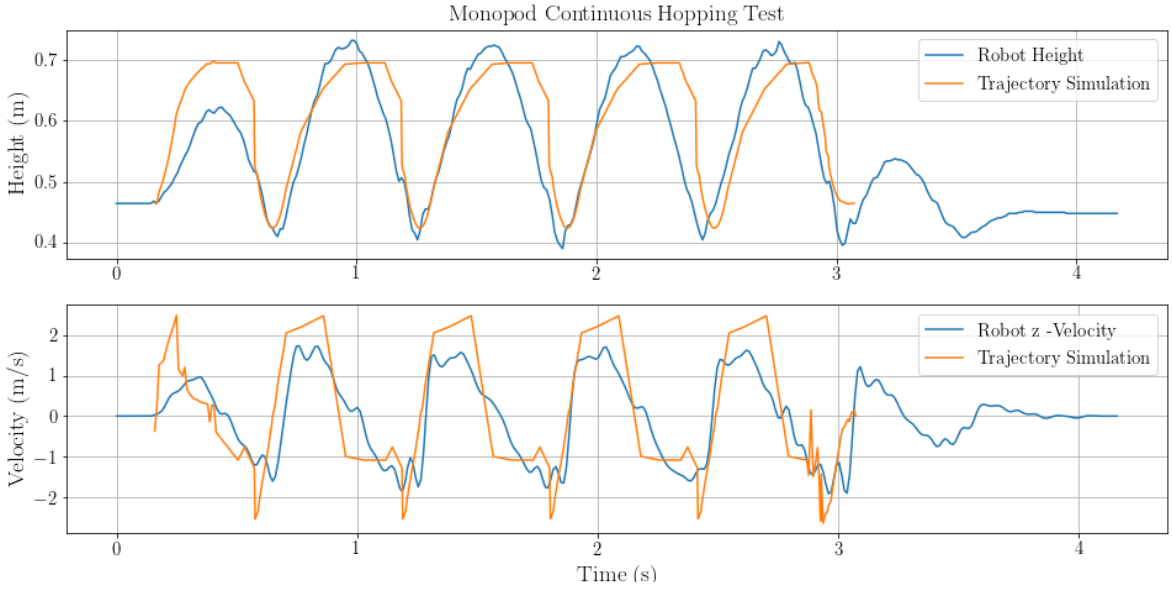

Figure 7.10: The monopod continuously hopping using a thrust force of 150 N with the top graph showing the body height of the robot against the simulated trajectory. Whereas the lower graph shows the vertical hopping velocity of the robot against the simulated trajectory result. Note the discrepancy between the two models on the first hop due to the robot overcoming static joint friction before achieving steady-state motion.

The hopping height and vertical velocity of the robot was seen to align with the simulated trajectory data, with the only discrepancy being the apex height of the first hop. This discrepancy occurs due to the static joint friction experienced by the robot in the resting position of the initial hop. Furthermore, the simulated trajectory does not

account for the oscillation seen by the physical robot during landing, as the optimizer was setup to complete the trajectory once the body velocity of the decelerating hop reached zero. However, the initial drop tests performed in Section 7.1.3 provided assurance that the robot would land compliantly.

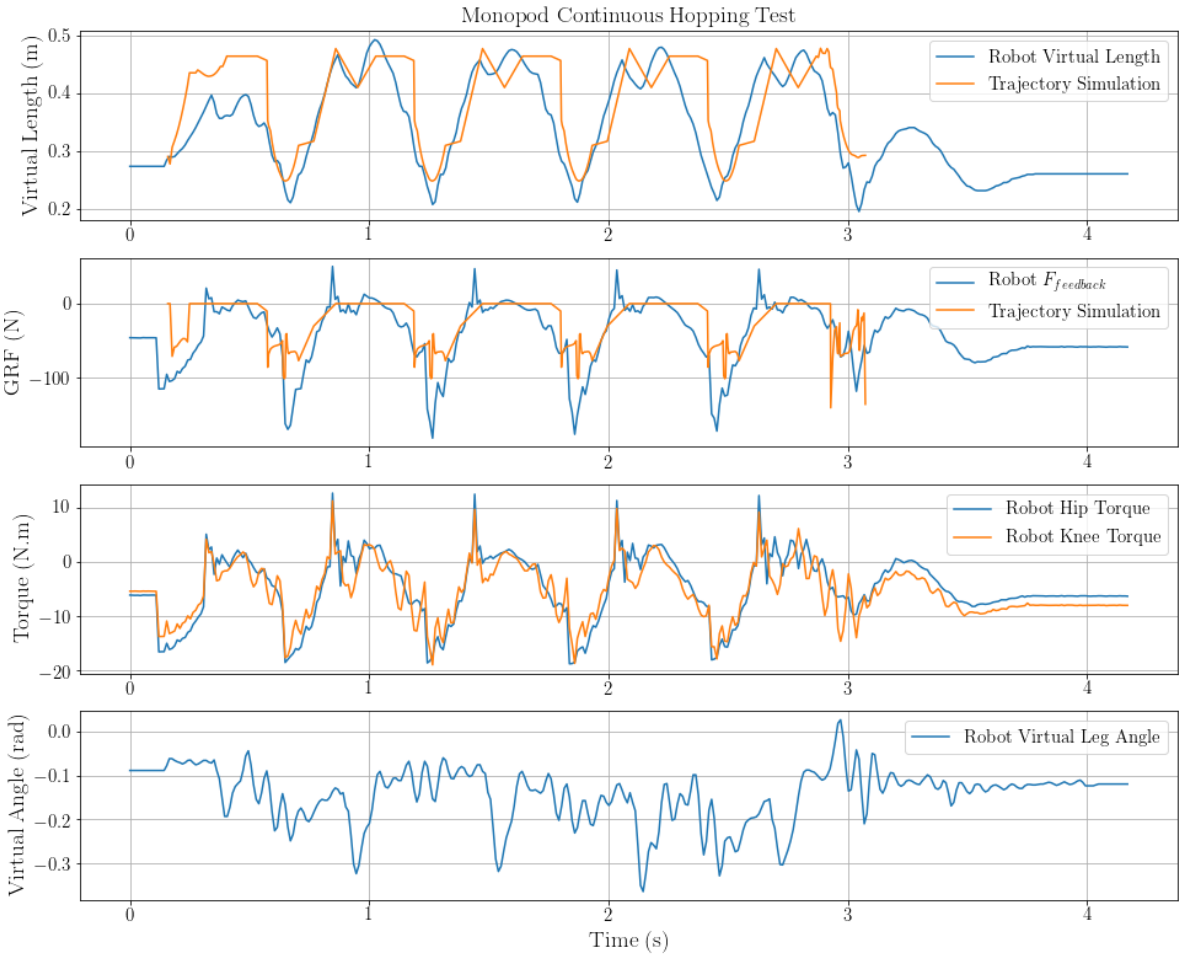

Figure 7.11: The monopod continuous hopping data showing (from top to bottom) the virtual leg length and ground reaction force graphs of the robot against the simulated trajectory. Followed by the motor torques and virtual angle data of the executed hopping maneuver.

The monopod results shown in Figure 7.11 display the virtual leg length and ground reaction force of the robot compared to the simulated trajectory results, followed by the motor torques and virtual leg angle of the robot. A distinct similarity between the two data sets emerged for the virtual leg length comparison, as the both the physical robot and simulated result presented minor oscillations at the apex of the trajectory; resembling the repositioning of the foot upon flight. Evidently, the comparison between the physical model and simulated results revealed that Q-Bert required a single hop to generate sufficient acceleration to achieve and maintain steady-state motion. With the exception of minor error observed in the ground reaction force comparison between the robot and simplified model used to simulate the trajectories; however, both results experienced similar behaviour

in terms of ground contact timing. Furthermore, the presented motor torques indicated a maximum produced torque of 17.892 N.m, which corresponded to 72.15 % of the maximum operating torque. Additionally, the virtual leg angle indicated that the periodic hopping maneuver started and ended in the same orientation and verified the robustness of the virtual model control template for accelerating periodic motions.

7.3.2. Biped Continuous Hopping

Vertical continuous hopping tests were conducted on the biped using a thrust force of 120 N and were compared to the simulated trajectory data as shown in Figure 7.12 and 7.13. Through analyzing the hopping height comparison graph shown in Figure 7.12, it can be seen that the biped achieved a steady-state hopping height of 0.665 m at a hopping frequency of 1.976 Hz. However, unlike the monopod, steady-state motion was only achieved from the third hop as seen by the discrepancy between the height of the physical robot and simulated trajectory for the first two hops.

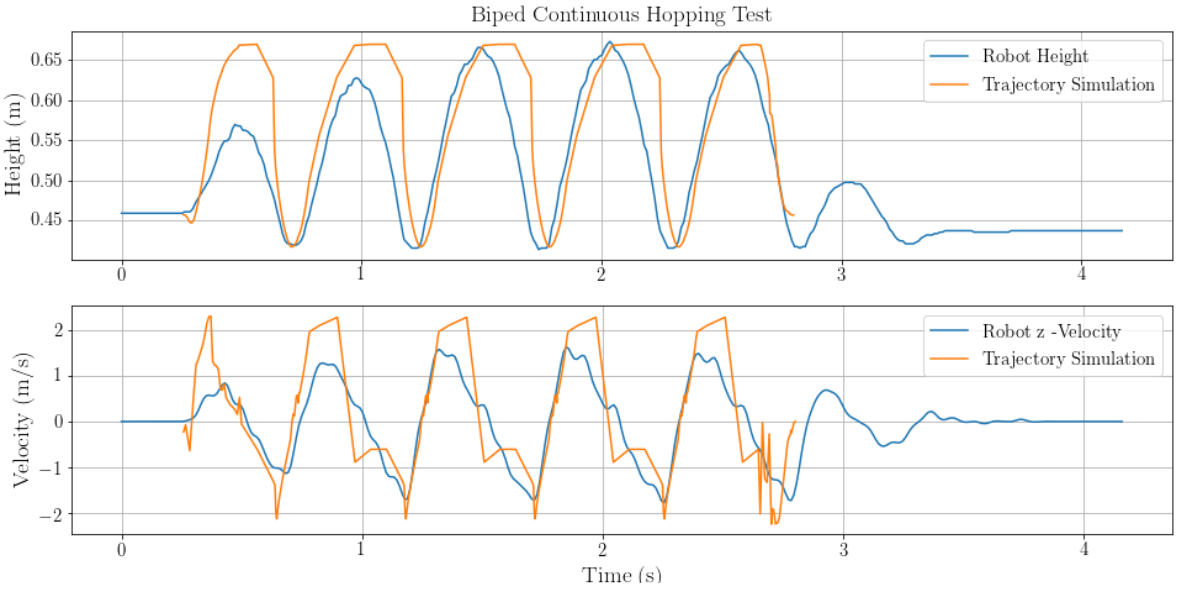

Figure 7.12: The biped continuously hopping using a thrust force of 120 N with a top graph showing the body height of the robot against the simulated trajectory. The lower graph shows the vertical hopping height of the robot against the simulated trajectory result. Note the discrepancy between the two models for the first two hops before achieving steady-state motion.

Similarly to the monopod, the robot was required to overcome static joint friction on the first hop and evidently resulted in an error between the actual and desired trajectories. Although in the case of the biped, due to the power supply issues encountered during periodic hopping tests as mentioned in Section 5.3.1, a lower thrust force was applied in order to sustain periodic motion. Consequently, this decrease in thrust force ultimately required the system to generated sufficient acceleration over two hops to achieve and maintain steady-state motion. Additionally, the biped produced a steady-state vertical

hopping velocity of 1.69 m/s, which gradually increased over the first two hops until steady-state motion was attained.

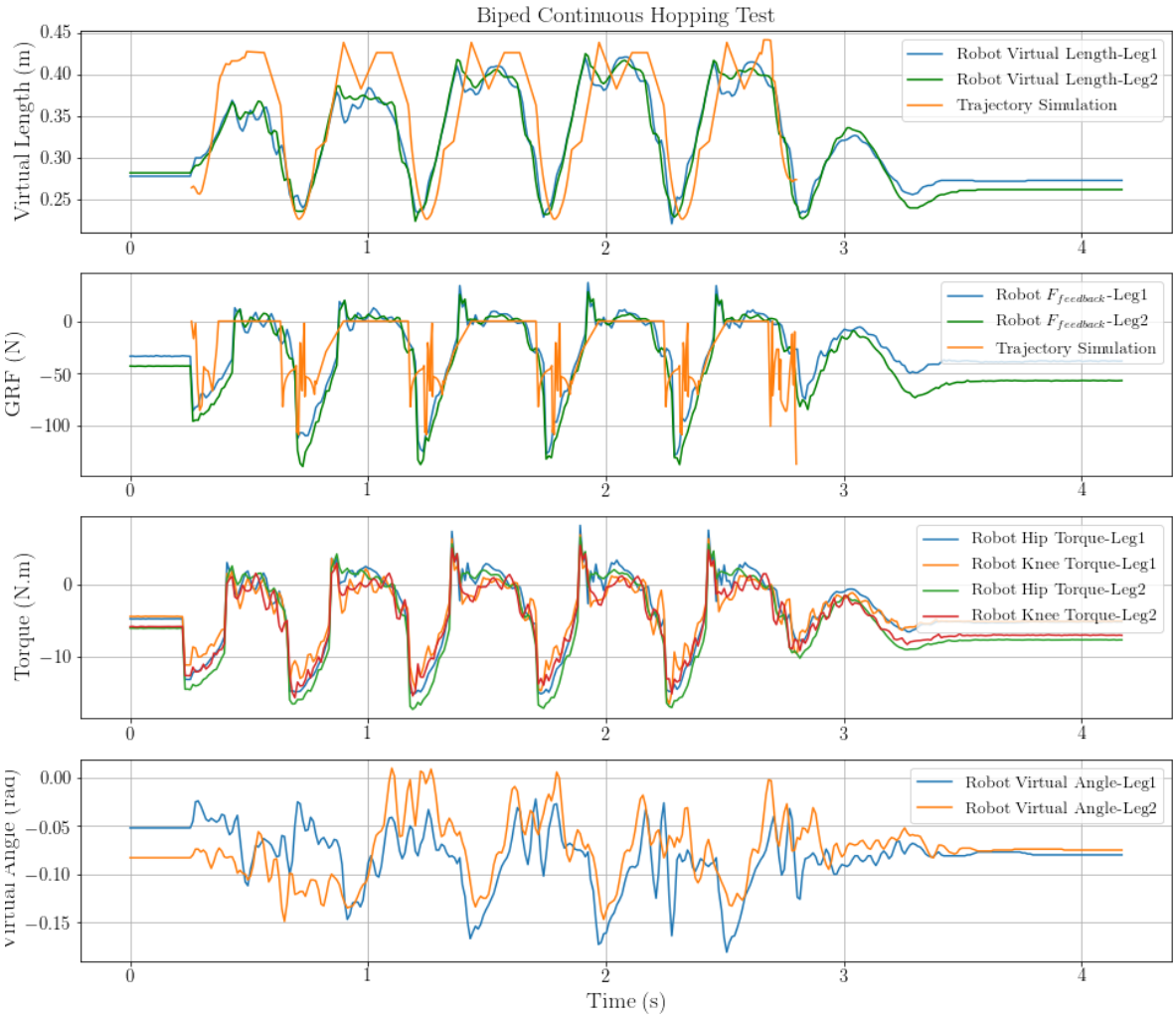

Figure 7.13: The biped continuous hopping data showing (from top to bottom) the virtual leg length and ground reaction force results of the robot against the simulated trajectory. Followed by the motor torques and virtual angle of the executed hopping maneuver.

The biped results shown in Figure 7.13 display the virtual leg length and ground reaction force of the robot compared to the simulated trajectory, followed by the motor torque and virtual angle of the legs. Similarly to the monopod, the virtual leg lengths of the biped presented similar behaviour and motion in comparison to the simulated trajectory with both data sets producing minor oscillations at the apex; while re-positioning the foot during flight. Additionally, the magnitude of the ground reaction forces determined through proprioceptive force feedback was seen to align with the simulated trajectory result. Although, it was noted that the simulated ground reaction force revealed abrupt ground contact between hops, which indicated each steady-state landing was on the verge of non-compliance. However, this was not experienced during physical system testing.

Furthermore, the presented motor torques indicated a maximum produced torque of 15.719 N.m, which corresponded to 63.38 % of the maximum operating torque. Lastly, Q-Bert's control stability can be seen through the minor deviations in the virtual leg angle, as the legs fluctuated within 0.1 rad of the initial resting position.

Bipedal Thrust Comparison

A continuous hopping comparison using different thrust forces was performed to explore the accelerating behaviour of the robot at increased hopping heights. This comparison, as shown by the graphs in Figure 7.14, involved comparing the hopping height of the biped for thrust forces of 120 N and 180 N, along with examining the behaviour of the virtual leg length and angle to evaluate the controller performance. Notably, the 180 N continuous hopping test was limited to three hops as power supply OVP problems were encountered as discussed in Section 5.3.1.

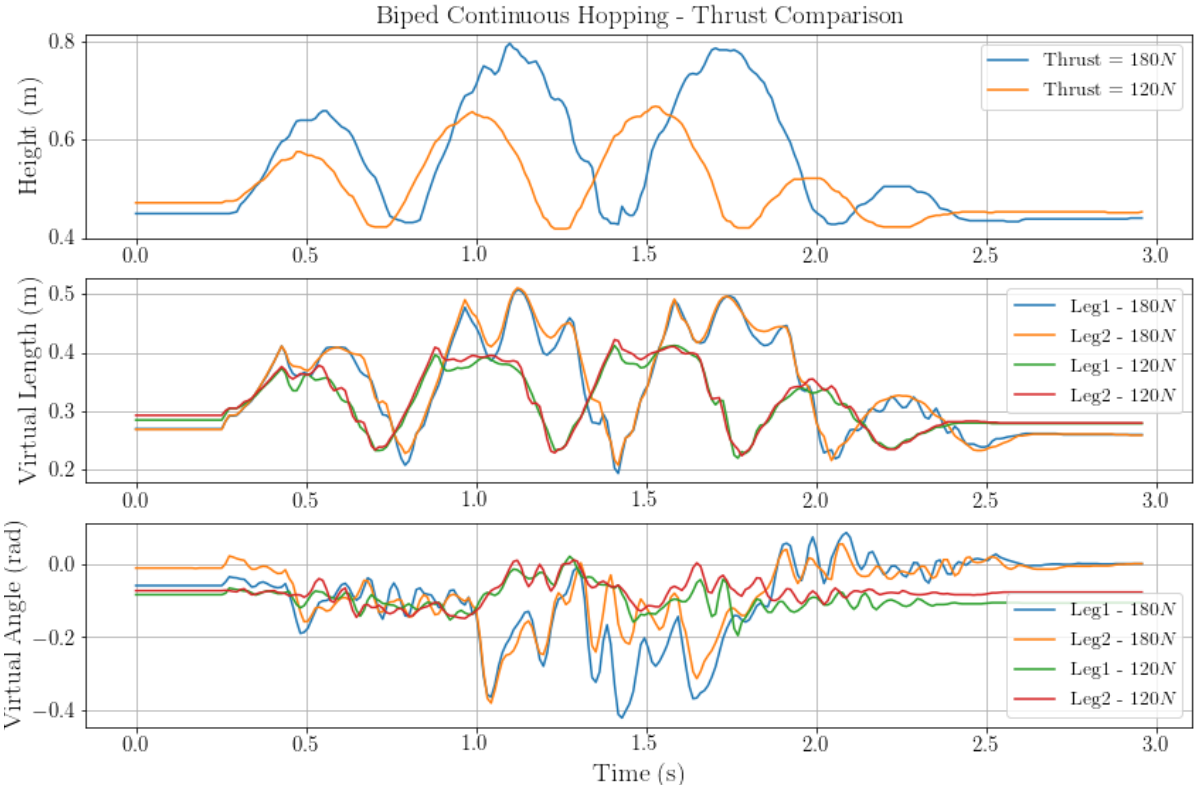

Figure 7.14: A data comparison of different thrust force implemented on the biped during the continuous hopping maneuvers. The compared data (from top to bottom) includes the body height, virtual length and virtual angle of the robot for a thrust force of 180 N and 120 N.

Examining the compared results shown in Figure 7.14, it was clear that Q-Bert was capable of attaining a steady-state hopping height of 0.8 m at a hopping frequency of 1.653 Hz through a thrust force of 180 N. Which was near the maximum height of 0.81 m observed in the single hop test. Whereas, a thrust force of 120 N produced a lower hopping height of 0.665 m at an increased hopping frequency of 1.976 Hz. Upon

analyzing the virtual length and angle of the system, a distinguishable difference could be seen between the two data sets as the thrust force of 180 N produced larger oscillations during flight. However, the thrust force of 120 N presented stable behaviour with subtle deviations from the original virtual angle of the leg, while a smooth transition between the stance and flight states could be seen in the virtual length data.

Although Q-Bert was capable of performing steady-state continuous hopping maneuvers at a thrust force of 180 N, due to the OVP power supply problems encountered and the exhibited oscillations in state transitioning; this was not sustainable for prolonged periods of time. However, with an alternative power source and minor controller adjustments, better performance can be emulated at these higher thrust forces. Additionally, this comparison concluded that the implemented virtual model controller provided robust and stable motions through state transitioning for lower thrust forces.

7.4. Summary

This chapter validated the desired purpose and outcome of this thesis to develop a series articulated bipedal robot capable of agile and transient maneuvers. This was done by evaluating the dynamic performance and behaviour of the robot through various conducted experiments. This chapter provided an initial discussion on the calibration and initialization process of the system. Which displayed the robot in the calibrated orientation while attached to the vertical planarizing cart system; constraining the robot in the sagittal plane. Thereafter, the initial disturbance and drop tests performed on Q-Bert were detailed and verified the proprioceptive force sensing of the system. These initial experiments revealed the behaviour of the virtual model controller for the respective robots, allowing the author to identify regions of non-compliant motion based on the spring constants and damping coefficients implemented by the controller.

This was followed by a vertical specific agility analysis to compare the agility performance of Q-Bert to existing dynamic legged robots. This was conducted in the form of single hop tests, which noted a maximum hopping height of 0.784 m and 0.81 m for the monopod and biped, respectively. This validated the design analysis of Q-Bert by surpassing the analytically determined jumping height. Additionally, these jumping heights resulted to a vertical specific agility of 2.84 $(m/s)^2$ and 3.34 $(m/s)^2$ for the monopod and biped, respectively and surpassed the agility embodied by bipedal robots such as ATRIAS and Jerbora. Thereafter, vertical continuous hopping maneuvers were conducted and compared to the trajectory optimisation simulation to verify the accelerating capabilities of the robot for transient maneuvers. Lastly, a thrust comparison was presented to observe the distinguishable differences in Q-Bert's control behaviour for different thrust forces.

Chapter 8

Conclusion and Future Works

The main focus of this project was to design and develop a series articulated bipedal robot, given the name Q-Bert, to perform transient and agile maneuvers. In achieving this goal, Q-Bert has provided a platform for future students within the ESL at Stellenbosch University to explore the effective compliance of the platform on rugged terrain beyond the confinement of a laboratory environment. While also allowing student to explore different control techniques and develop novel control algorithms. Furthermore, throughout the iterative and detailed design process of the robot, including the development of the hardware, software and artificial restraint systems; the five objectives outlined in Chapter 1 of this thesis were satisfied. The accomplishment of these objectives will be elaborated on throughout this chapter by summarizing the work conducted in this research.

8.1. Summary and Conclusion

Over the past few decades, literature has shown legged locomotion to be a superior and growing field of research within the robotics community due to the ability of these platforms to climb over obstacles and overcome topographic terrain discontinuities. While in recent years, the commercialization of quadrupedal robots has emerged to assist with tasks such as research and rescue operations, remote exploration and navigation through hostile and dangerous environment. Evidently, indicating the profound viability of these robots, along with enhancements in infrastructure to allow dynamic maneuverability.

The literature review presented in Chapter 2, provided the necessary theory and relevant robotic principles to successfully accomplish the research objectives outlined in this thesis. The literature introduced the topic of legged locomotion through a brief discussion on the evolution of legged robotics; which revealed animals and biological mechanisms in nature to be the inspiration behind this form of robotic locomotion. Which has resulted in the development of several existing bio-inspired legged robots, either based on the bio-mimetics of animals or humans, due to their highly dynamic maneuverability and agility. Additionally, the literature study enabled the author to identify key principles for compliant leg design along with desired features for highly dynamic legged robots.

This included robustness, force proprioception and the effects of different actuation and transmission strategies in legged systems. While various artificial restraint systems were presented to support and constrain robots within the sagittal plane without impeding the robots dynamics.

The thesis objective of conducting a trajectory optimisation simulation to verify the dynamic capabilities of the robot was achieved in Chapter 3, while the simulation results were compare to the physical robot in Chapter 7. The developed trajectory optimisation simulation utilized the SLIP model template to embody the dynamics of the system and was implemented in the form of the manipulator equation. Complementarity constraints were employed to enforce contact methods in combination with epsilon relaxation techniques to solve these constraints within an acceptable tolerance. Additionally, the trajectory optimisation simulation was divided into three separate tasks consisting of an acceleration, steady-state and deceleration phase, which were stitched together to form a long-time-horizon trajectory of a periodic planar hopping maneuver.

The incremental analytical analysis developed in Chapter 4, satisfied by the thesis objective of developing a simulation to aid the design process of the robot. The developed analytical analysis was based on a series articulated two link model and analysed the jumping performance of the model for a range of initial orientation conditions, link lengths and different motors. Conclusively, the CubeMars AK10-10 BLDC motor prevailed as the motor to produce the highest jumping performance amongst the examined QDD actuators. Whereas, a conventional link length of 0.27 m was selected to be the most feasible link size for the system. Notably, the selection of the CubeMars AK70-10 modules satisfied the transmission objectives identified in the project requirements. This was accomplished through acquiring a motor capable of providing accurate proprioceptive feedback and low reflected inertia due to the QDD transmission strategy.

The mechanical design objective of this thesis was satisfied through the iterative development phase of the mechanical mechanism prototype presented in Chapter 5. An initial prototype of the robot was design, manufactured and assembled in the form of a monopedal robot to isolate and mitigate any design faults before expanding to the bipedal robot. The mechanical design process placed special focus on minimizing the mass and inertia of the system to reduce the systems mechanical impedance. This was achieved through utilizing aluminium plating containing sectioned cutouts to construct the limbs of the robot along with 3D printed components. Q-Bert recorded a total effective mass of 9.1 kg, which was significantly lower in comparison to existing bipedal robots such as ATRIAS [41] and Baleka [59]. Furthermore, an FEA analysis was performed using Ansys Mechanical to examine the equivalent von-Mises stress and deformation

of the mechanical limbs to verify the structural integrity for a FoS of 2 against the detrimental impact force experienced during landing maneuvers. Additionally, a belt drive transmission with a transmission ratio of 1.25 : 1 was implemented to transfer actuation from the the coaxial motor configuration situated at the hip of the robot to tibia limb.

The defined objective of developing an artificial restraint system to constrain the planar motion of the robot within the saggital plane was addressed within Chapter 5. Through inspiration obtained from existing platforms analyzed in the literature study, a custom planarizing cart system was developed and combined the pivot axis boom arm system and planarizing system into a single concept. The planarizing cart system comprised of a 1.2 m boom arm connected to a pivoting axis situated on the cart system. Due to the time constraints of this thesis, the full functionality of this system was not explored and forms part of the future works section of this thesis.

A simple virtual model controller inspired through Raibert's decoupled parallel hopping control algorithm was implemented in Chapter 6. The virtual mode controller comprised of a sequential state machine to actively transition between the different hopping states, along with an impedance control action based on the SLIP model template and a low-level torque mapping controller. A MATLAB Simulink simulation was conducted to verify and generate the torque mapping control equations. Furthermore, initial complaint disturbance and drop tests were conducted in Chapter 7 and aided in formulating the control parameters required for each of the hopping states. From the single hop and continuous hopping maneuvers executed on the physical robot in Chapter 7, the stability and performance of the controller was examined for various thrust forces. Conclusively, for lower thrust forces the controller displayed robust and stable control of the systems virtual length and angle; whereas for higher thrust forces, oscillations could be observed in the systems virtual length and angle. Subsequently, the controller remained stable throughout the physical experiments and produced robust motion, which satisfied the controller design objectives outlined for this thesis.

The physical experiments conducted in Chapter 7 validated the dynamic capabilities, performance and design process of Q-Bert. The initial complaint drop tests successfully validated the accuracy of the force proprioception by comparing the obtained force feedback to the pressure sensor data captured by the foot of the robot. The design process of the Q-Bert was evaluated through single hop tests, where Q-Bert produced a maximum jumping height of 0.784 m and 0.81 m for the monopod and biped, respectively. Evidently, this surpassed the analytical jumping height of 0.78 m, acquired by the analytical analysis for the relevant take-off leg length. Furthermore, vertical specific agility was selected as a measure of performance to evaluate the agility of the platform and produced a vertical

specific agility of 2.84 $(m/s)^2$ and 3.34$(m/s)^2$ for the monopod and biped, respectively. These results surpassed the vertical specific agility of some existing highly dynamic robots, however Q-Bert was unable to compete with the most agile legged robots. Lastly, the transient capabilities of the Q-Bert were verified by the comparative results shown between the trajectory optimisation simulation and the physical robot. Where the robot effectively produced steady-state continuous hopping to align with the simulation, despite discrepancies involving the first hop of the periodic maneuver.

In conclusion, the accomplishment of the project objectives discussed throughout this chapter shows that the developed platform is indeed agile and capable of performing dynamic, transient maneuvers. Additionally, a repository containing video recordings of the executed hopping maneuvers can be found here.

8.2. Recommendations and Future Works

As the design, fabrication and experimentation of Q-Bert was the first iteration of the bipedal system, several suggestions and future works can be provided to improve the system and explore future research.

Firstly, as Q-Bert operates and performs maneuvers on a more frequent basis; the belt transmission will begin to wear and stretch due to the detrimental ground reaction forces and limited life cycle offered by polyurethane belts. Evidently, this will require constant re-tensioning to maintain a mechanically stiff transmission. Therefore, it is advised to consider replacing the belt and 3D print pulleys with a machined sprocket and chain mechanism in the future.

Notably, the experimental maneuvers conducted within this thesis were limited to periodic hopping due to the time constraint placed on this research. Therefore, alternating hopping maneuvers, along with walking and running maneuvers are yet to be explored and can be conducted on both flat and rough terrain. This would require the support and full functionality of the planarizing cart system; which would require the development and implementation of a position-tracking controller to keep the pivot access centered within the cart.

Lastly, the accuracy of the trajectory optimization simulation can be improved through increasing the dynamic complexity by employing a two-link series articulated model to resemble the robot. This would allow Q-Bert to execute linearized trajectory solutions in an open loop fashion and could be used to develop a gait library of various maneuvers.

Bibliography

[1] M. Silva and J. Tenreiro Machado, "A historical perspective of legged robots," *Journal of Vibration and Control*, vol. 13, p. 1447 – 1486, 09 2007.

[2] S. Rezazadeh, A. Abate, R. L. Hatton, and J. W. Hurst, "Robot leg design: A constructive framework," *IEEE Access*, vol. 6, pp. 54 369–54 387, 2018.

[3] S. Kalouche, "Design for 3d agility and virtual compliance using proprioceptive force control in dynamic legged robots," Master's thesis, Carnegie Mellon University, Pittsburgh, PA, August 2016.

[4] C. Fisher, "Trajectory optimisation inspired design for legged robotics," Ph.D. dissertation, University of Cape Town, 2021.

[5] G. Kenneally, A. De, and D. E. Koditschek, "Design principles for a family of direct-drive legged robots," *IEEE Robotics and Automation Letters*, vol. 1, no. 2, pp. 900–907, 2016.

[6] H.-W. Park, P. M. Wensing, and S. Kim, "Jumping over obstacles with mit cheetah 2," *Robotics and Autonomous Systems*, vol. 136, p. 103703, 2021.

[7] E. Guizzo and E. Ackerman, "74, 500 will fetch you a spot: For the price of a luxury car, you can now buy a very smart, very capable, very yellow robot dog," *IEEE Spectrum*, vol. 57, no. 8, pp. 11–11, 2020.

[8] A. F. Blom, "Design of a bipedal robot for rapid acceleration and braking manoeuvres," Master's thesis, University of Cape Town, 2019.

[9] A. Spielberg, B. Araki, C. Sung, R. Tedrake, and D. Rus, "Functional co-optimization of articulated robots," in *2017 IEEE International Conference on Robotics and Automation (ICRA)*, 2017, pp. 5035–5042.

[10] H. M. M. Ferrolho, "Robustness to external disturbances for legged robots using dynamic trajectory optimisation," Ph.D. dissertation, University of Edinburgh, 2022.

[11] D. Pretorius and C. Fisher, "A novel method for computing the 3d friction cone using complimentary constraints," in *2021 IEEE International Conference on Robotics and Automation (ICRA)*, 2021, pp. 5000–5006.

[12] J. Meyer, "Trajectory optimisation inspired pneumatic locomotion on compliant terrains," Master's thesis, Stellenbosch University, 2022.

[13] Electronic Systems Laboratory. [Online]. Available: https://www.esl.sun.ac.za/

[14] J. Tenreiro Machado and M. Silva, "An overview of legged robots," 04 2006.

[15] P. Billeschou, N. N. Bijma, L. B. Larsen, S. N. Gorb, J. C. Larsen, and P. Manoonpong, "Framework for developing bio-inspired morphologies for walking robots," *Applied Sciences*, vol. 10, no. 19, 2020. [Online]. Available: https://www.mdpi.com/2076-3417/10/19/6986

[16] D. Pretorius, "3d turning analysis of a bipedal robot," Master's thesis, Stellenbosch University, 2022.

[17] A. D. Perkins, "Control of dynamic maneuvers for bipedal robots," Ph.D. dissertation, Stanford University, 2010.

[18] K. R. O'Connor Shawn M., Dawson Terence J. and D. J. Maxwell, "The kangaroo's tail propels and powers pentapedal locomotion," *Biology Letters*, 2014.

[19] "Cheetah chasing a thomson's gazelle." 2018, [Online; accessed October 12, 2022]. [Online]. Available: https://www.reddit.com/r/natureismetal/comments/b52qi7/cheetah_chasing_a_thomsons_gazelle/

[20] K. Houser, "See mit's robot land a perfect backflip - and mangle many others." 2019, [Online; accessed October 12, 2022]. [Online]. Available: https://futurism.com/the-byte/mini-cheetah-backflipping-robot

[21] L. Brassó, B. Béri, and I. Komlosi, "Studies on ostrich (struthio camelus) - review," *Acta Agraria Debreceniensis*, pp. 15–22, 05 2020.

[22] C. Fisher, "State estimation of a cheetah spine and tail using an inertial sensor network," Master's thesis, University of Cape Town, 2015.

[23] V. Shams Esfanabadi, M. Rostami, S. M. Rahmati, J. Baltes, and S. Sadeghnejad, "The average speed of motion and optimal power consumption in biped robots," *The Knowledge Engineering Review*, vol. 34, p. e25, 2019.

[24] "Cassie establishes guinness world record for bipedal robot 100-metre sprint," 2022, [Online; accessed October 12, 2022]. [Online]. Available: https://indianexpress.com/article/technology/science/cassie-bipedal-robot-guinness-world-record-100-metre-sprint-8185835

[25] P. Muench, "Efficiency and speed in legged robots," p. 115, 03 2011.

[26] S. Kim and P. Wensing, "Design of dynamic legged robots," *Foundations and Trends in Robotics*, vol. 5, pp. 117–190, 01 2017.

[27] M. Raibert, *Legged Robots That Balance*. Cambridge, MA: The MIT Press, 1986.

[28] J. Pratt, "Spring flamingo (1996-2000)," [Online; accessed October 13, 2022]. [Online]. Available: http://www.ai.mit.edu/projects/leglab/robots/Spring_Flamingo/Spring_Flamingo.html

[29] M. H. Raibert, "3d one-leg hopper (1983-1984)," [Online; accessed October 13, 2022]. [Online]. Available: http://www.ai.mit.edu/projects/leglab/robots/3D_hopper/3D_hopper.html

[30] C. Chevallereau, G. Abba, Y. Aoustin, F. Plestan, E. Westervelt, C. Canudas-De-Wit, and J. Grizzle, "Rabbit: a testbed for advanced control theory," *IEEE Control Systems Magazine*, vol. 23, no. 5, pp. 57–79, 2003.

[31] M. Hutter, C. Gehring, D. Jud, A. Lauber, C. D. Bellicoso, V. Tsounis, J. Hwangbo, K. Bodie, P. Fankhauser, M. Bloesch, R. Diethelm, S. Bachmann, A. Melzer, and M. Hoepflinger, "Anymal - a highly mobile and dynamic quadrupedal robot," in *2016 IEEE/RSJ International Conference on Intelligent Robots and Systems (IROS)*, 2016, pp. 38–44.

[32] B. G. Katz, "A low cost modular actuator for dynamic robots," Master's thesis, Massachusetts Institute of Technology, June 2018.

[33] G. Bledt, M. J. Powell, B. Katz, J. Di Carlo, P. M. Wensing, and S. Kim, "Mit cheetah 3: Design and control of a robust, dynamic quadruped robot," in *2018 IEEE/RSJ International Conference on Intelligent Robots and Systems (IROS)*, 2018, pp. 2245–2252.

[34] P. M. Wensing, A. Wang, S. Seok, D. Otten, J. Lang, and S. Kim, "Proprioceptive actuator design in the mit cheetah: Impact mitigation and high-bandwidth physical interaction for dynamic legged robots," *IEEE Transactions on Robotics*, vol. 33, no. 3, pp. 509–522, 2017.

[35] S. Seok, A. Wang, D. Otten, and S. Kim, "Actuator design for high force proprioceptive control in fast legged locomotion," in *2012 IEEE/RSJ International Conference on Intelligent Robots and Systems*, 2012, pp. 1970–1975.

[36] P. Holmes, R. J. Full, D. Koditschek, and J. Guckenheimer, "The dynamics of legged locomotion: Models, analyses, and challenges," *SIAM Review*, vol. 48, no. 2, pp. 207–304, 2006.

[37] S. Y. Loo, S. H. Tang, and M. Syamsiah, "Active and passive compliance mechanisms in legged robot locomotion," in *Pertanika Journal of Scholarly Research Reviews*, 2015.

[38] M. A. Jr., W. Wang, R. Loh, and T.-S. Low, "Passive compliance from robot limbs and its usefulness in robotic automation," *Journal of Intelligent and Robotic Systems*, 1997.

[39] R. Blickhan, "The spring-mass model for running and hopping," *Journal of Biomechanics*, vol. 22, no. 11, pp. 1217–1227, 1989.

[40] J. Sensinger and R. Weir, "Design and analysis of a non-backdrivable series elastic actuator," 01 2005, pp. 390 – 393.

[41] C. Hubicki, J. Grimes, M. Jones, D. Renjewski, A. Spröwitz, A. Abate, and J. Hurst, "Atrias: Design and validation of a tether-free 3d-capable spring-mass bipedal robot," *The International Journal of Robotics Research*, vol. 35, no. 12, pp. 1497–1521, 2016.

[42] C. Hubicki, A. Abate, P. Clary, S. Rezazadeh, M. Jones, A. Peekema, J. Van Why, R. Domres, A. Wu, W. Martin, H. Geyer, and J. Hurst, "Walking and running with passive compliance: Lessons from engineering: A live demonstration of the atrias biped," *IEEE Robotics and Automation Magazine*, vol. 25, no. 3, pp. 23–39, 2018.

[43] G. Kenneally, "Design of proprioceptive legged robots," Ph.D. dissertation, University of Pennsylvania, 2021.

[44] J. van Zyl, "Rapid acceleration of legged robots," Master's thesis, University of Cape Town, 2021.

[45] D. Robinson, J. Pratt, D. Paluska, and G. Pratt, "Series elastic actuator development for a biomimetic walking robot," in *1999 IEEE/ASME International Conference on Advanced Intelligent Mechatronics (Cat. No.99TH8399)*, 1999, pp. 561–568.

[46] E. Ackerman, "Ghost robotics' minitaur demonstrates impressive new skills," 2017. [Online]. Available: https://spectrum.ieee.org/ghost-robotics-minitaur-demonstrates-impressive-new-skills

[47] B. T. Knox, "Design of a bipedal robot cable of dynamic maneuvers," Master's thesis, The Ohio State University, 281 W Lane Ave, Columbus, OH 43210, United States, 2008.

[48] J. W. Hurst, "The role an implementation of compliance in legged locomotion," Ph.D. dissertation, Carnegie Mellon University, 2008.

[49] A. Wang and S. Kim, "Directional efficiency in geared transmissions: Characterization of backdrivability towards improved proprioceptive control," in *2015 IEEE International Conference on Robotics and Automation (ICRA)*, 2015, pp. 1055–1062.

[50] H. Asada and K. Youcef-Toumi, *Direct-Drive Robots: Theory and Practice*. The MIT Press, 1987, ch. 1.

[51] A. Singh, N. Kashiri, and N. Tsagarakis, "Design of a quasi-direct-drive actuator for dynamic motions," *Proceedings*, vol. 64, 11 2020.

[52] Y. Yesilevskiy, Z. Gan, and C. D. Remy, "Optimal configuration of series and parallel elasticity in a 2d monoped," in *2016 IEEE International Conference on Robotics and Automation (ICRA)*, 2016, pp. 1360–1365.

[53] M. Hutter, M. Hoepflinger, C. Remy, and R. Siegwart, "Hybrid operational space control for compliant legged systems," 07 2012.

[54] J. Grimes and J. W. Hurst, "The design of atrias 1.0 a unique monopod, hopping robot," 2012.

[55] J. Chen, Z. Liang, Y. Zhu, C. Liu, L. Zhang, L. Hao, and J. Zhao, "Towards the exploitation of physical compliance in segmented and electrically actuated robotic legs: A review focused on elastic mechanisms," *Sensors*, vol. 19, no. 24, 2019. [Online]. Available: https://www.mdpi.com/1424-8220/19/24/5351

[56] J. S. Colett and J. W. Hurst, "Artificial restraint systems for walking and running robots: an overview," *Int. J. Humanoid Robotics*, vol. 9, 2012.

[57] N. Smit-Anseeuw, R. Gleason, P. Zaytsev, and C. David Remy, "Ramone: A planar biped for studying the energetics of gait," in *2017 IEEE/RSJ International Conference on Intelligent Robots and Systems (IROS)*, 2017, pp. 4090–4095.

[58] "Boston dynamics atlas," [Online; accessed October 18, 2022]. [Online]. Available: https://www.bostondynamics.com/atlas

[59] C. Fisher, A. Blom, and A. Patel, "Baleka: A bipedal robot for studying rapid maneuverability," *Frontiers in Mechanical Engineering*, vol. 6, 07 2020.

[60] T. Yang, E. Westervelt, and J. Schmiedeler, "Design and control of a planar bipedal robot ernie with parallel knee compliance," *Autonomous Robots*, vol. 25, p. 317–330, 2008.

[61] S. Seok, A. Wang, M. Y. M. Chuah, D. J. Hyun, J. Lee, D. M. Otten, J. H. Lang, and S. Kim, "Design principles for energy-efficient legged locomotion and implementation

on the mit cheetah robot," *IEEE/ASME Transactions on Mechatronics*, vol. 20, pp. 1117–1129, 2015.

[62] I. Poulakakis and J. Grizzle, "The spring loaded inverted pendulum as the hybrid zero dynamics of an asymmetric hopper," *Automatic Control, IEEE Transactions on*, vol. 54, pp. 1779 – 1793, 09 2009.

[63] B. T. Krupp, "Design and control of a planar robot to study quadrupedal locomotion," Master's thesis, Massachusetts Institute of Technology, 2000.

[64] T. Cnops, Z. Gan, and C. Remy, "The basin of attraction for running robots: Fractals, multistep trajectories, and the choice of control," 09 2015, pp. 1586–1591.

[65] M. Hutter, C. D. Remy, M. A. Höpflinger, and R. Siegwart, "Slip running with an articulated robotic leg," in *2010 IEEE/RSJ International Conference on Intelligent Robots and Systems*, 2010, pp. 4934–4939.

[66] F. Grimminger, T. Flayols, J. Fiene, A. Badri-Spröwitz, L. Righetti, A. Meduri, M. Khadiv, J. Viereck, M. Wuthrich, M. Naveau, V. Berenz, S. Heim, and F. Widmaier, "An open torque-controlled modular robot architecture for legged locomotion research," *IEEE Robotics and Automation Letters*, vol. PP, pp. 1–1, 02 2020.

[67] J. Carius, R. Ranftl, V. Koltun, and M. Hutter, "Trajectory optimization for legged robots with slipping motions," *IEEE Robotics and Automation Letters*, vol. 4, no. 3, pp. 3013–3020, 2019.

[68] E. Almasri and M. Uyguroğlu, "Trajectory optimization in robotic applications: Survey of recent developments," 05 2021.

[69] M. Kelly, "An introduction to trajectory optimization: How to do your own direct collocation," *SIAM Review*, vol. 59, no. 4, pp. 849–904, 2017.

[70] A. W. Winkler, C. D. Bellicoso, M. Hutter, and J. Buchli, "Gait and trajectory optimization for legged systems through phase-based end-effector parameterization," *IEEE Robotics and Automation Letters*, vol. 3, no. 3, pp. 1560–1567, 2018.

[71] C. Fisher, C. Hubicki, and A. Patel, "Do intermediate gaits matter when rapidly accelerating?" *IEEE Robotics and Automation Letters*, vol. 4, no. 4, pp. 3418–3424, 2019.

[72] W. Hart, J.-P. Watson, D. Woodruff, and J.-P. Watson, "Pyomo: Modeling and solving mathematical programs in python," *Mathematical Programming Computation*, vol. 3, pp. 219–260, 09 2011.

[73] A. Patel, S. Shield, S. Kazi, A. Johnson, and L. Biegler, "Contact-implicit trajectory optimization using orthogonal collocation," 09 2018.

[74] L. T. Biegler, "Nonlinear programming - concepts, algorithms, and applications to chemical processes," in *MOS-SIAM Series on Optimization*, 2010.

[75] M. Haberland and S. Kim, "On extracting design principles from biology: Ii. case study-the effect of knee direction on bipedal robot running efficiency." in *Bioinspiration & Biomimetics*, vol. 10, no. 1, 2015.

[76] L. Drnach and Y. Zhao, "Robust trajectory optimization over uncertain terrain with stochastic complementarity," *IEEE Robotics and Automation Letters*, vol. PP, pp. 1–1, 02 2021.

[77] D. R. * and S. J. Wright, "Some properties of regularization and penalization schemes for mpecs," *Optimization Methods and Software*, vol. 19, no. 5, pp. 527–556, 2004.

[78] M. Li, X. Wang, W. Guo, P. Wang, and L. Su, "System design of a cheetah robot toward ultra-high speed," *International Journal of Advanced Robotic Systems*, p. 1, 05 2014.

[79] S. Yu, T.-H. Huang, X. Yang, C. Jiao, J. Yang, Y. Chen, J. Yi, and H. Su, "Quasi-direct drive actuation for a lightweight hip exoskeleton with high backdrivability and high bandwidth," *IEEE/ASME Transactions on Mechatronics*, vol. 25, no. 4, pp. 1794–1802, 2020.

[80] A. Singh, N. Kashiri, and N. Tsagarakis, "Design of a quasi-direct-drive actuator for dynamic motions," *Proceedings*, vol. 64, 11 2020.

[81] B. T. Knox, "Evaluation of a prototype series-compliant hopping leg for biped robot applications," 2007.

[82] K. Byl, M. Byl, M. Rutschmann, B. Satzinger, L. van Blarigan, G. Piovan, and J. Cortell, "Series-elastic actuation prototype for rough terrain hopping," in *2012 IEEE International Conference on Technologies for Practical Robot Applications (TePRA)*, 2012, pp. 103–110.

[83] J. John J. Uiker, G. R. Pennock, and J. E. Shigley, *Theory of Machines and Mechanisms*. Oxford University Press, 2011, ch. 10.

[84] Y. X. Caihua Xiong, Yongan Huang and H. Liu, "Intelligent robotics and applications," in *ICIRA:International Conference on Intelligent Robotics and Applications*, October 2008, p. 157.

[85] T. Yoshikawa, "Manipulability and redundancy control of robotic mechanisms," in *Proceedings. 1985 IEEE International Conference on Robotics and Automation*, vol. 2, 1985, pp. 1004–1009.

[86] J. Martinez, "Manipulability ellipsoids in robotics," February 2022, engineer JAU. [Online]. Available: https://engineerjau.wordpress.com/2013/05/04/advanced-robotics-manipulability-ellipsoids/

[87] M. Azad, J. Babič, and M. Mistry, "Effects of the weighting matrix on dynamic manipulability of robots," *Autonomous Robots*, vol. 43, 10 2019.

[88] Tmotor, The Safer Propulsion System, "Ak series dynamical modular/ak80-6," 2022, [Online; accessed July 5, 2022]. [Online]. Available: https://store.tmotor.com/goods.php?id=981

[89] ——, "Ak series dynamical modular/ak80-9," 2022, [Online; accessed July 5, 2022]. [Online]. Available: https://store.tmotor.com/goods.php?id=982

[90] ——, "Ak series dynamical modular/ak80-9," 2022, [Online; accessed July 5, 2022]. [Online]. Available: https://store.tmotor.com/goods.php?id=1031

[91] J. Driessen and R. Orsolino, "Improving robustness of legged robots against mechanical shock using impulsive dynamics," *Frontiers in Mechanical Engineering*, vol. 6, 01 2021.

[92] Misumi Mech Lab. [Online]. Available: https://us.misumi-ec.com/pdf/tech/mech/US2010_fa_p3513_3534.pdf

[93] "Ansys workbench." [Online]. Available: https://www.ansys.com/

[94] P. Eckert and A. J. Ijspeert, "Adaptive foot design for small quadruped robots," 2016.

[95] A. Spröwitz, A. Tuleu, M. Vespignani, M. Ajallooeian, E. Badri, and A. J. Ijspeert, "Towards dynamic trot gait locomotion: Design, control, and experiments with cheetah-cub, a compliant quadruped robot," *The International Journal of Robotics Research*, vol. 32, pp. 932 – 950, 2013.

[96] J. Pratt, C.-M. Chew, A. Torres, P. Dilworth, and G. Pratt, "Virtual model control: An intuitive approach for bipedal locomotion," *The International Journal of Robotics Research*, vol. 20, pp. 129–143, 2001.

[97] J. Duperret, G. D. Kenneally, J. Pusey, and D. E. Koditschek, "Towards a comparative measure of legged agility," in *ISER*, 2014.

[98] M. M. Plecnik, J. K. Yim, and R. S. Fearing, "Robotic vertical jumping agility via series-elastic power modulation," *Science Robotics*, vol. 1, 2016.

Appendix A

Trajectory Optimisation Formulation

This appendix comprises of the additional details and theory used in the formulation of the trajectory optimisation problem. Various equations and algorithms omitted from the body of this thesis, used to compute the EoM of the simulated SLIP model will be presented throughout this appendix. Furthermore, the exact generalized coordinate bounds implemented during setup of the optimisation environment will be be provided.

A.1. System Kinetic and Potential Energy

Notably, the SLIP model used to represent the robot contained a body and leg mass, along with a leg link moment of inertia (MoI) and centre of mass (CoM). Through the use of the systems generalized coordinates ($\boldsymbol{q}$), the position vector of the leg CoM denoted by $\boldsymbol{P}_{CoM}$ could be defined. Thereafter, the CoM velocity ($\dot{\boldsymbol{P}}_{CoM}$)could be determined using the Jacobian matrix as shown in Equation A.1.

$$\dot{\boldsymbol{P}}_{CoM} = jacobian(\boldsymbol{P}_{CoM}, \boldsymbol{q})\dot{\boldsymbol{q}}. \tag{A.1}$$

Once the position and velocity vectors of the leg CoM were determined the respective potential and kinetic energy of the system could be calculated.

Potential Energy

The potential energy of system denoted by V was determined as follows:

$$V = m_{link} \cdot \boldsymbol{g} \cdot \boldsymbol{P}_{CoM_z} \tag{A.2}$$

Where m_{link} represents the mass of the leg link and $\boldsymbol{g}$ represents the gravitational constant. Notably, in event of a multi-link model, the formula shown in Equation A.2 should sum the energies of the various links to generate the total potential energy of the system.

Kinetic Energy

The total kinetic energy of the system denoted by T_{total}, comprised of both linear (T_{linear}) and rotational ($T_{rotational}$) kinetic energy and was calculated as follows:

$$\begin{aligned} T_{total} &= T_{linear} + T_{rotational}, \\ T_{linear} &= \frac{1}{2} \cdot \boldsymbol{m}_{link} \cdot \dot{\boldsymbol{P}}_{CoM} \cdot \dot{\boldsymbol{P}}_{CoM}^{T}, \\ T_{rotational} &= \frac{1}{2} \cdot \boldsymbol{\omega}_{CoM} \cdot \boldsymbol{J}_{MoI} \cdot \boldsymbol{\omega}_{CoM}{}^{T}. \end{aligned} \tag{A.3}$$

Where $\boldsymbol{\omega}_{CoM}$ denotes the angular velocity of the CoM and $\boldsymbol{J}_{MoI}$ denotes the moment of inertia of the leg link. Similarly to the potential energy, in the event of multiple leg links, the total kinetic energy of the system should consist of the sum of the energy generated by the various links.

A.2. EoM Computation

As mentioned in Section 3.4.1, Euler-Lagrange dynamics were used in form of the manipulator equation as shown in Equation 3.1. Therefore, the computational formulation of each of the matrices involved in the generation of the EoM are provided in this section. The formulation of the Mass matrix ($\boldsymbol{M}(\boldsymbol{q})$) is shown in Equation A.4, whereas the computation of the Coriolis matrix ($\boldsymbol{C}(\boldsymbol{q})$) and Gravitational matrix ($\boldsymbol{G}(\boldsymbol{q})$) are shown in Algorithm 1.1 and 1.2, respectively.

$$\boldsymbol{M} = jacobian(jacobian(T_{total}, \dot{\boldsymbol{q}})', \dot{\boldsymbol{q}}). \tag{A.4}$$

Algorithm 1.1: Formulation of the Coriolis Matrix ($\boldsymbol{C}$) [4, 16].

for $i = 1$: length($\boldsymbol{q}$) **do**
  for $j = 1$: length($\boldsymbol{q}$) **do**
    for $m = 1$: length($\boldsymbol{q}$) **do**
      temp = 0.5(diff($\boldsymbol{M}$(i,j),$\boldsymbol{q}$(m)) + diff($\boldsymbol{M}$(i,m),$\boldsymbol{q}$(j)) - diff($\boldsymbol{M}$(j,m),$\boldsymbol{q}$(i)))$\dot{\boldsymbol{q}}$(m);
      $\boldsymbol{C}$(i,j) = $\boldsymbol{C}$(i,j) + temp;
    end for
  end for
end for

Algorithm 1.2: Formulation of the Gravitational Potential Matrix ($\boldsymbol{G}$) [4, 16].

for $i = 1$: length($\boldsymbol{q}$) **do**
  $\boldsymbol{G}$(i) = diff(V,$\boldsymbol{q}$(i))
end for

Furthermore, the $\boldsymbol{A}$ matrix used to map the external ground reaction forces was calculated using the Jacobian of the foot position ($\boldsymbol{P}_{foot}$) of the leg with respect to the generalized coordinates as follows:

$$\boldsymbol{A} = \sum_{foot} jacobian(\boldsymbol{P}_{foot}, \boldsymbol{q}). \tag{A.5}$$

Lastly, the $\boldsymbol{B}$ matrix used to map the actuator forces and torques to the respective generalized coordinates was calculated through the use of the Jacobian matrix as follows:

$$\boldsymbol{B} = jacobian(\theta, \boldsymbol{q}). \tag{A.6}$$

Where θ denotes a vector that represents the relative angle of the link at which the corresponding torque or force actuator acts.

A.3. Generalized Coordinate Bounds

In order to ensure feasible solutions were generated for the desired robotic maneuvers, bounds were placed on the generalized coordinate positions ($\boldsymbol{q}$) and velocities ($\dot{\boldsymbol{q}}$) to limit the models range of motion. Alternatively, these generalized coordinate bounds shown in Table A.1 were applied to the trajectory optimisation environment without influencing the EoM to enforce the orientation of the leg.

Table A.1: Generalized coordinate bounds of the trajectory optimisation model.

Generalized Coordinate	Bound Range	Description
X	$0 \leftrightarrow 1.1$ m	X - position bounds of the body.
Z	$0 \leftrightarrow 1$ m	Z - position bounds of the body.
r	$0.2 \leftrightarrow 0.48$ m	Leg length bounds of the model.
θ_{leg}	$\frac{\pi}{4} \leftrightarrow \frac{5\pi}{6}$ rad	Leg angle bounds.
$\dot{X}$	$0 \leftrightarrow 3$ m/s	X - velocity bounds of the body.
$\dot{Z}$	$-3 \leftrightarrow 3$ m/s	Z - velocity bounds of the body.
$\dot{r}$	$-2.5 \leftrightarrow 2.5$ m/s	Leg length velocity bounds of the model.
$\dot{\theta}_{leg}$	$-41.88 \leftrightarrow 41.88$ rad/s	Angular velocity bounds of the leg.

A.4. Initial and Terminal Trajectory Conditions

The implemented initial and final conditions used to generate the acceleration, steady-state and deceleration trajectories are shown in Table A.2, A.3 and A.4,respectively. Additionally, the type of enforcement used to implement each of these conditions is indicated by either a fixed or constrained enforcement.

Table A.2: The initial and terminal conditions used to generate an acceleration phase trajectory.

Acceleration Phase Conditions		
Condition	Fixed	Constrained
$Z(1) = Z_{rest}$		X
$Z(N)_{Acc} = Z_{apex_{ss}}$		X
$\dot{Z}(1) = 0$	X	
$\dot{Z}(N)_{Acc} = 0$		X
$X(1) = 0$	X	
$\dot{X}(1) = 0$	X	
$r(1) = r_{neutral}$	X	
$r(N)_{Acc} = r(1)_{ss}$		X
$\dot{r}(N)_{Acc} = \dot{r}(1)_{ss}$		X
$\theta_{leg}(1) = \frac{\pi}{2}$	X	
$\theta_{leg}(N)_{Acc} = \theta_{leg}(1)_{ss}$		X
$\dot{\theta}_{leg}(N)_{Acc} = \dot{\theta}_{leg}(1)_{ss}$		X

Table A.3: The initial and terminal conditions used to generate a steady-state phase trajectory.

Steady-State Phase Conditions		
Condition	Fixed	Constrained
$Z(1) = Z_{apex_{ss}}$		X
$Z(N)_{ss} = Z_{apex_{ss}}$		X
$\dot{Z}(1) = 0$	X	
$\dot{Z}(N)_{ss} = 0$		X
$X(1) = 0$	X	
$\dot{X}(1) = 0$	X	
$r(1) = r_{neutral}$	X	
$r(N)_{ss} = r(1)_{ss}$		X
$\dot{r}(N)_{ss} = \dot{r}(1)_{ss}$		X
$\theta_{leg}(N)_{ss} = \theta_{leg}(1)_{ss}$		X
$\dot{\theta}_{leg}(N)_{ss} = \dot{\theta}_{leg}(1)_{ss}$		X

Table A.4: The initial and terminal conditions used to generate a deceleration phase trajectory.

Deceleration Phase Conditions		
Condition	Fixed	Constrained
$Z(1) = Z_{apex_{ss}}$	X	
$Z(N)_{Dec} = Z_{rest}$		X
$\dot{Z}(1) = 0$	X	
$\dot{Z}(N)_{ss} = 0$		X
$X(1) = 0$	X	
$\dot{X}(N)_{Dec} = 0$		X
$r(1) = r(1)_{ss}$	X	
$r(N)_{Dec} = r_{neutral}$		X
$\dot{r}(1)_{Dec} = \dot{r}(1)_{ss}$	X	
$\dot{r}(N)_{Dec} = 0$		X
$\theta_{leg}(1)_{Dec} = \theta_{leg}(1)_{ss}$	X	
$\dot{\theta}_{leg}(N)_{Dec} = 0$		X

Appendix B

Manufacturing Drawings

This appendix compromises of the isometric manufacturing drawings for the fabricated monopedal prototype robot, including the component details.

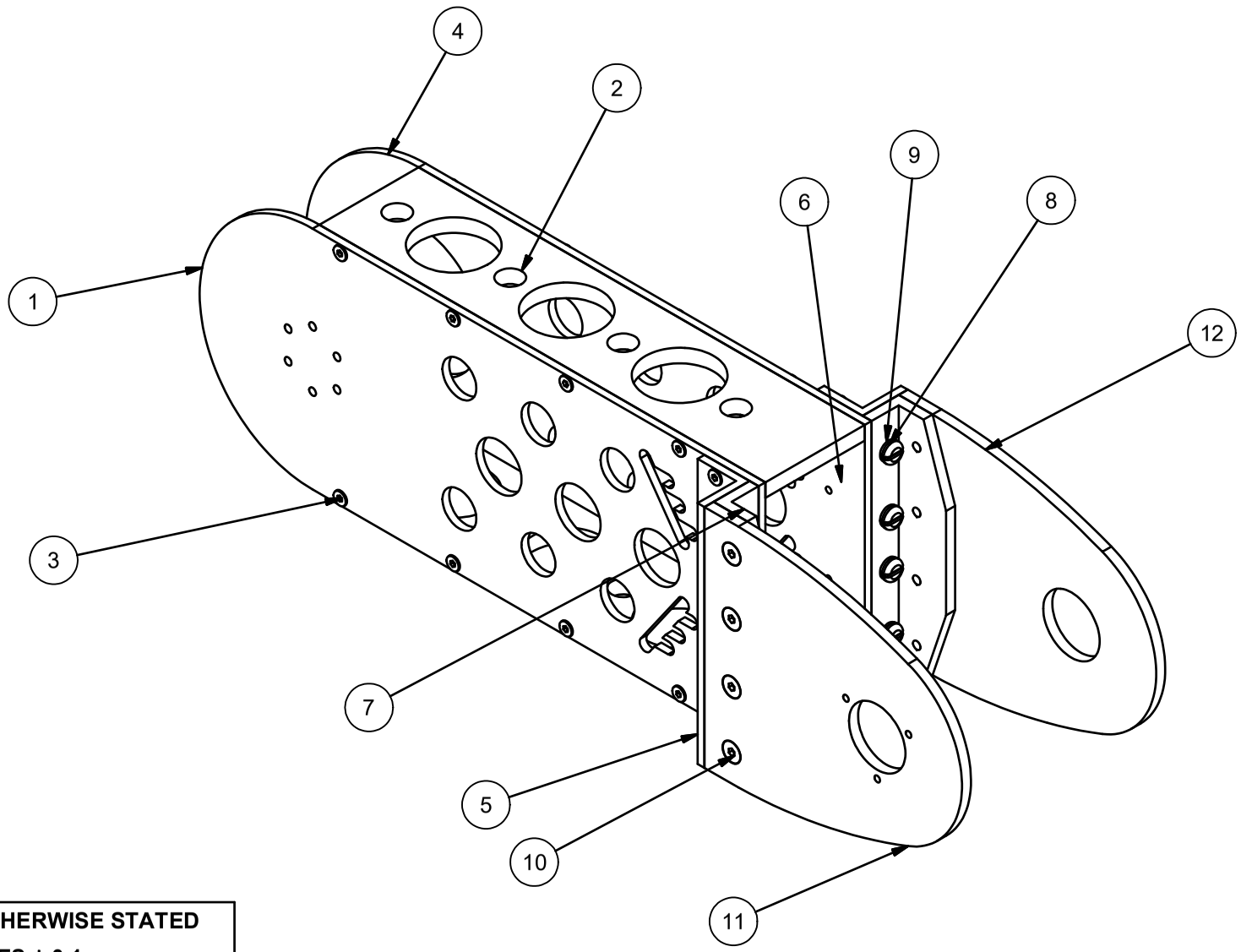

UNLESS OTHERWISE STATED
TOLERANCES ± 0,1
ANGLES 1°

ITEM	DESCRIPTION	Qty.	MATERIAL / SPECIFICATIONS

STELLENBOSCH UNIVERSITY

SCALE ON A 4 = 1:2
UNITS IN mm

TITLE: FEMUR ASSEMBLY

STUDENT Nr. 21168636	DRAWN BY NE WEISS	CHECKED	DATE 08/10/2021	SHEET Nr. 1 OF 2 SHEETS	Nr. 10/02/2021

ITEM	DESCRIPTION	Qty.	MATERIAL / SPECIFICATIONS
12	RIGHT FEMUR KNEE PLATE	1	3mm ALUMINIUM
11	LEFT FEMUR KNEE PLATE	1	3mm ALUMINIUM
10	FORGED HEXAGON SOCKET FLAT COUNTERSUNK HEAD CAP SCREWS - METRIC	8	M4 x 8 (STAINLESS STEEL)
9	HELICAL SPRING LOCK WASHERS (METRIC SERIES)	8	M4 (STAINLESS STEEL)
8	ISO METRIC MACHINE SCREWS	8	M4 x 8 (STAINLESS STEEL)
7	KNEE ANGLE BRACKET	2	4mm ALUMINIUM
6	FORGED HEXAGON SOCKET FLAT COUNTERSUNK HEAD CAP SCREWS - METRIC	4	M3 x 8 (STAINLESS STEEL)
5	ANGLE BRACKET	2	3mm ALUMINIUM
4	FEMUR RIGHT PLATE	1	3mm ALUMINIUM
3	FORGED HEXAGON SOCKET FLAT COUNTERSUNK HEAD CAP SCREWS - METRIC	20	M3 x 12 (STAINLESS STEEL)
2	FEMUR TOP PLATE	2	6mm ALUMINIUM
1	FEMUR LEFT PLATE	1	3mm ALUMINIUM

UNLESS OTHERWISE STATED
TOLERANCES ± 0,1
ANGLES 1°

STELLENBOSCH UNIVERSITY

SCALE ON A 4 = 1:2
UNITS IN mm
TITLE: FEMUR ASSEMBLY

STUDENT Nr. 21168636 | DRAWN BY NE WEISS | CHECKED | DATE 08/10/2021 | SHEET Nr. 2 OF 2 SHEETS | Nr. 10/02/2021

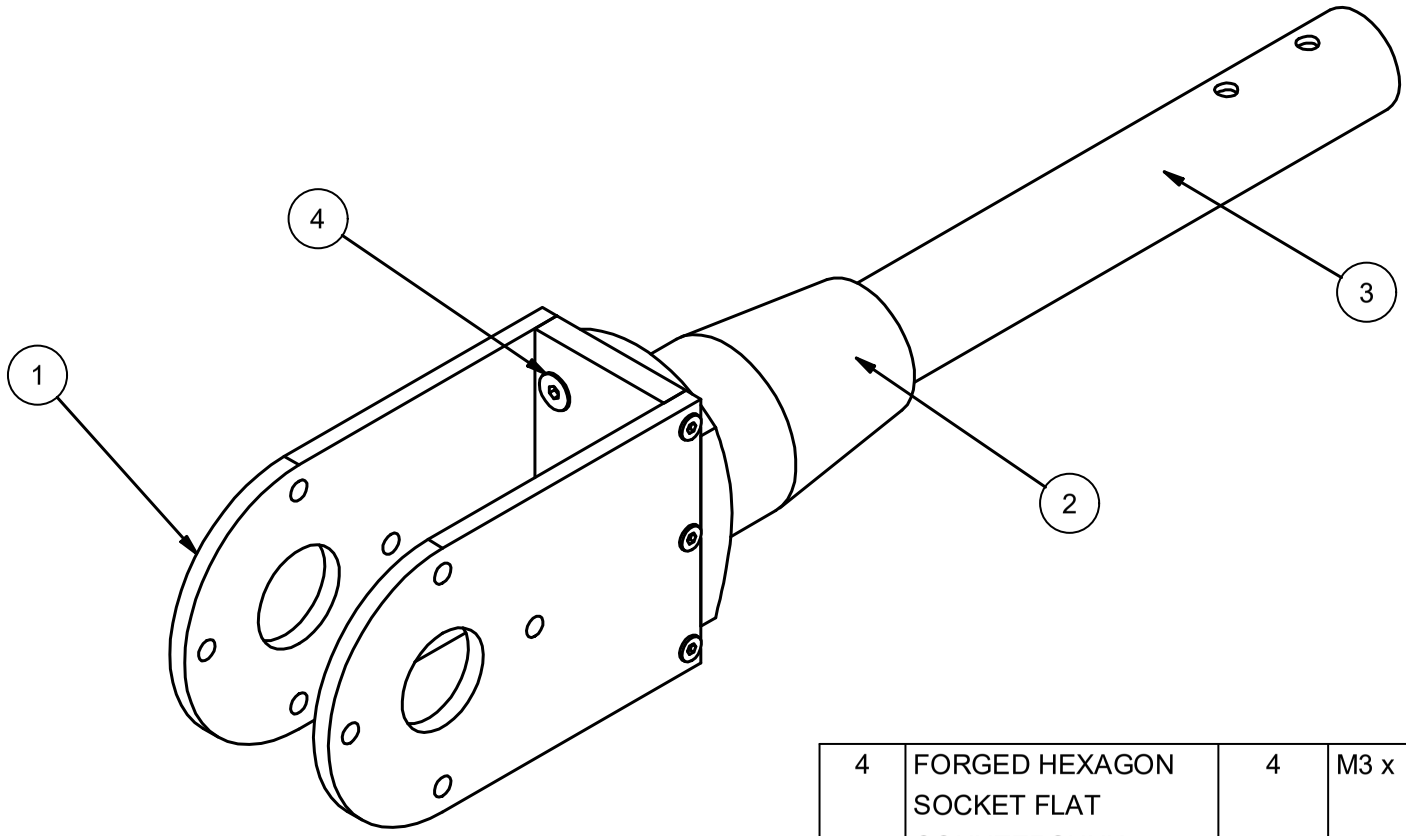

ITEM	DESCRIPTION	Qty.	MATERIAL / SPECIFICATIONS
4	FORGED HEXAGON SOCKET FLAT COUNTERSUNK HEAD CAP SCREWS - METRIC	4	M3 x 14 - STAINLESS STEEL
3	TIBIA TUBE	1	ALUMINIUM
2	TIBIA CONE	1	ALUMINIUM
1	TIBIA YOKE	1	ALUMINIUM 6063-T6

UNLESS OTHERWISE STATED
TOLERANCES ± 0,1
ANGLES 1°

STELLENBOSCH UNIVERSITY

SCALE ON A4 = 1:1.5
UNITS IN mm

TITLE: TIBIA ASSEMBLY

STUDENT Nr. 21168636	DRAWN BY NE WEISS	CHECKED	DATE 08/10/2021	SHEET Nr. 1 OF 1 SHEETS	Nr. 09/02/2021